EUROPEAN ORGANIZATION FOR NUCLEAR RESEARCH

DRAFT

Version 0 1
April 1983

ALEPH Collaboration

TECHNICAL REPORT 1983

SUMMARY

This report is prepared for the use of the CERN LEP Committee, for the participants of the ALEPH Collaboration, and for the use of others who may be interested in the design of this detector. It contains up-to-date information on the over-all design, the design of the components, the expected performances, construction schedule, and cost estimates, as well as the organization of the group. The design of some of the components is in a nearly final stage (e.g. magnet and superconducting coil) and for some components (e.g. TPC) it is still evolutive and far from final. It is therefore clear that many of the design details given here can be expected to undergo changes.

It is planned to update this report periodically.

- *¿El ALEPH? - repetí.*
- *Sí, el lugar donde están, sin confundirse, todos los lugares del orbe, vistos desde todos los ángulos.* [...]

From *El Aleph*, J.L. Borges

CONTENTS

1. GENERAL INTRODUCTION

2. SUPERCONDUCTING COIL

3. IRON YOKE AND MAGNETIC FIELD

4. THE TIME PROJECTION CHAMBER (TPC)
   - 4.1 Introduction
   - 4.2 Mechanics
   - 4.3 Electronics
   - 4.4 Laser calibration system
   - 4.5 Gating
   - 4.6 Field cage
   - 4.7 Gas system
   - 4.8 Performance
   - 4.9 TPC 90
   - 4.10 Time schedule and cost estimate

5. ELECTROMAGNETIC CALORIMETER
   - 5.1 Basic description and general layout
   - 5.2 Performance
   - 5.3 Mechanical construction
   - 5.4 Electronics
   - 5.5 Calibration
   - 5.6 Plans for prototypes
   - 5.7 Time schedule
   - 5.8 Cost estimate

6. HADRON CALORIMETER AND MUON DETECTOR
   - 6.1 Introduction
   - 6.2 The hadron calorimeter
   - 6.3 The muon detector
   - 6.4 Gas mixture and monitoring system
   - 6.5 Front-end electronics
   - 6.6 Performances of the hadron calorimeter
   - 6.7 Muon identification
   - 6.8 Construction and time schedule
   - 6.9 Cost estimate and staging

7. INNER CHAMBER

8. LUMINOSITY MONITOR

9. MINI VERTEX DETECTOR

10. BEAM PIPE AND BACKGROUNDS

11. TRIGGER

12. DATA ACQUISITION

13. OFF-LINE SOFTWARE
    13.1 Introduction
    13.2 The simulation program GALEPH
    13.3 The software development environment
    13.4 Data processing environment
    13.5 Planning of software development
    13.6 Time scale

14. INSTALLATION
    14.1 Experimental zone
    14.2 Gases and safety
    14.3 Electricity, water, and air conditioning
    14.4 Assembly schedule
    14.5 Space requirements at CERN and experimental areas
    14.6 Requested services from CERN in the experimental zone
    14.7 ALEPH budget for zone installation

15. TEST BEAM REQUIREMENTS

16. GROUP COMPOSITION, RESPONSIBILITIES, MANPOWER

17. FINANCES

1. GENERAL INTRODUCTION

The LEP e^+e^- collider is expected to produce e^+e^- collisions with luminosities of the order of 10^{32} cm^{-2} s^{-1}, at eight interaction points, initially at c.m. energies up to ~ 100 GeV, later up to ~ 200 GeV. Typical events are expected to be complex, with many particles each, distributed in jets over the entire sphere. Furthermore, especially at the highest energies, the event rate is very low. The ALEPH detector is therefore designed to accumulate for each event as much information over as much of the solid angle as seems at present practical. Of central importance in the detector are the magnetic track detector, designed to permit precise momentum determination of charged secondaries up to the highest energies, and the electron–photon calorimeter surrounding it, designed to achieve the highest possible spatial resolution and electron identification.

The over-all detector layout is shown in Figs. 1.1 to 1.3. The magnetic field is produced by a superconducting solenoid, 5.3 m in diameter and 6.4 m long, which produces an axial magnetic field of 1.5 T. Detection is accomplished in consecutive layers. Innermost is a solid-state microstrip detector to help in the location of decay vertices of short-lived particles. This is followed by a small inner chamber using drift wires, and a large Time Projection Chamber (TPC), which together are expected to provide momentum resolution $\Delta p_T/p_T \simeq 0.001\, p_T$, or 5% at 50 GeV/c momentum. The TPC offers also on the average 300 dE/dx measurements per track, important for particle identification. The next layer, still inside the coil, is the e–γ calorimeter, consisting of alternating layers of lead sheets and proportional tubes. The showers are read out in 72 000 projective towers, each tower separated into three depth zones. The solid angle of each tower is ~ 2×10^{-4} sr; the width of a tower corresponds roughly to the electromagnetic (e.m.) shower width. Outside the coil, the hadron calorimeter consists of limited streamer tubes interleaved with the iron plates forming the magnetic return path. The calorimeter readout is in 1344 projective towers. In addition, each tube provides a Yes/No signal to aid in tracking muons. The final shell is the muon detector, consisting of two double layers of streamer tubes, separated by 50 cm, which are read out with 2 mm resolution in both projections.

For financial reasons, the detector is expected to be "staged"; that is, some elements are expected to be provided only after the start-up of LEP. These elements are:

a) the microstrip inner detector,
b) the individual tube readouts of the hadron calorimeter,
c) the outer muon detection double layer.

The staged detector is expected to be ready in time for installation and check-out before the turn-on of LEP late in 1988.

The collaborating team consists of ~ 300 scientists and engineers from 25 laboratories representing eight countries. The responsibilities for the construction of the components and the associated software are divided according to the interests of the participants and the technical possibilities and financial resources of the participating laboratories.

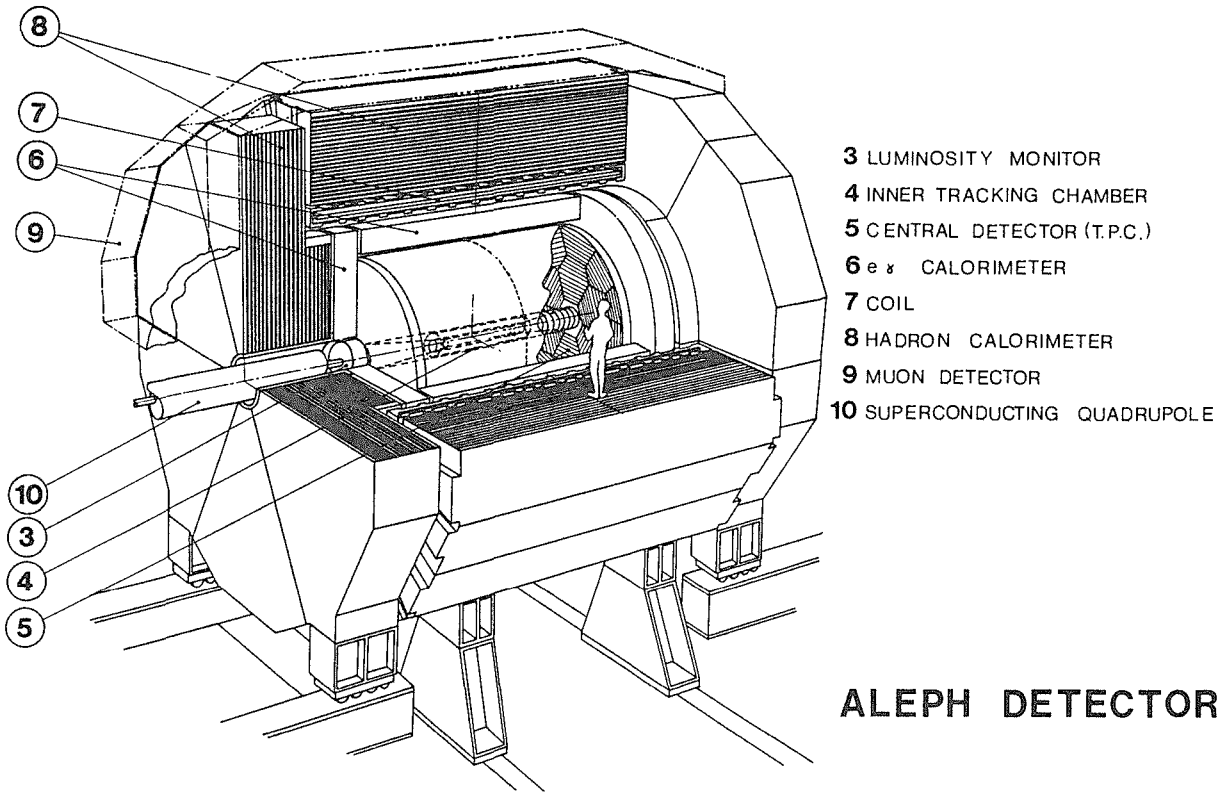

Fig. 1.1

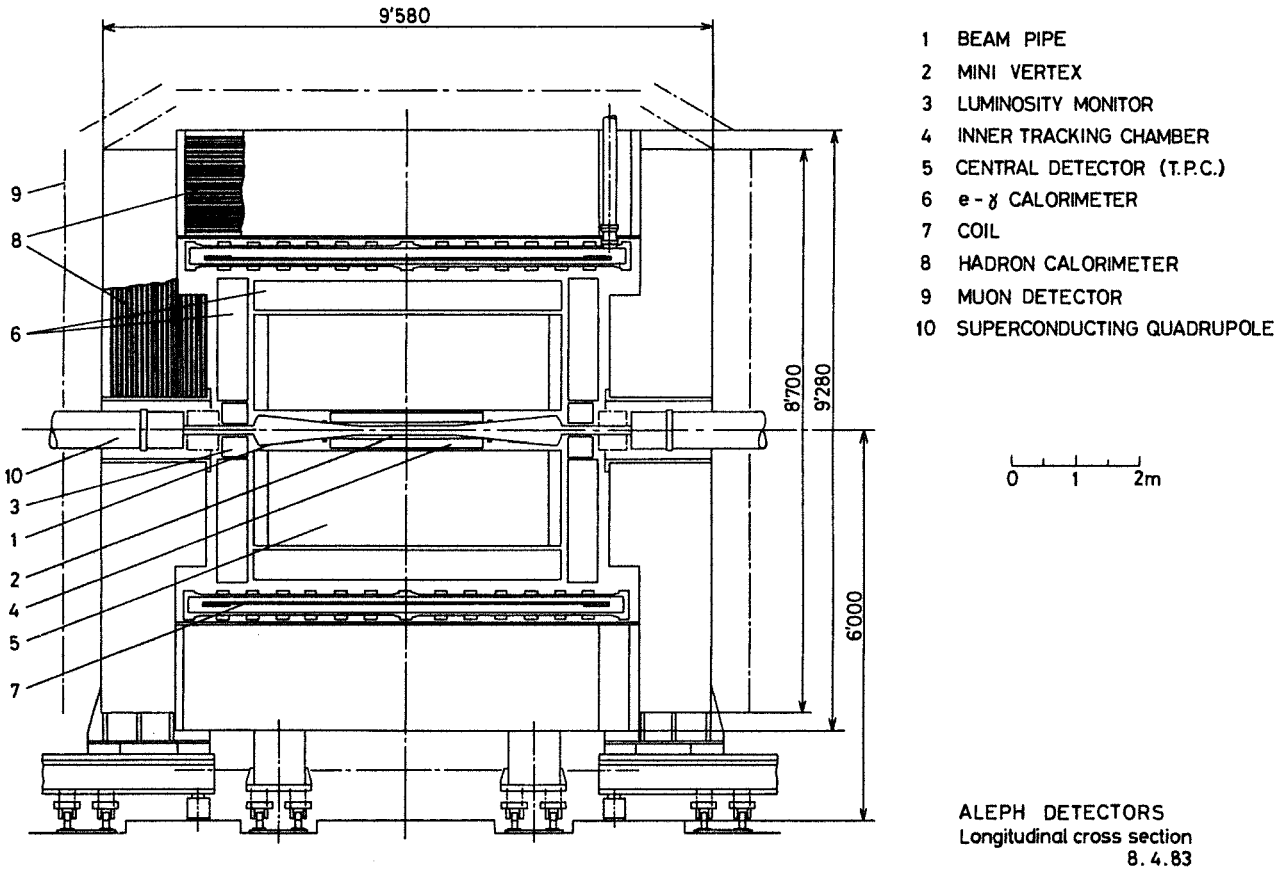
9'580
8'700
9'280
6'000
1 BEAM PIPE
2 MINI VERTEX
3 LUMINOSITY MONITOR
4 INNER TRACKING CHAMBER
5 CENTRAL DETECTOR (T.P.C.)
6 e - γ CALORIMETER
7 COIL
8 HADRON CALORIMETER
9 MUON DETECTOR
10 SUPERCONDUCTING QUADRUPOLE
0 1 2m
ALEPH DETECTORS
Longitudinal cross section
8.4.83

Fig. 1.2

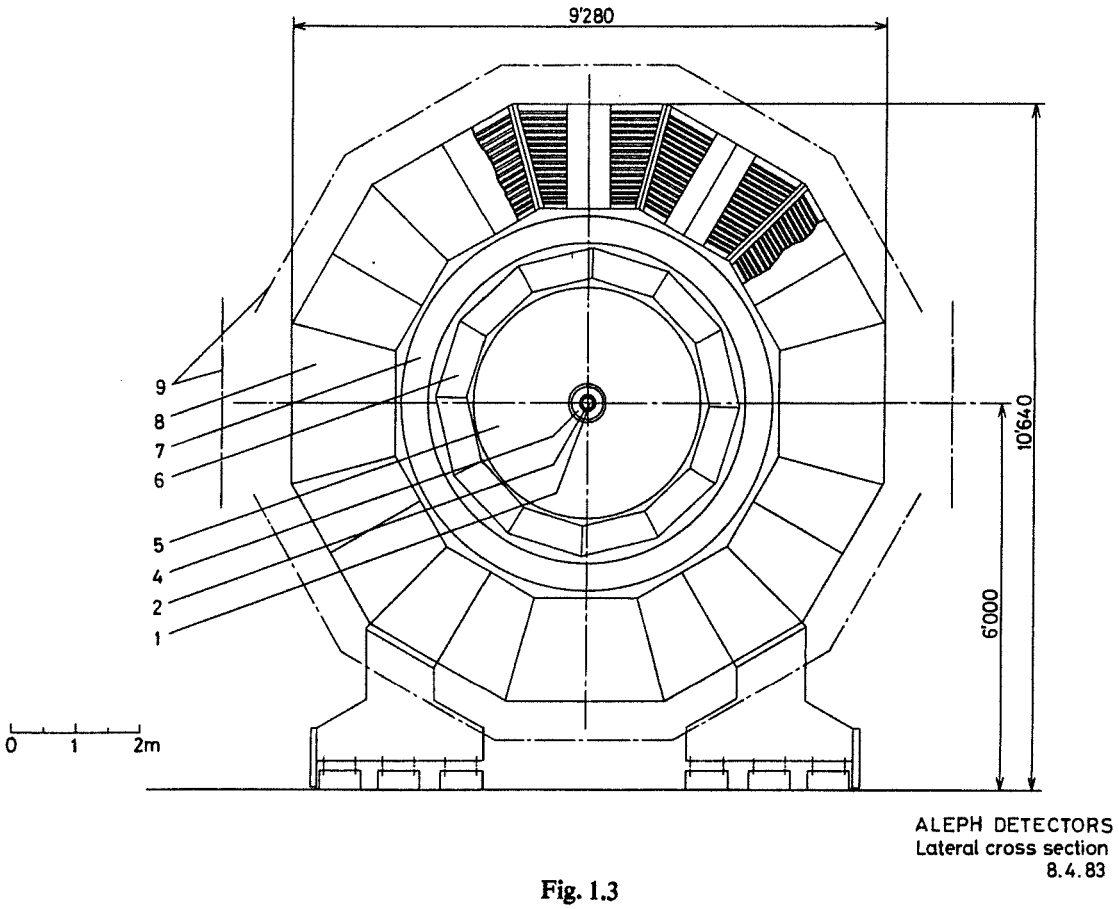
9'280
10'640
6'000
0 1 2m
ALEPH DETECTORS
Lateral cross section
8.4.83

Fig. 1.3

2. SUPERCONDUCTING COIL

2.1 Specification

The solenoid is required to supply the ampere turns with an adequate current distribution for producing, in combination with the iron-yoke laminated structure, a magnetic field of 1.5 T in the central detector and with the appropriate field uniformity.

In view of the large number of ampere turns ($\sim 8 \times 10^6$) and the size of the coil, a superconducting winding has been chosen.

The solenoid with its cryostat is located between the electromagnetic and the hadronic calorimeters. After a proper design of the major components of the solenoid, the over-all dimensions have been set at the values given in Table 2.1, which determine the boundaries for the other components of the detector.

Table 2.1

Inner cryostat radius	2480 mm
Outer cryostat radius	2920 mm
Over-all cryostat length	7000 mm
Main coil winding radius	2647 mm
Main coil length	6360 mm
Compensating coil winding radius	2757 mm
Compensating coil length	400 mm
Central field	1.5 T
Ampere turns	5 kA × 1680
Stored energy	130 mJ
Thickness of coil and cryostat:	
Absorption length	$0.4\,\lambda_{abs}$
Radiation length	$1.6\,\lambda_{rad}$
Weight of coil and cryostat	55 t
Refrigeration power	100 W at 4.2 K
	2400 W at 60 K
	30 l/h of L He

Another constraint for the mechanical design of the solenoid is the requirement of supporting the central detector and the e–γ calorimeter on the inner vacuum tank of the cryostat (weight $\sim$ 130 t).

The condition for field homogeneity can be expressed as a tolerance on the integral of the radial field component along parallels to the beam axis in either half of the TPC, which is 2.2 m long and 3.6 m in diameter. This condition is given by

$$\int_0^{2200} B_r/B_z \, dz < 2 \text{ mm}.$$

In order to fulfil this requirement, it has been found necessary to equip the solenoid with correction windings at both ends of the main coil. These corrections are also superconducting and will be incorporated in the same mechanical structure as the main winding. They will be fed electrically in series with the main winding but with provision for a trim current which will allow for optimum adjustment of the correction, both with respect to the actual characteristics of the iron yoke and to the iron saturation effect versus field.

Extensive field calculations have been carried out at CERN, Edinburgh, and Saclay. Details of these calculations and significant results are presented in subsection 3.2.

The solenoid will be cooled in closed-loop refrigeration by means of a refrigerator provided by CERN and installed on one of the platforms of the experiment so that both the solenoid and the refrigerator remain permanently and rigidly connected to each other. A very high reliability of the refrigerator is required, as any failure or interruption of the latter will cause the shutdown of the solenoid.

It is planned to have the solenoid built at Saclay. Before shipping the coil to CERN, a complete cryogenic test will be carried out using existing facilities, as well as a partial field test up to the stress level acceptable without the iron yoke.

2.2 General design

The main concepts used in the coil design are similar to those of the CELLO coil.

The coil configuration (see Figs. 2.1 and 2.2) consists of one main solenoid of 6.4 m continuous length, and of two compensating coils of 40 cm length at both ends. The three windings are closely fitted and potted into a common

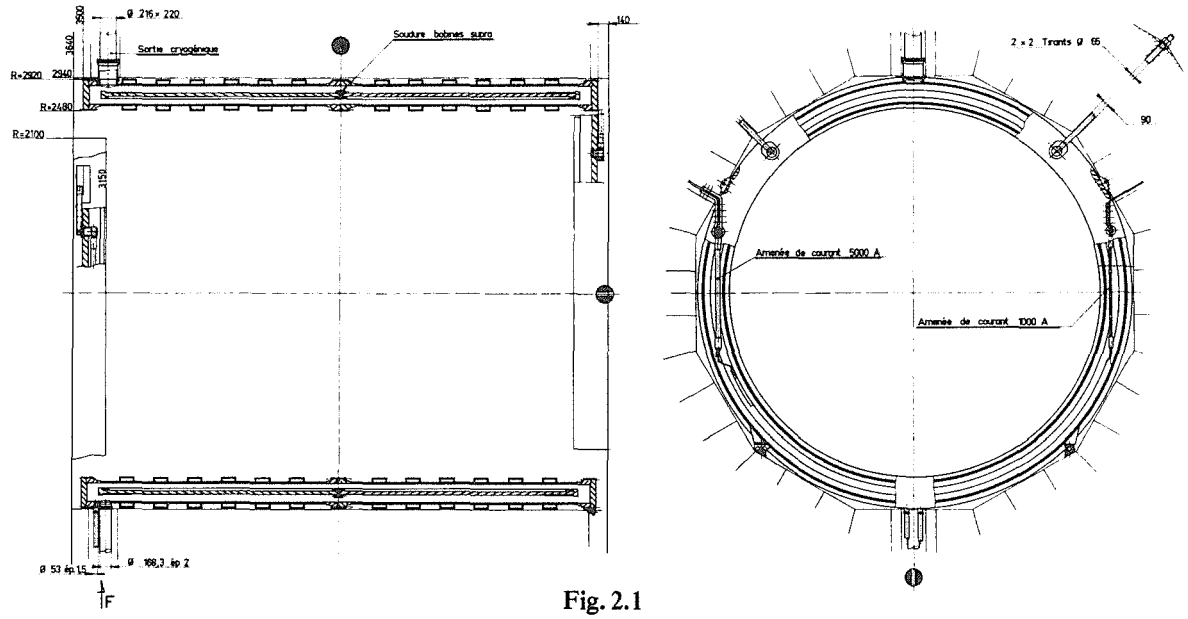

Fig. 2.1

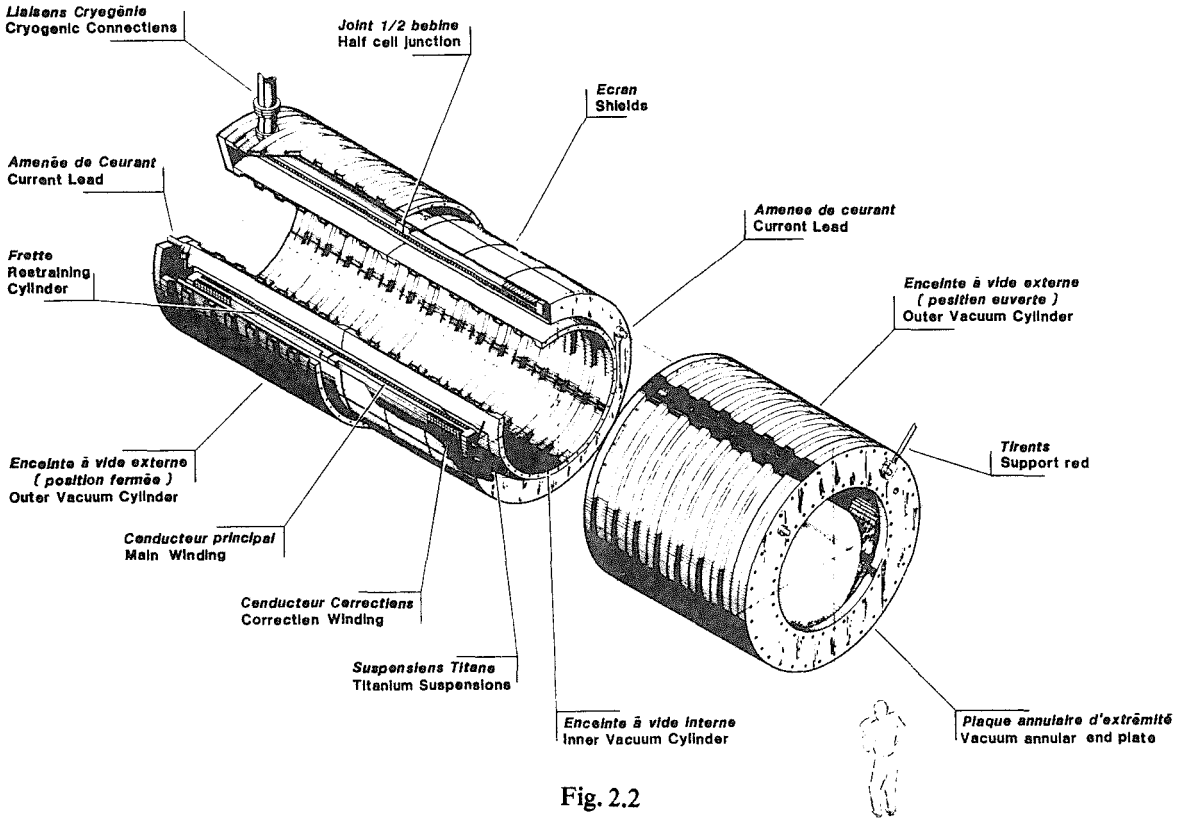

Fig. 2.2

structural member, made of a solid metallic cylinder which has a threefold purpose: i) to serve as a mandrel for laying the conductor (inside winding for the main solenoid, outside winding for the compensating coils); ii) to act as a banding structure for containment of the hoop magnetic forces; and iii) to provide a heat sink for keeping the windings at a uniform temperature, the cylinder itself being cooled by forced-flow circulation of liquid helium in a pipe welded to its surface.

The above assembly is mounted in an annular vacuum tank and is thermally insulated by means of radiation shields cooled by helium gas and superinsulated.

The vacuum tank is reinforced so as to carry the weight of the central detector and of the e–γ barrel calorimeter.

In order to limit the weight of the solenoid and make it compatible with the handling and lifting equipment provided in the experimental area, and to minimize the nuclear absorption thickness interfering with the detectors, the over-all construction is based on the systematic use of aluminium or aluminium alloys. It will also be shown that this choice leads to substantial advantages in the design of the winding itself.

To make possible the transport of the solenoid from the construction site to CERN, it has been found necessary to divide the whole solenoid lengthwise into two halves, which can be handled separately and easily re-assembled at the experiment site. This solution also brings appreciable simplifications in the fabrication and handling of the large vessels and of the winding fixtures.

The refrigeration system requires three cryogenic circuits supplied from the refrigerator:

i) a solenoid cooling-loop fed by helium gas during cool-down from 300 K to 4.2 K, then by two-phase helium at 4.2 K during normal operation (100 W);
ii) shield cooling-loop fed by helium gas at 70 K (2400 W);
iii) current leads evaporators fed by liquid helium at 4.2 K (30 l/h).

The feeding lines for these circuits are brought out through a common vertical chimney at one end of the solenoid. The chimney is terminated by a valve box which contains all cryogenic safety and control equipment and which is connected to the refrigerator through a common transfer line.

Four power leads are necessary for energizing the set of coils. These are disposed in pairs at each end of the cryostat so as to avoid inner return leads which would create unwanted field components.

The complete equipment necessary for operating the coil is designed and supplied in accordance with the requirements of long-term reliability, automatic control, and full safety. Such equipment includes the power supplies, coil protection and energy dump devices, vacuum system, cryogenic sensors and instrumentation, a microcomputer for data acquisition and control functions.

2.3 Main components

2.3.1 Conductor

One of the most crucial components of the solenoid is the conductor, as this plays the major part in providing the required field performances and in ensuring operation reliability and safety. The conductor design is closely related to the adopted cooling mode, which in the present case has been chosen as indirect cooling from cooling pipes thermally coupled to the support cylinder of the winding. This cooling mode relies on the thermal conductivity of the materials used in the coil package. On the other hand, the stability of the superconductor, or its reliable behaviour against the small disturbances likely to occur in a solenoid of this type, is governed by the two related properties of high thermal conductivity and low resistivity of the substrate in which it is embedded.

In all these respects, high-purity aluminium appears to be particularly attractive, and it has been chosen rather than copper. Alu-stabilization was already used for the CELLO coil.

Other considerations have to be made regarding the choice of an alu-stabilized conductor:

- light weight and high radiation length, as already pointed out;
- soft mechanical properties, making it easy to blend and to prestress during winding;
- quench protection criteria, which can be accommodated by using the adequate amount of aluminium in the conductor cross-section, as explained later;
- The use of an aluminium conductor enables the hoop restraining cylinder, or external mandrel, to be made also of an alu-based alloy, with the advantage of matched thermal contraction coefficients between this cylinder and the winding, and good thermal conductivity for heat transfer to the cooling pipe, compared to stainless steel. Consequently, the cooling loop does not need to be closely spaced and only needs short runs, resulting in low-pressure drop for forced helium circulation.

The fabrication of the alu-stabilized conductor can be carried out along the lines of two techniques that have already been developed on a significant scale: soft soldering of a cable or of a monolith — made of a conventional copper/NbTi composite — onto an aluminium channel (solution used for the CELLO conductor) or alu-cladding of the same insert by an extrusion process. This last technique has been successfully demonstrated by two Japanese manufacturers and is used for two similar solenoids at present under construction: the CDF coil for Fermilab and the TOPAZ magnet for KEK.

Both techniques are under active investigation by several European manufacturers within an R&D program initiated for ALEPH, and will provide the basis for a final choice before the end of 1983.

The cost of an alu-based conductor may be slightly higher than a copper-based one (10 to 20%), but the difference, compared to the over-all cost of the project, is minor, and in view of the foreseen advantages it is considered as most worth while.

The physical geometry, as shown in Fig. 2.3 (central circle), and the electrical characteristics of the conductor have been selected according to the following criteria:

- For practical reasons related to the winding mode inside the hoop restraining cylinder, the solenoid has to be wound as one single layer. This is also favourable for cooling purposes, as a minimum of thermal insulating barriers should be introduced in the coil package.
- The ampere turns along the axial length of the solenoid are set by the required field of 1.5 T as 12 000 A/cm.
- The axial thickness of the conductor is then dictated by the previous figure and by the rated current.
- The rated current is somewhat arbitrary but should be optimized as a compromise between safety and economy. Safety is related to the peak voltage produced by the fast discharge following a quench and is favoured by a high

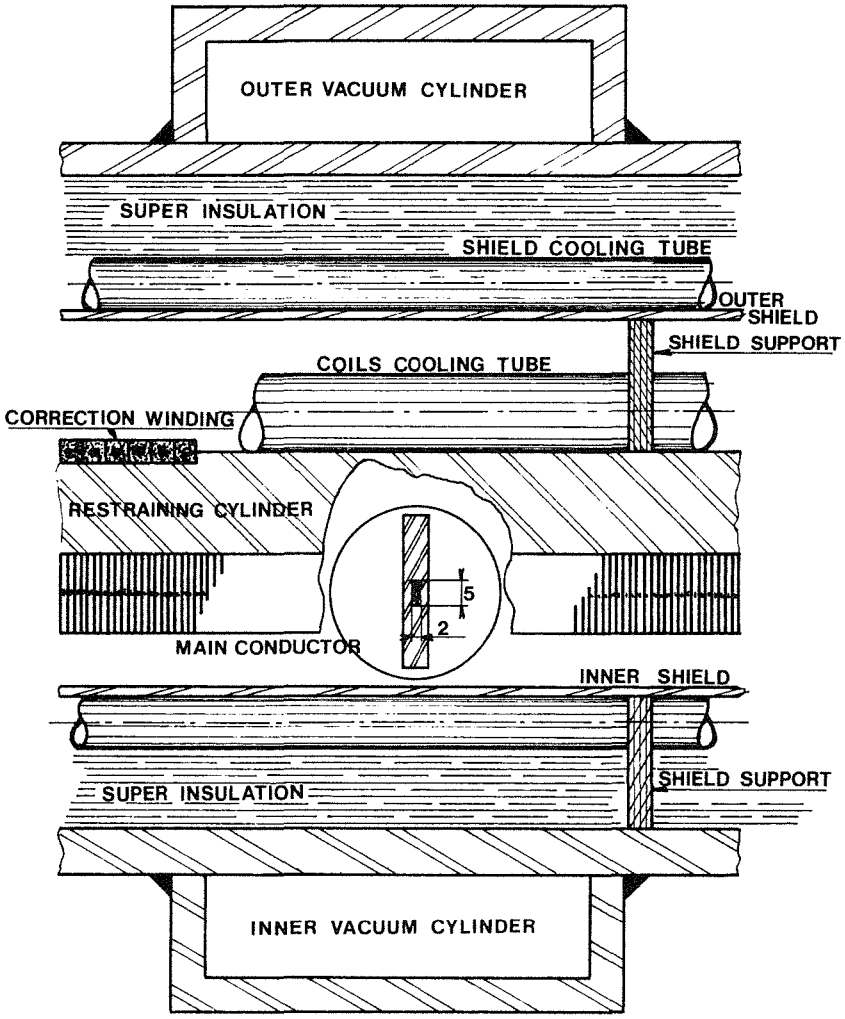

Fig. 2.3

nominal current (see subsection 2.4); whilst economy commands low current, as it affects the size of current leads power supplies, bus bars and protection circuitry, as well as the heat input through the current leads. A value of 5000 A has been determined as adequate for fulfilling both requirements.

- The axial thickness of the conductor for 5000 A is then 3.6 mm, excluding electrical insulation.
- The width of the conductor (radial dimension) is set at 35 mm in order to provide the amount of aluminium necessary for limiting the temperature of the conductor in case of quench, as explained in subsection 2.4.

2.3.2 Winding process

Each half coil is wound separately as a single unit. The support cylinder is used directly as the winding mandrel and is mounted on a rotating base with its axis vertical. The main solenoid is wound on the inside surface of the mandrel. The conductor is fed through a guiding and preforming line mounted on an inner drum, which also serves as a pressing device for keeping the eveness and compactness of the turns as the winding progresses.

The same fixture enables the compensating coil to be wound on the outside of the mandrel, this time from an external pay-off winding line.

The conductor is electrically insulated by a double wrap of glass tape applied at the time of winding.

After the two coil sections have been wound, the assembly will be transferred to a potting fixture where the winding will be vacuum-impregnated with epoxy resin whilst being pressed axially and radially against the support cylinder. After curing of the epoxy, the winding package will be homogeneously bonded and will form a self-supporting and rigid cylinder.

The two half coils, fabricated according to the above method, will be rigidly assembled by means of bolted flanges, with the two end-turns coming close together in the central plane. The electrical joint between the two will be made on the outside of the support cylinder, after bringing out the conductor terminals through slots cut in the connecting flanges.

2.3.3 Cryostat

The coil assembly described above is surrounded by radiation shields and superinsulation, and is suspended in a vacuum-insulated cryostat.

The shields are made of aluminium panels, 5 mm thick, cooled by helium gas at 70 K circulated in welded pipes. The separate panels are electrically insulated between each other so as to avoid eddy current effects, and are attached either to the solenoid support cylinder (outer shield) or to the inner vacuum tank (inner shield) by means of low thermal conductivity insulating studs.

Multilayer superinsulation is laid over the whole surface of the shields in the space between shields and vacuum shells.

The vacuum tank is made of two large cylindrical shells connected at both ends through bolted flanges to a thick annular end-plate. Connecting flanges are also provided in the central plane of the solenoid, enabling the disassembly of the cryostat into two halves, as already mentioned.

The cylindrical shells are made of aluminium alloy sheets reinforced by U-shaped rings welded on the surface and distributed along the whole length (see Figs. 2.1 and 2.2). These rings provide rigidity against bending and buckling which would be induced both by atmospheric pressure (outer pressure in case of the outer shell) and by the weight to be carried by the cryostat (inner shell).

The stiff end-plates provide sufficient rigidity to the whole cryostat for carrying the total weight, which is transferred to the iron structure by suspension rods tied to these plates.

The cold weight of the coil (windings and support cylinder) is supported within the cryostat by means of an array of tie rods at each end of the solenoid, as shown in Fig. 2.4. The distribution of these rods is such that they will carry the weight of the solenoid as well as any magnetic forces resulting from an eventual de-centring of the coil with respect to the iron. They also accommodate the thermal contraction of the coil when cooled at 4 K, with no resulting stress. The rods are made of titanium alloy (TASE ELI), which provides a high mechanical stability, and a minimum heat input into the solenoid.

The current leads are located inside the vacuum tank at both ends, and are terminated at their warm extremity by insulated feedthroughs fitted in the cryostat end-plates, with external terminal blocks for their connection to the bus bars going to the power supplies (see detail in Fig. 2.1).

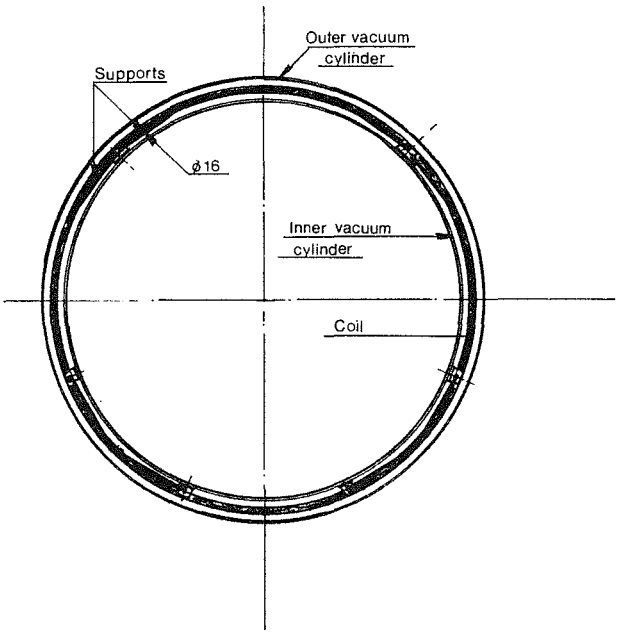

Fig. 2.4

2.3.4 Refrigeration

The refrigerating power needed at the various stages indicated in subsection 2.2 will be supplied by a single refrigerator provided by CERN. The refrigerator at present under consideration (SULZER TCF 200) has the required capacity, with sufficient safety margin for supplying the three circuits incorporated in the solenoid for normal operation.

Cooling down of the solenoid will take about 15 to 20 days, the cooling rate being limited by the actual power characteristics of the refrigerator, between 300 K and 4.2 K (weight to be cooled ~ 25 t).

The general layout of the refrigeration circuits is shown schematically in the flow chart of Fig. 2.5, where the interface is indicated between the components integrated in the refrigerator and the equipment supplied with the solenoid for its specific needs. The main items of the latter can be briefly indicated as follows:

- Heat exchanger (HX) for recondensing the gas evaporated by heat losses along the transfer line.
- Pressure control and temperature control of the flow circulating in the main cooling-loop of the solenoid.
- Mass flow-control of each current lead.

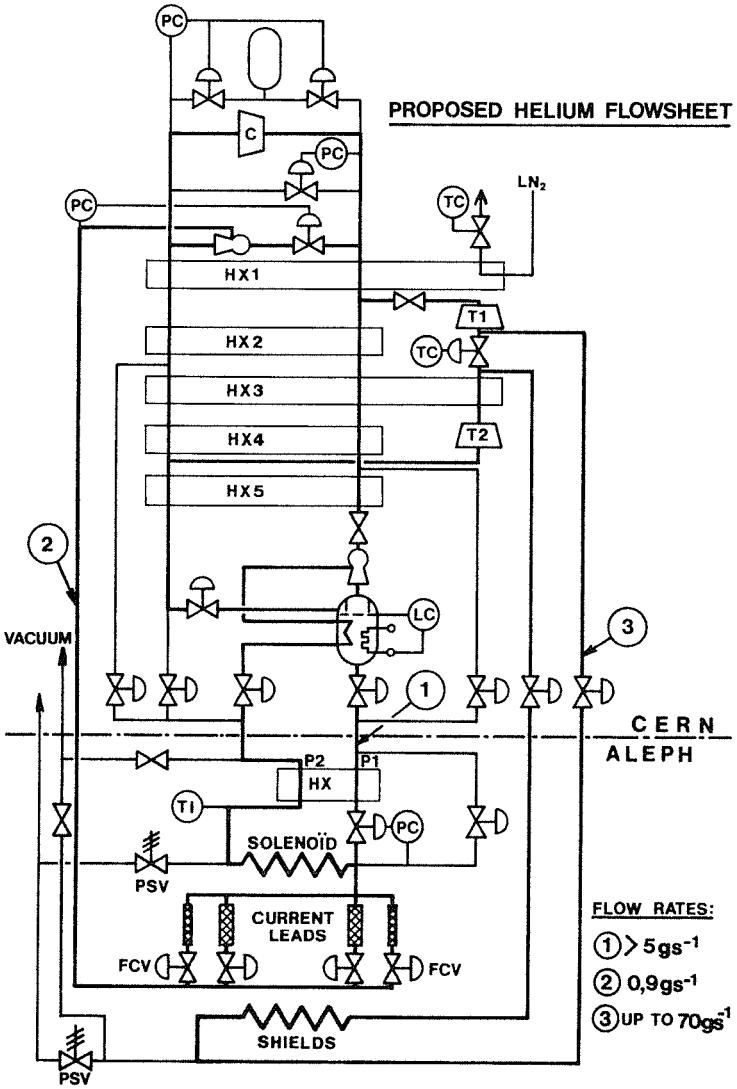

Fig. 2.5

- Cold valves for isolating and purging individual circuits.
- Relief valves on each circuit for safety purposes.

Close co-ordination will be established for the joint operation of these circuits together with the refrigerator, and for the centralized control of the whole system.

2.3.5 Vacuum system

All the vacuum-insulated parts of the coil, up to the connection with the transfer line, have a common vacuum.

A classical pumping system will be installed close to the coil and, after the cryostat has been thoroughly evacuated at the beginning of its first operation, will only be used intermittently if necessary, the normal operation being carried out under permanently sealed vacuum.

Protection of the vacuum vessels for overpressure is done by rupture disks.

2.3.6 Power supplies and coil protection

The electric power circuit of the coil is shown schematically in Fig. 2.6.

Three power supplies are necessary for energizing the set of coils: the main one feeds the three windings in series at the rated current of 5000 A; the two smaller ones rated at 1000 A are connected in parallel with the two compensating coils for adjusting their current with respect to the main solenoid.

The d.c. voltage of the main power supply is set by the charging rate desired for the coil: 30 V will give a charging time of 30 minutes, which seems reasonable. With these parameters, an installed power of 300 kVA is needed for the power supply.

Protection of the coil in case of quench or of any emergency is carried out by dumping the magnetic energy stored in the magnet in an external dump resistor. This is achieved by switching off the power supplies by means of heavy circuit breakers, thus forcing the current to flow in the dump resistors, where it decays rapidly. It is worth noting that if the stored energy of 130 MJ must be discharged in one minute, the instant power in the dump resistor will reach 4 MW.

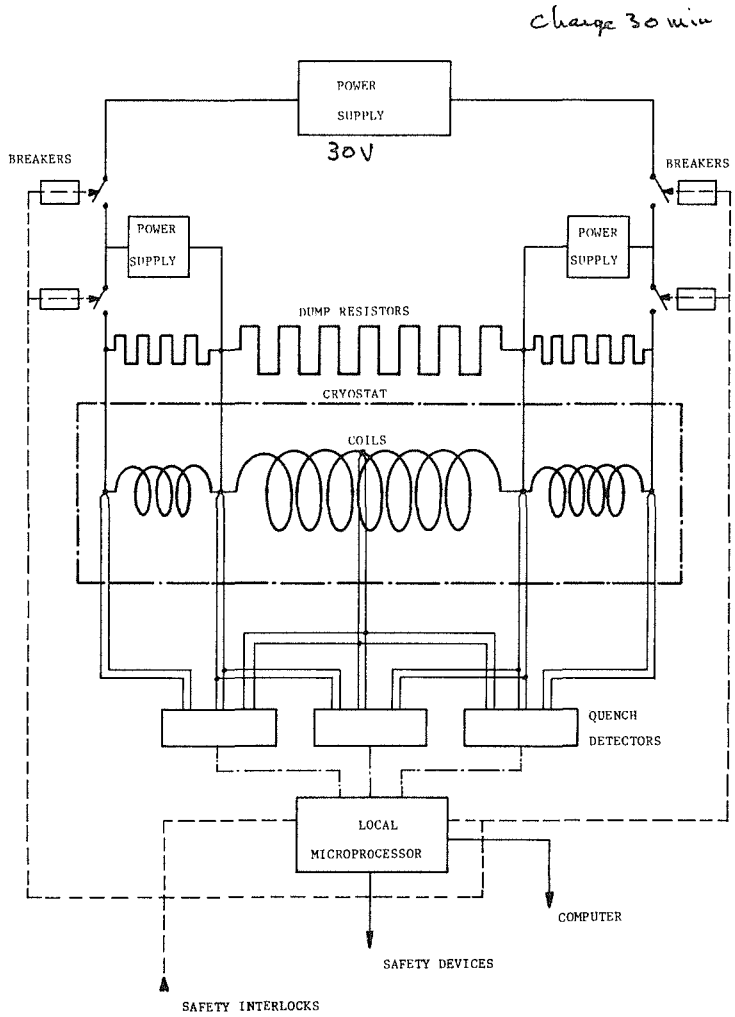

Fig. 2.6

The circuit breakers are triggered by a set of electronic quench detectors arranged in such a way that the appearance of a resistive transition in any part of the coils will be immediately sensed and will automatically trip the protection system.

In view of the importance of such protection, redundancy of the essential components of the system will be systematically provided.

2.3.7 Process instrumentation

In addition to the main circuitry described in the last paragraphs for cryogenic and electrical operation of the magnet, a large number of physical parameters have to be monitored and logged either for routine survey or for control and safety feedback actions.

Typical measurements regularly recorded are:

- temperatures of all active parts of the coil which must operate below a given temperature (winding, support cylinder, shields, current leads, etc.);
- temperature and pressure of the cooling fluids at key points of the circuit;
- flow rate in the different circuits, especially in the current leads;
- strain gauge measurements of structural members such as the cold support struts used for the coil suspension in the cryostat;
- voltage taps along the windings and the feeding lines in order to check permanently the conductor superconducting or resistive state, the joint resistances, ground insulation, etc.

All the signals and information from the various sensors will be processed by a local stored-program microcomputer which will be able to check the parameters against their preset value, to store wanted information, and to generate alarm signals, control actions, and interlocks between associated systems. This microcomputer will provide all necessary interfaces with other computers or the central control room. It will be power assisted with sufficient autonomy in case of network failure. Even so, crucial safety devices such as the quench protection system will have their own directly acting logic, independent of the microcomputer, for absolute safety.

A schematic block diagram of all the instrumentation is shown in Fig. 2.7. All these components should be grouped in the same area, as close as possible to the coil and to the refrigerator, with the local control racks, where all services described in subsection 2.5 should be available.

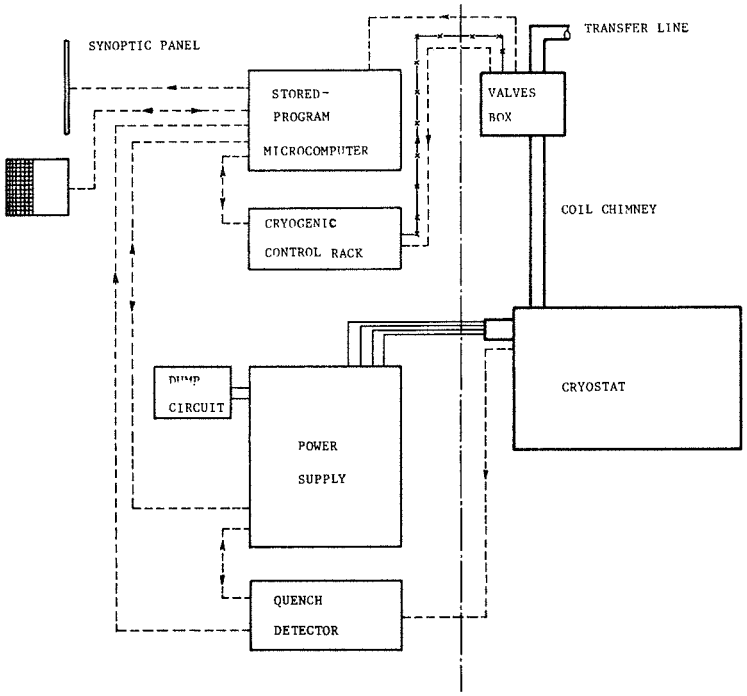

Fig. 2.7

2.4 Safety aspects

Two important domains must be carefully examined with regard to safety: mechanical design and electrical operation.

A complete stress analysis has been carried out on the proposed design. Two parts are considered independently: i) the winding structure, which is submitted to the weight and to electromagnetic forces; ii) the vacuum tank, which supports the atmospheric pressure and carries the weight of the coil and of the central detectors. According to these calculations the over-all mechanical design is satisfactory.

Electrical safety is mainly concerned with the quench response of the system. Although the probability for a quench to occur is very small, this event has to be taken into account and safety measures must be absolutely reliable.

A quench is a sudden transition from superconducting state to resistive state. When a small length of the conductor becomes resistive, two phenomena occur: i) the conductor starts heating up owing to the Joule effect; ii) the heat propagates by thermal conduction, both along the conductor and transversally from turn to turn, forcing the normal transition to spread over an increasing length of conductor.

This last effect can be characterized by two so-called "velocities of propagation", one longitudinal and the other transverse, which results in an internal resistance increasing rapidly with time.

The "hot spot", or portion of the conductor which will reach the highest temperature, is located at the point where the quench was initiated and, in order to limit this maximum temperature, the current initially flowing in the conductor must be dumped in a relatively short time. This is achieved by discharging the coil in a resistance, which consists both of the internal resistance already mentioned and of an additional external resistor inserted in the coil electrical circuit as explained in subsection 2.3 (Fig. 2.6).

The current will decay with a time constant

$$\tau = L/(R_i + R_e), \tag{1}$$

where L is the inductance of the coil (10 H),

R_e is the external dump resistance,

R_i is the average value of the internal resistance over the discharge time.

The maximum temperature T_{max} in the conductor is given, in the pessimistic adiabatic approximation, by the relation

$$F(T_{max}) = \int_{T_i}^{T_{max}} C(T)/\rho(T)\, dT = I_0^2/A^2\, \tau/2 \tag{2}$$

where C and ρ are the specific heat and normal resistivity of the conductor, both dependent on the temperature; I_0 is the initial current; A is the cross-section of the conductor, and τ is the time constant given by Eq. (1).

The universal function $F(T_{max})$ for a given material (aluminium in the present case) can be calculated from the known characteristics of the conductor. It is obvious from this expression that high-purity aluminium plays an important part, as its resistivity is very low at low temperature.

Typical values of $F(T_{max})$ and of the resulting τ are given in Table 2.2.

Table 2.2

T_{max} (K)	$F(T_{max})$ ($J/cm^3\,\Omega\,cm$) ($\times 10^8$)	τ (s)
100	4.2	53
150	5.2	66
200	5.9	75
250	6.5	83
300	7	90

From this table it results that a safe value for τ would be of the order of 60 s.

If we take the worst assumption that no internal resistance contributes to the current decay ($R_i = 0$), τ is given by

$$\tau = L/R_e = 2W/UI_0 \,, \tag{3}$$

where W is the stored energy in the coil, U is the voltage at the coil terminal at the beginning of dump, and I_0 is the initial current.

This expression gives an estimate of the maximum voltage generated during a quench. For τ = 60 s, we get U_{max} = 860 V, which is an acceptable value for a fully insulated coil operating in vacuum.

In reality, the internal resistance should not be neglected and helps to speed up the current discharge. A first analysis of the quench propagation in the coil gives expected values of the longitudinal velocity of propagation of 9 m/s and of the transverse velocity of 1.6 m/s.

T_{max} will not exceed 40 K with an external resistor of 0.1 Ω, giving an output voltage of 500 V. This shows that both the temperature and the overvoltage can be kept at very safe values.

Further analysis and experimental measurements of the actual quench propagation are being carried out in the R&D program and will enable the final characteristics to be chosen for the protection device.

2.5 Summary of fluids requirements

2.5.1 Helium refrigeration

	Cool-down phase	4.2 K refrigeration	Radiation shields
Mass flow rate (g/s)	30	5	50
Temperature (K)	300 ↘ 4.2	4.2	60–70
Pressure (bars)	13	1	13
ΔP circuit (bars)	$\ll 1$	< 0.1	< 0.5

2.5.2 Electrical power (a.c. 3-phase 380 V)

Power supplies	:	350 kVA
Vacuum pump	:	10 kVA
Auxiliaries and instrumentation (with stand-by PS)	:	3 kVA

2.5.3 Water (to be specified more precisely after actual characteristics are known)

- Power supplies (demineralized water):
  Inlet temperature : 15 °C
  Inlet pressure : 15 bars
  Total flow : 300 l/min
- Vacuum pump : 10 l/min
  (industrial water)

2.5.4 Air

Pressure : 7 bars
Flow rate : 30 m^3/h

2.6 Transport

The transport will be carried out by road from Saclay to CERN. Owing to the large dimensions, the cryostat and coil assembly will be separated into two parts. Each part will be loaded on a level-adjustable lorry trailer.

The characteristics of the convoy are the following:

- Total weight : 85 t
- Length : 15.7 m
- Width : 6 m
- Height : 5.1 m

A study of transport possibilities have been done by the Society STAG at Argenteuil. This report is available: "Recherche et reconnaissance d'un itinéraire pour deux pièces, poids unitaire 40 t, diamètre 6 m, hauteur 4 m, depuis Saclay jusqu'au CERN/Genève", with the reference: DET 8304-GEN, STIPE, SACLAY-DPhPE, 91191 Gif-sur-Yvette CEDEX (France).

2.7 Assembly at CERN

The solenoid will have been fully tested prior to its transport to CERN. Therefore, after delivery at CERN, it could be directly re-assembled and installed in the detector without any other tests. However, in order to save time during the over-all assembly of the detector in the experimental zone, it is envisaged to assemble the two halves of the solenoid in a surface building at CERN. Furthermore, a complete pre-assembly of the solenoid in the iron calorimeter is possible and a full test of the complete magnet will be carried out, which will allow the field to be mapped.

2.8 Schedule of ALEPH superconducting coil

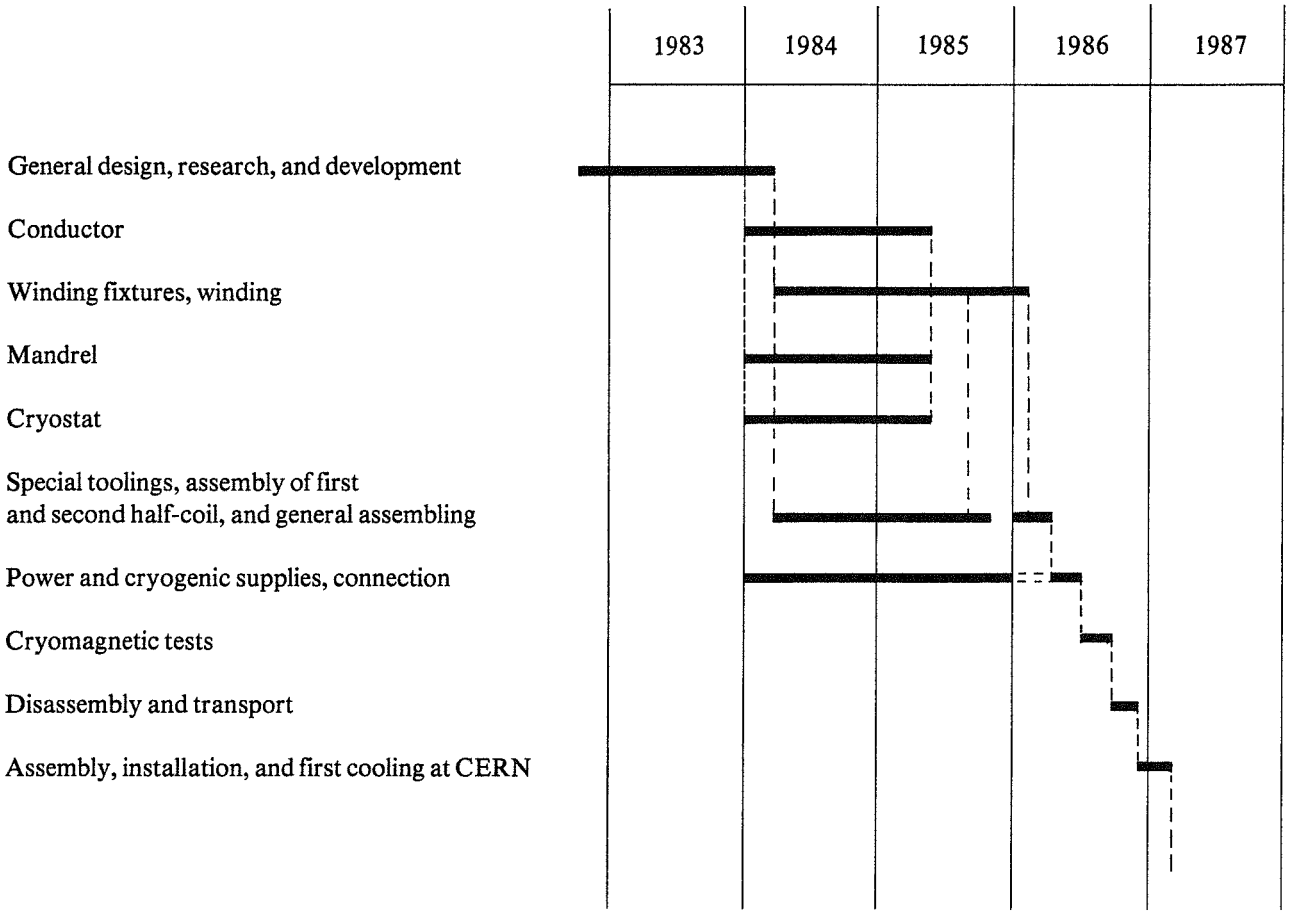

2.9 Cost estimate

The cost estimate and the estimated number of man-years are given in Table 2.3. The profile over the years 1983 to 1987 is displayed in Fig. 2.8.

Table 2.3

Detector element	Cost without manpower and without taxes (MSF)	Total manpower (man-years)
R&D	0.51	3
Conductor	1.66	1
Winding fixtures	0.69	4.5
Mandrels	0.48	1
Coil fabrication	0.15	6
Special toolings	0.52	4
Complete cryostat	1.66	5.5
Power supplies, instrumentation	0.66	3
Test Saclay	0.33	3
Assembly, installation at CERN	0.34	4
	7.00	35
Transport to CERN	0.30	
Total manpower		4 MSF
Manpower to be paid	2.4	
Grand total	9.7 +1.6 = 11.3 MSF	evaluated at 4.1.83

15.6 m

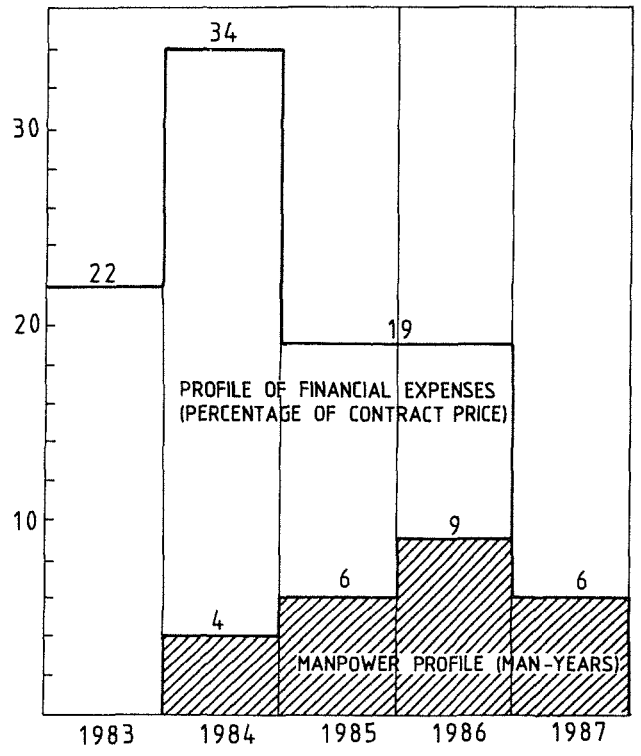

Fig. 2.8

3. IRON YOKE AND MAGNETIC FIELD

The yoke is subdivided into a central part called the barrel, and two end parts, called the end-caps. It has the purpose of shaping a longitudinal field, which must be particularly uniform in the central region occupied by the TPC. The iron yoke of the magnet has also to accomplish the function of hadron calorimeter and muon filter. For this, the iron yoke is segmented into layers of rolled steel plates interleaved with flat particle detectors. Being the heaviest and strongest part of the experiment, the iron yoke is also used as support for all the other elements of the detector. In order to permit access to the inside detectors as well as to the barrel end faces, the magnet can be opened at each end. This is achieved by rolling each end-cap parallel to the solenoid axis, along a supporting platform. The three parts of the magnet (experiment) can be moved independently one from the other, along the experiment tunnel.

The main dimensions of the magnet are shown in Fig. 3.1. The magnetic field produced is 1.5 T. It should be sufficiently uniform in the TPC volume so that the sagitta distortions remain as much as possible below 0.1–0.2 mm.

The useful magnetic volume, limited by the coil cryostat inside wall and by the end-caps pole surfaces is 123 m^3. The total magnetic stored energy is approximately 150×10^6 J. The total iron weight is $\sim$ 55 t and its average thickness corresponds to $\sim$ 0.4 absorption lengths.

3.1 Iron yoke

The mechanical design is based on the following criteria:

i) Axial symmetry. This geometry is needed in order to avoid creating azimuthal field components. It has been approximated by giving the yoke the shape of a polygonal cylinder.

ii) Modular structure. This requirement is imposed in order to facilitate the iron calorimetrization and, more generally, in order to reduce the manufacturing cost.

iii) Dead-space minimization. The iron regions that cannot be calorimetrized or where no muon detectors can be mounted should be kept as small as is practicable.

The unitary weight of the single modules is as high as permitted by handling and transport considerations. This reduces both dead-space as well as manufacturing cost.

The magnetic forces are large. For instance, the end-caps are pulled towards the barrel by a force of about 4000 t. In particular, in the end-caps, where the forces act perpendicularly to the plates, they have to be calculated on each individual plate of the stack. Figure 3.2 shows the cross-section of a barrel module, an end-cap module, and various details of the yoke structure.

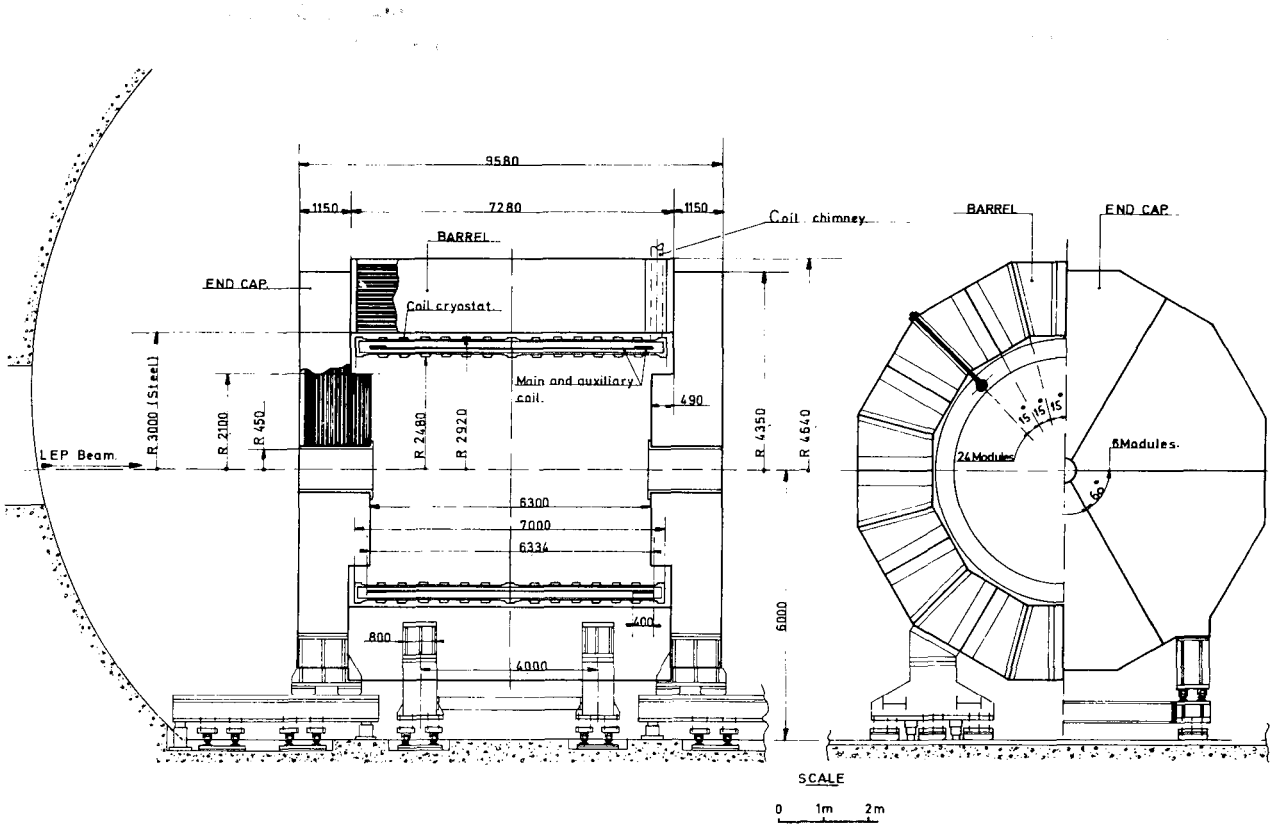

Fig. 3.1

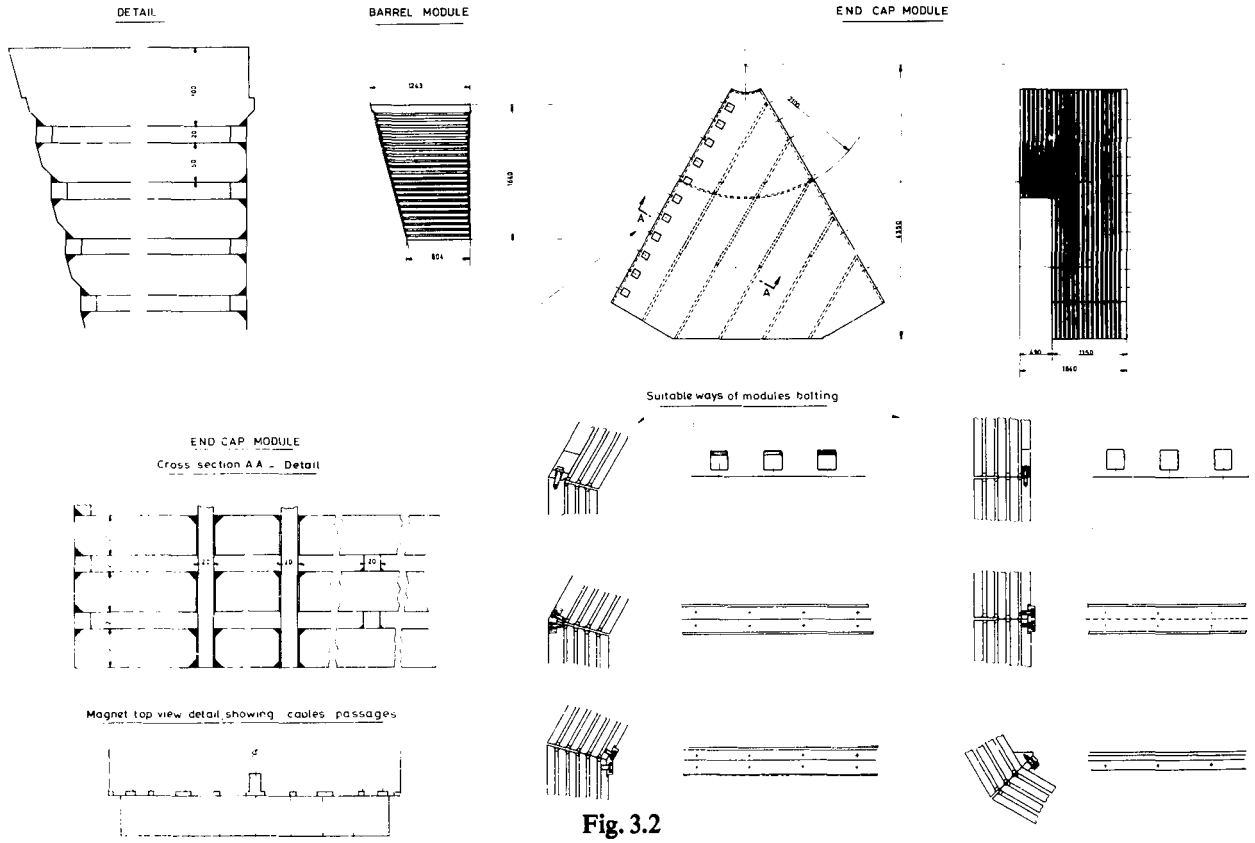

Fig. 3.2

The barrel is composed of 24 nearly equal asymmetric modules assembled to form a dodecagonal cylinder. This shape has been preferred with respect to the more natural 24-sided polygon, because it allows a less expensive construction of the muon detector. The iron plates of the barrel modules lie in planes parallel to the experiment axis. The unitary weight of a barrel module is ~ 70 t.

The end-caps are each composed of six nearly equal modules, and their iron plates lie in planes perpendicular to the experiment axis. The end-cap has the shape of a short dodecagonal cylinder, somewhat smaller in cross-section than the barrel, followed by a smaller circular polar piece. The unitary weight of an end-cap module is ~ 75 t. On their axis, the end-caps present a 90 cm diameter round hole which is adequate for the passage of the LEP low-beta s.c. quadrupole and its support.

A 5 cm thick iron cylinder ending on one side with a larger flange is foreseen in the axial hole of each end-cap in order to increase its stiffness and to compensate the deleterious effect of the hole on the magnetic field shape. These cylinders will be strongly bolted to the plates of the end-cap modules.

All the modules of the barrel and the end-caps are made from layers of 5 cm thick rolled-iron plates, with the exception of the outside plate, which is 10 cm thick for mechanical reasons. The total iron thickness of both barrel and end-caps is 1.2 m. The plates constituting the modules are kept in place by means of narrow spacers, 2 cm thick, welded all along the long sides of the barrel modules and along the radial sides of the end-cap modules. On the latter, further spacers are provided along lines parallel to one of their radial sides: these spacers, on limited regions, are replaced by 2 cm thick plates passing across corresponding slots cut out of the stack plates and welded onto them. Assembly of the modules is by means of bolts (see various details in Fig. 3.2). The contact surfaces between the modules will be limited to narrow strips in order to reduce the necessary machining and increase the stability of the assembled yoke.

Machining is required mainly on all the contact surfaces, but also on the surfaces of the polar pieces.

At each barrel end, 12 large and 12 narrow equally spaced slots are cut out to provide passage for cables, pipes, ducts, supports, etc. On one side of the barrel only, the top and bottom slot are further cut to permit the passage of the coil cryostat chimney and vacuum line. These last cuts are deep but narrow, and their effect on the field should be acceptable.

The supports of the yoke are designed to minimize the dead-space for muon detection. The barrel is supported by four legs, whose total cross-section corresponds to less than 2% of its outside surface (~ 215 m^2). The end-caps are supported by two legs each, corresponding to about 2.5% of their surface (~ 94 m^2/end-cap). Standard roller carriages (driven by electric motors) and rails are foreseen for the required movements. The design of the carriages permits a certain amount of level adjustment. Elastic elements are included in the roller supports in order to ensure adequate load repartition. The end-caps will roll on small platforms in order to permit rapid access to the inside of the magnet. The end-cap platforms will themselves roll, like the barrel, on rails laid down in the floor of the experimental tunnel, perpendicular to the LEP beam.

The movement and position (relative and absolute) of the three magnet parts will be carefully controlled. Resolution better than 0.5 mm will be ensured by position encoders. A microcomputer system will check that the translation commands can safely be executed in any configuration, and will control and synchronize the detector displacement and provide the operator with the necessary information.

3.2 Magnetic field

The magnet geometry has been optimized by means of two-dimensional field calculations made in parallel at Saclay and at CERN. The results of these two calculations are very similar and lead to the same iron geometry and almost to the same current for the main and the auxiliary coils.

Calculations with a three-dimensional program have been started in Rutherford by the Edinburgh group.

Furthermore, a magnetic 1:10 scale model equipped with conventional coils and operating at 1/10 of the nominal magnet field, i.e. at 1.5 kG, is under construction, and measurements with it should start early in May.

The two-dimensional calculations have been performed with the following simplifications of the magnet geometry:

1) Cylindrical symmetry. The polygonal return yoke cross-section is approximated by an annular cross-section.
2) The particular structure of the end-caps and barrel with plates and interleaved gaps is only partially introduced into the calculation, the remaining part being approximated by a homogeneous material with a packing factor given by the ratio of the effective iron to the total volume occupied by the iron and the air gaps. This approximation is legitimate only in the regions where the flux lines lie parallel to the iron plates.
3) The region of the barrel where all the passages for cables and pipes are located has also been represented by a homogeneous region with, again, a packing factor defined as a ratio of the effective iron to the volume of the whole region. The effect of the deeper grooves which accommodate the cryogenic and vacuum outlets of the coil cryostat has not been taken into account.

The simplifications of points (1) and (3) are, of course, imposed by the capacity of the program to deal only with a two-dimensional geometry. For the same reason, the geometrical errors that cannot be represented in the two-dimensional scheme—such as the coaxiality error between coil and iron yoke or sagging of the coil, or parallelism error of the pole pieces—have to be studied by other means. The simplification indicated under point (2) was introduced to shorten the computation time and allow an easier comparison between the results of the Saclay and CERN teams. It has been checked that this simplification does not modify the field shape significantly in the TPC volume, but leads only to a slight change in the ampere turns required to attain the same field. All the calculations are aimed at minimizing the value of $\int_0^L (B_r/B_z)\,dz$ within the TPC volume, with L being the total drift length. The accuracy of this integral can be estimated to be ± 0.1 mm.

The first calculations have immediately shown the need for an increase of the ampere turns' density at the ends of the solenoid, in order to compensate the magnetic reluctance of the end-caps due to the many air gaps crossed by the field lines there. The extra ampere turns needed can be obtained by adding short compensating coils wound around the main coil ends.

Figure 3.3a shows the value of the integral of B_r/B_z plotted as a function of the radius for different values of the compensating coil current.

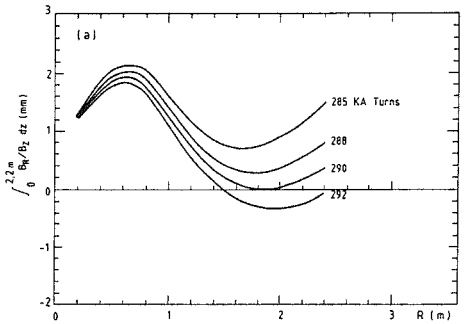

Fig. 3.3a

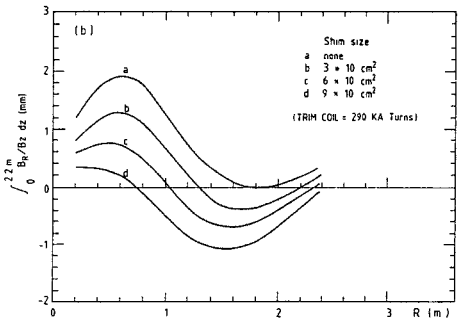

Fig. 3.3b

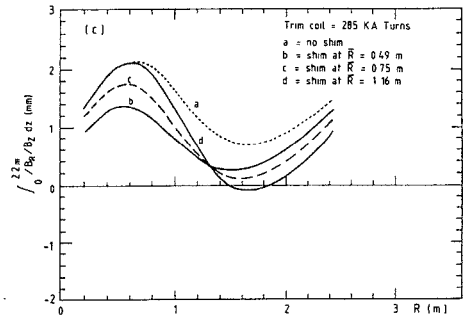

Fig. 3.3c

It also appears from the calculations that the axial end-cap hole produces a considerable deterioration of the field shape. This effect can partly be corrected by shimming. Figures 3.3b and c show the value of the integral of B_r/B_z as a function of the radius for various shim positions and shapes. The best results have been achieved, as shown in Fig. 3.4, by adding a 5 cm thick iron cylinder in the hole itself, by further adding a ring around the hole in front of the first iron slab, and by cutting a circular groove at 1 m radius. The detailed mechanical dimensions of the shims are given in the insert of Fig. 3.4. The integral of B_r/B_z then remains limited to ± 0.5 mm in the entire TPC volume.

The rather large space around the polar pieces kept free for the cryostat ends, the e–γ calorimeter electronics, and the many cables and pipes passing there, strongly deteriorates the field, but mainly outside the TPC volume. Figure 3.5 gives the isofield lines extended into a region larger than the TPC, showing the effects of the missing iron. Finally, in the optimized case, Fig. 3.6 shows the deformation due to the radial field of straight trajectories originating at the central point of the TPC at different polar angles θ with respect to the e^+e^- axis.

The two-dimensional calculations have been used to evaluate the effect of the magnetic forces on the laminated end-caps. Forces of the order of 5 kg/cm^2 have been found in large regions of the first few plates following the pole pieces. The more serious longitudinal forces acting on the compensating coils and on the main coil ends have been estimated to be about 13 t/m each.

Figure 3.7 shows a schematic cross-section of the magnet model, which, in conjunction with the Rutherford program, should permit the study of the three-dimensional field shape. The model has been designed to reproduce, as much as possible, the iron saturation conditions of the real magnet, and consequently to measure, for example, among other effects, the azimuthal distortions due to localized holes in the barrel. For this purpose the iron cross-section has been reduced in proportion to the field ratio wherever the field lines lie parallel to the iron plates. The magnetic measurement apparatus for the magnet model has been designed to provide longitudinal translation and rotation movement as accurately as possible, to measure the very small field secondary components (0.1 to a few gauss).

The experience gained with the model measurement will be used in the design of the large apparatus needed for the measurement of the real magnet.

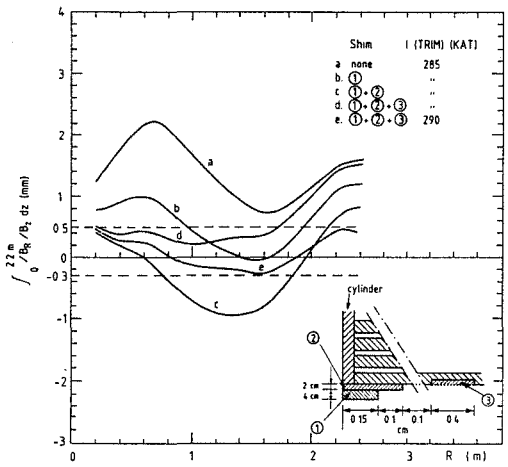

Fig. 3.4

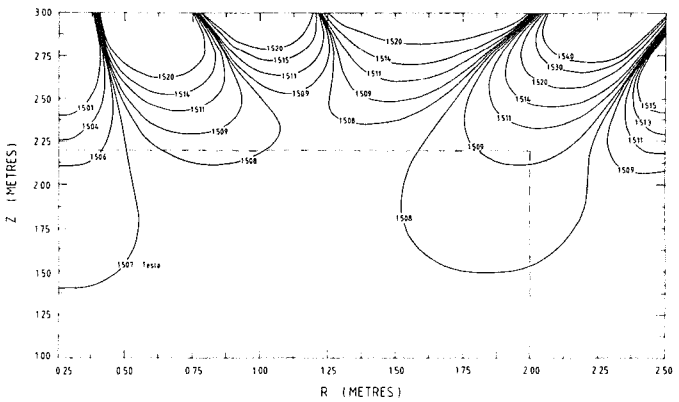

Fig. 3.5

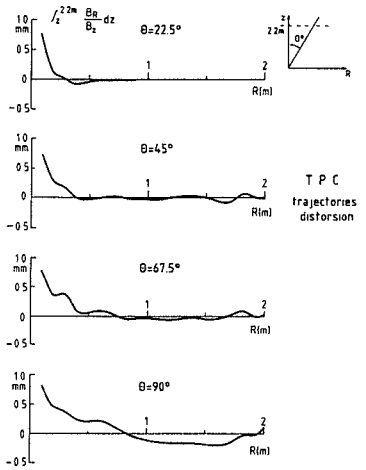

Fig. 3.6

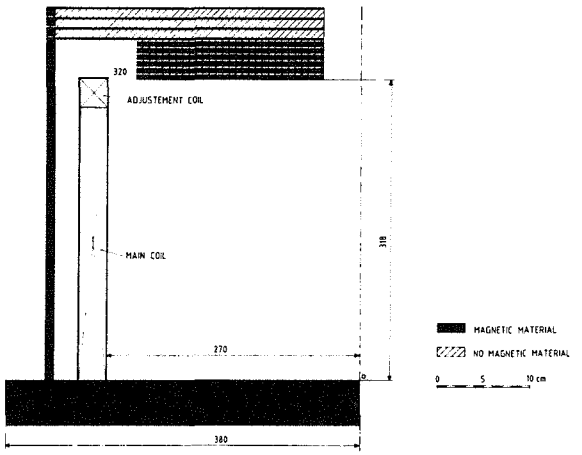

Fig. 3.7

4. THE TIME PROJECTION CHAMBER (TPC)

4.1 Introduction

We believe that the best way to obtain good momentum and angular resolution, as well as ease in pattern recognition and additional resolving power in e–π separation, is to use a Time Projection Chamber (TPC) as the central detector for ALEPH.

On the basis of the pioneering work at Berkeley and on the progress we have made by performing tests, calculations, and design work, we will build a TPC which has a cylindrical active volume of 2 × 2.2 m length with circular end-plates of 1.77 m outer radius and 0.33 m inner radius, as measured inside the cylindrical field cages. The total gas volume is 42 m^3. It uses an argon–methane (10–20)% mixture at atmospheric pressure and a drift field of about 20 kV/m. The electrons drift to the end-plates of the TPC, where they are recorded by a system of proportional wires and capacitively coupled cathode readout pads. Points along the tracks of charged particles are thus measured in three dimensions (z, r, ϕ) through the drift time (z) and the pad coordinates (r, ϕ). The pulse heights on the proportional wires are a measure of the ionization density dE/dx along the track. The design of wires and pads is such that up to 21 space points and 320 ionization samples are measured per track.

The active area of the end-plate is $\sim$ 9 m^2, and is divided into modules as will be seen in Fig. 4.2.2. Each module contains pad rows with a pitch of 6 mm. The total number of pads is 22 000 on each end-plate, whilst the number of proportional wires is 3000. The total number of electronic channels is 50 000.

With the help of the laser calibration system described in subsection 4.4, it is foreseen to correct for the sagitta distortions caused by electric and magnetic field inhomogeneities. Track distortions due to space-charge effects of the slowly drifting positive ions will be avoided by (gas-)amplifying the drifting electrons only when there is a valid "Level 1" trigger. This gating system is outlined in subsection 4.5. The so-called "hooks" in the PEP-4 detector of course attract our attention. The electrode configuration described in subsection 4.6 should avoid these distortions.

Difficulties with electron attachment, or unstable conditions for the gas amplfication or drift velocity are usually not due to faults in the gas system, but rather to poor mechanical construction or choice of materials. Therefore the gas system (see subsection 4.7) must be designed such that up to a certain level such faults can be accommodated.

A major part of our development programme is the prototype testing with TPC 90 which represents one full-size sector of the proposed TPC. This work is described in subsection 4.9.

4.2 Mechanics

A general view of the TPC with its supporting structure is shown in Fig. 4.2.1. This unit carries also the inner chamber, the beam pipe, and the two luminosity monitors. Not shown on the sketch is the cabling.

The total weight of this assembly is 8000 kg. The individual contributions are about

200 kg	beam pipe, valves, etc.
100 kg	inner chamber
2 × 1100 kg	luminosity monitors
100 kg	inner field cage
2000 kg	outer field cage
2 × 800 kg	end-plate structure and wire chamber sectors
2 × 400 kg	electronics and cables
2 × 100 kg	cooling system
2 × 400 kg	supporting feet

It will be possible to remove any one of the supporting feet temporarily and without replacement as long as the other feet are left in place. This feature will be implemented in view of the maintenance work on parts which are hidden behind the feet.

4.2.1 Wire chamber sectors

Each end-plate carries 18 wire chamber sectors as shown in Fig. 4.2.2. The inner six are hexagonal. The outer twelve have two different shapes. The figure gives the dimensions and the surfaces. The inner pad-row has a radius of 380 mm, the outer one 1740 mm.

The basic structure of each sector is a sandwich construction composed of two aluminium sheets of 2 mm thickness, about 40 mm apart. Figure 4.2.3 shows also the tubular spacers between the two aluminium sheets. On the cathode side which faces the TPC gas volume, the sandwich carries an insulating fibre-glass layer and 10 pad-rows, each 8 mm high. The present choice for the width (or pitch) of the pads is 6 mm. In front of this plane are three wire planes, equally spaced by 4 mm. The sense plane has a 20 μm diameter sense wire every 4 mm, and, in between, field-shaping wires of 75 μm diameter. The ground grid terminates the drift field with wires 75 μm in diameter, which are spaced 1 mm apart. The gating grid inside the drift region has also wires of 75 μm diameter, which are 1 mm spaced.

The main guidelines for the detailed design of these sectors (three types) are:

- cathode flatness and wire positioning better than 50 μm, to maintain the uniformity of the gas amplification within 1%;

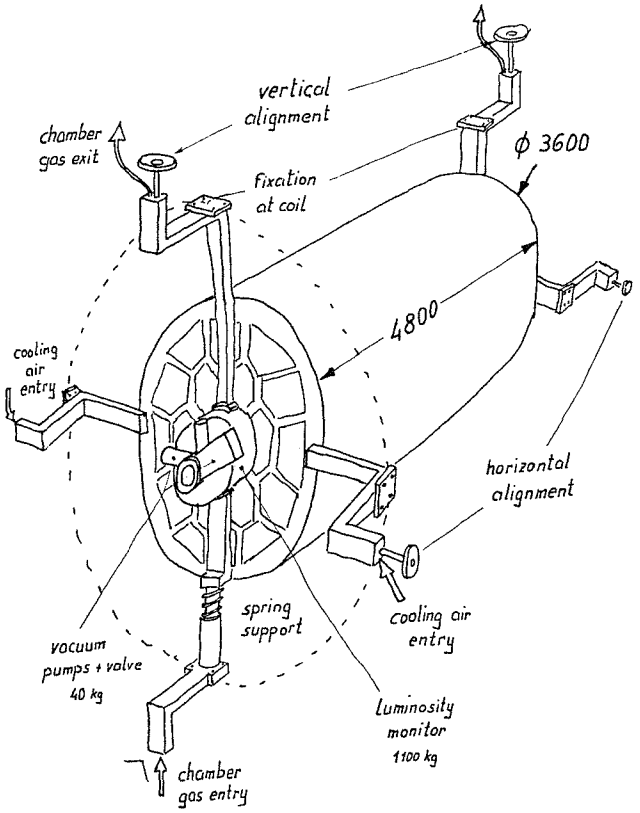

Fig. 4.2.1

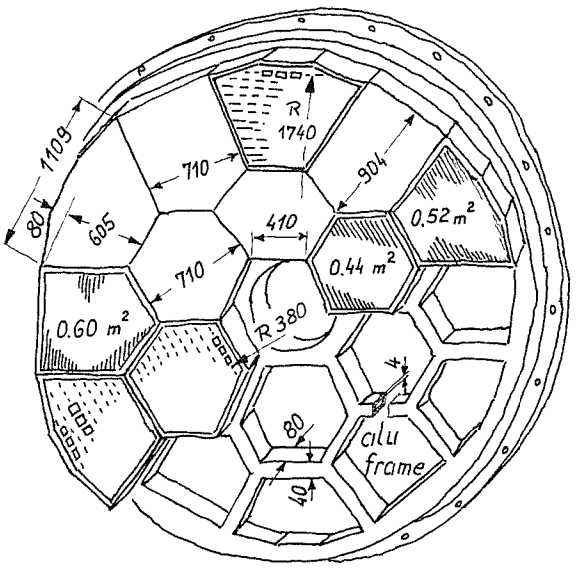

Fig. 4.2.2

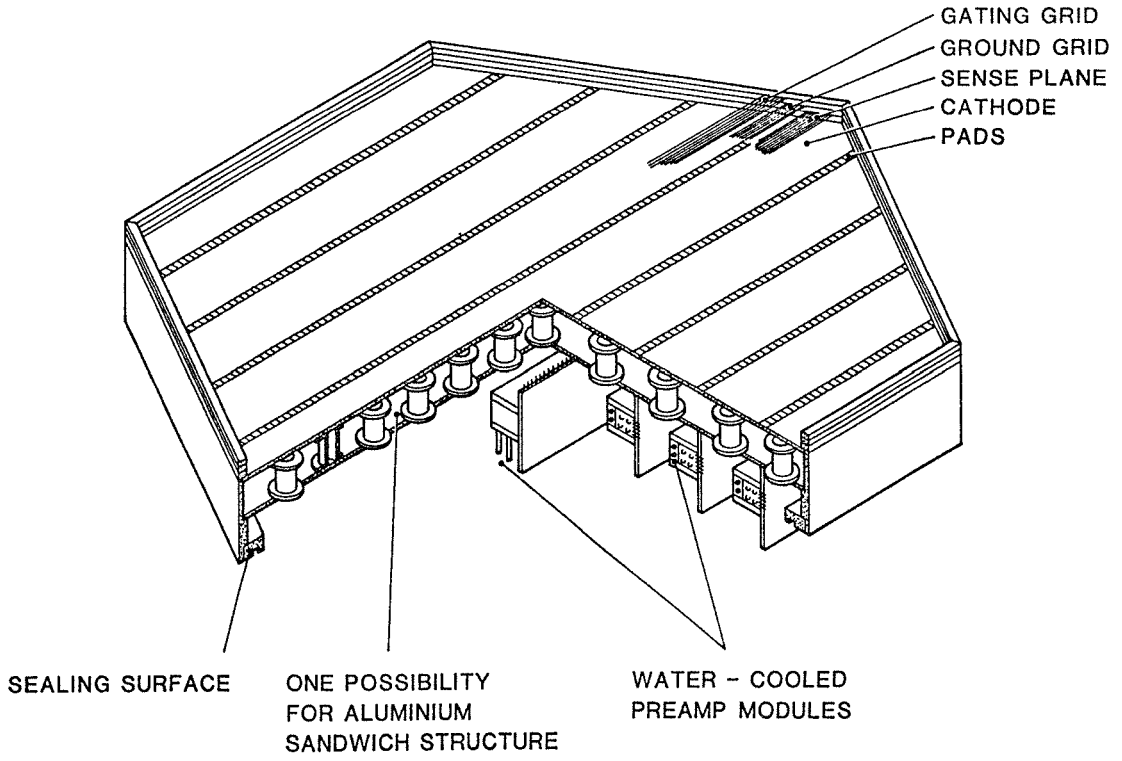

Fig. 4.2.3

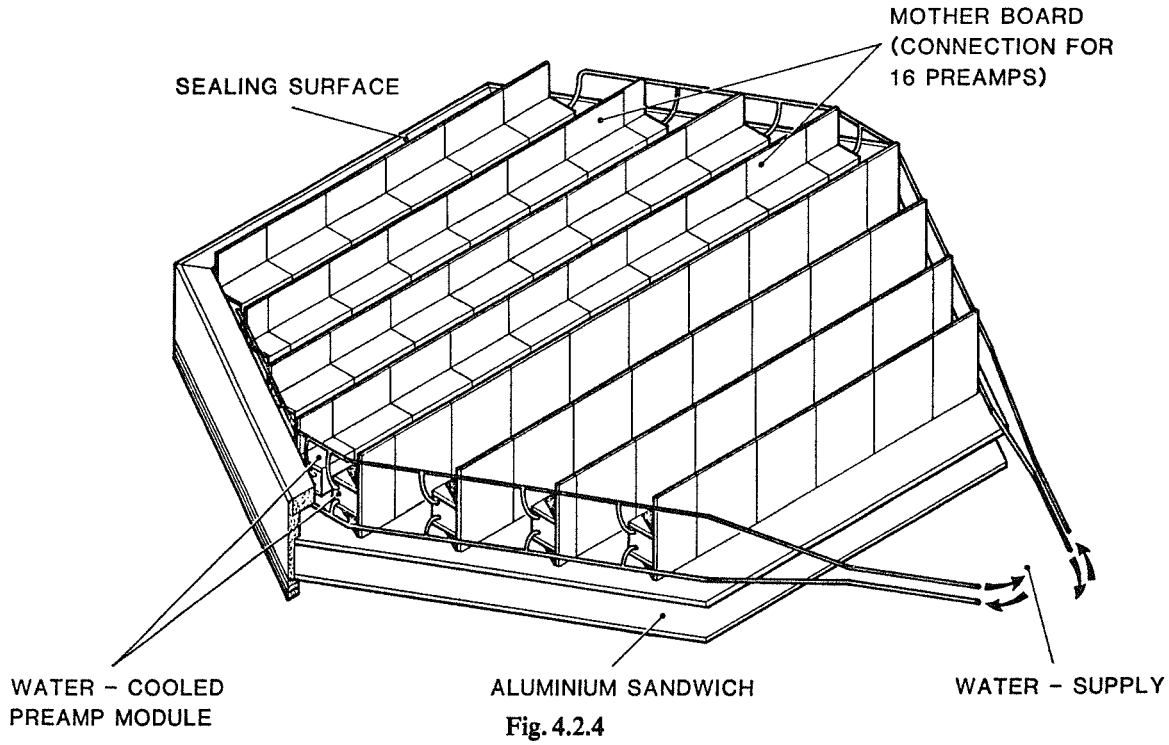

Fig. 4.2.4

- high stiffness to maintain these tolerances up to a working overpressure inside the TPC of 5 mbar;
- minimum amount of material (radiation length) and equal material distribution to obtain a good transparency for the end-cap e–γ calorimeter;
- minimization of the dead-zones between the neighbouring sectors to avoid loss of tracking information;
- very efficient heat removal from the preamplifiers to keep temperature differences below 0.5 °C in the amplification volume, the TPC structure, and on the outside of the TPC facing the e–γ calorimeter.

A view from the back (Fig. 4.2.4) shows the general arrangement of the preamplifier modules.

4.2.2 Cooling

Owing to the great importance of an effective cooling system, quite some effort has been devoted to this question and two possible solutions are being studied. Both use a liquid to transport the heat from the end-plate of the TPC to the outside of the magnet. The difference is the concept for transferring the heat from the preamplifiers into the liquid.

The first solution, which is presented in Figs. 4.2.5 and 4.2.6, uses argon gas to transport the heat from the preamplifiers to a water-cooled plane (heat exchangers) some 15 cm behind the preamplifiers. The gas flow inside the enclosed volume is driven by six centrifugal pumps.

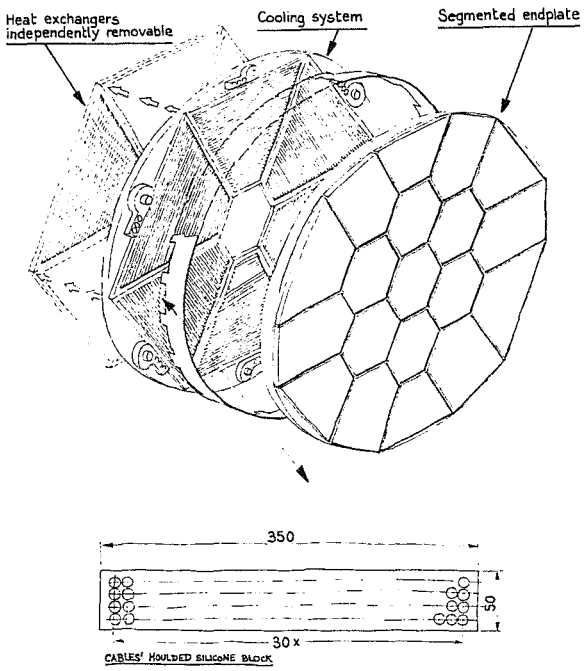

Fig. 4.2.5

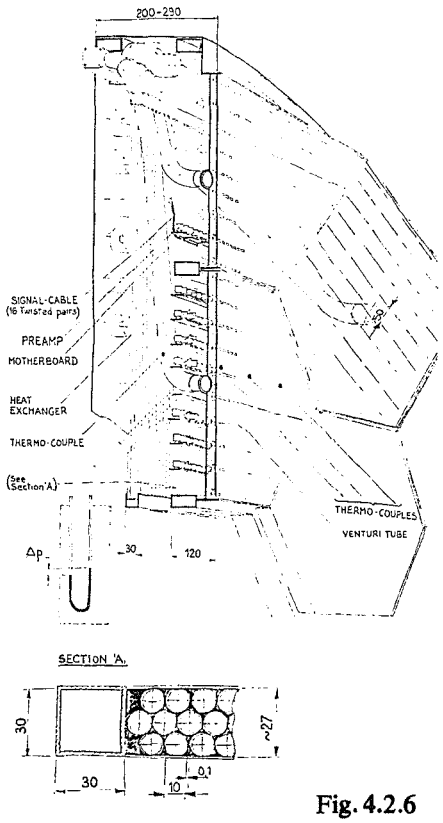

Fig. 4.2.6

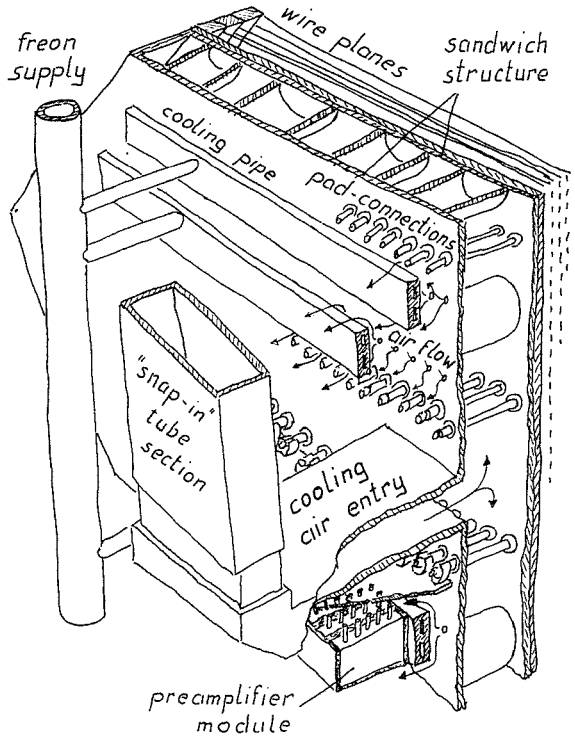

Fig. 4.2.7

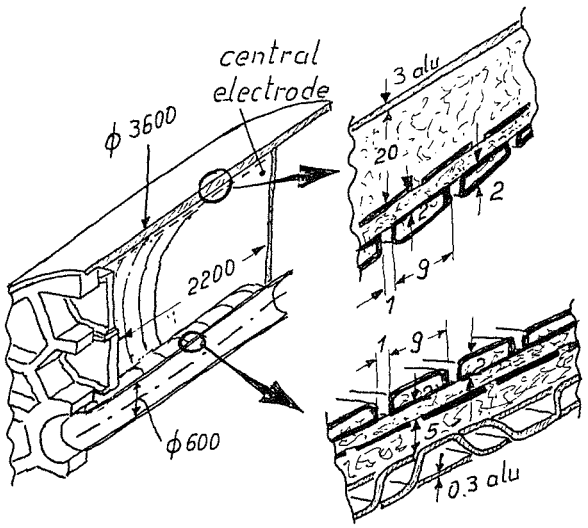

Fig. 4.2.8

The second solution (Fig. 4.2.7) collects the heat with liquid freon as close as possible to the heat-source. The preamplifiers are therefore in direct contact with the cooling pipes. In addition, a limited air flow integrated into the sandwich maintains the signal wires at the required temperature.

The merits of the first system are:

i) the tube arrangement for the cooling liquid is more simple;
ii) the argon, as cooling gas, avoids the penetration of oxygen into the TPC via possible leaks;
iii) the material distribution in the end-plane is slightly more homogeneous.

The merits of the second solution are:

i) the temperature differences Δt within the system are smaller;
ii) the access for maintenance work (preamplifiers, cables, laser system, alignment) is easier;
iii) no permanently moving elements (pumps) are required within the detector;
iv) the required air flow is much smaller.

These concepts will certainly develop further in the near future since it is necessary to find a common solution for the temperature stabilization elements for the TPC, the e–γ calorimeter, and the inner chamber.

4.2.3 Field cages

The outer and the inner field cages produce the electrostatic field, which must be adequately homogeneous. A possible mechanical design is shown in Fig. 4.2.8.

An important mechanical difference between the inner and outer field cages is that the thickness of the polyethylene insulator is 5 mm in one case and 20 mm in the other. This is due to the fact that the inner cage should be as thin as possible in radiation lengths, whereas the outer cage needs greater rigidity to avoid buckling. For the inner cage the mechanical strength has been obtained by means of an alu-double-wall.

The resistor chain might be located between the electrode structure and the insulator, as can be seen for the inner cage in Fig. 4.2.9.

4.2.4 Field alignment

In order to align the magnetic and electrostatic fields, provision has been made to tilt the entire TPC with respect to the magnet. This adjustment has a range of ± 3 mm at each end-plate of the TPC and allows a tilt in the vertical and in the horizontal plane. The inner chamber and luminosity monitor are being moved simultaneously with the TPC.

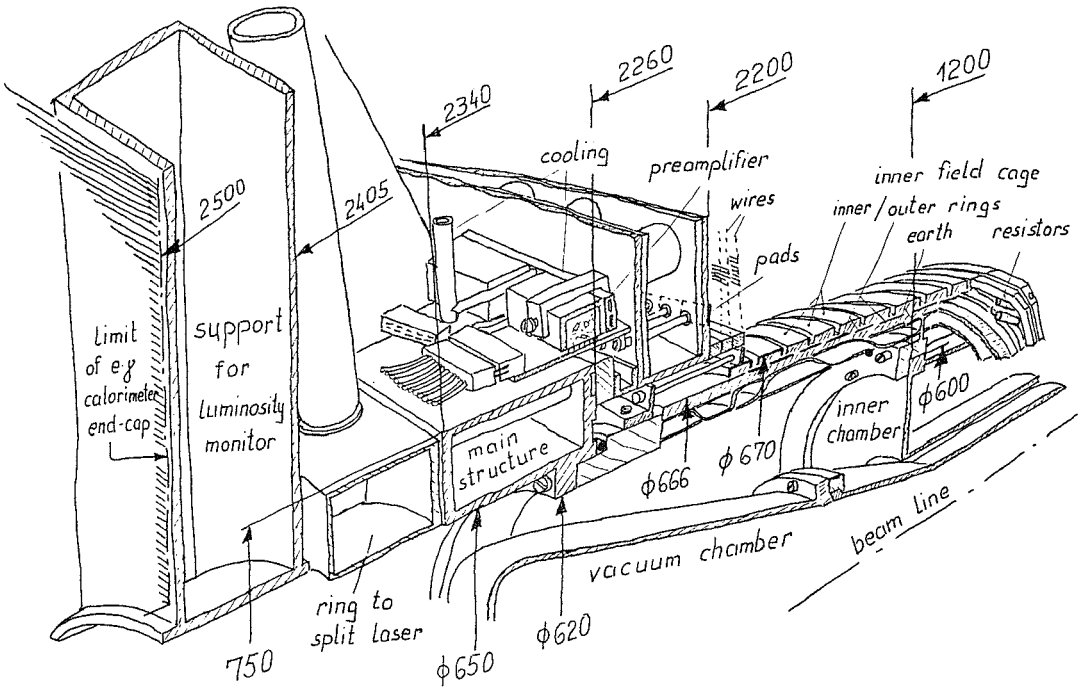

Fig. 4.2.9

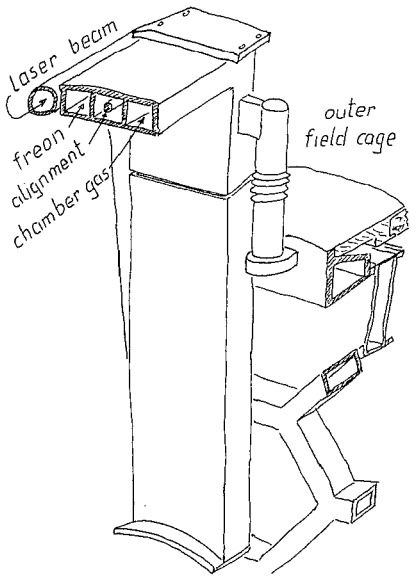

Fig. 4.2.10

4.2.5 System integration

The compatibility of the different subassemblies is shown in Figs. 4.2.9 and 4.2.10. The first figure shows the intended arrangement near the inner field cage and indicates the most important dimensions. The second figure shows the intended arrangement around the vertical foot on top and around the outer field cage. Missing in the first figure are the distribution for air-cooling and the cabling; in the second figure, the tubes for freon cooling. This has been done to avoid an overloading of these figures.

4.2.6 Installation tools

One set of tools (as shown in Fig. 4.2.11) will be provided for moving the TPC into its final position inside ALEPH. It consists of a pair of rails for the installation of the TPC after the assembly of magnet, coil, and e–γ calorimeter barrel. The supporting arms for these rails will be manipulated with the crane and fixed to the end-faces of the magnet. One pair of these fixation arms has wheels and a guiding facility for sliding the rails into place and retracting them after the installation of the TPC. Also, the four wheels of the TPC will be removed after the installation procedure. The detailed design of these tools will aim at a shape which requires as little space as possible between the TPC and the e–γ calorimeter.

Another tool which seems worth mentioning is shown in Fig. 4.2.12. It allows a wire chamber sector to be removed through the end-plate without removing the end-plate from the field cage. Two similar tools are required for the two types of sectors at the outer circumference.

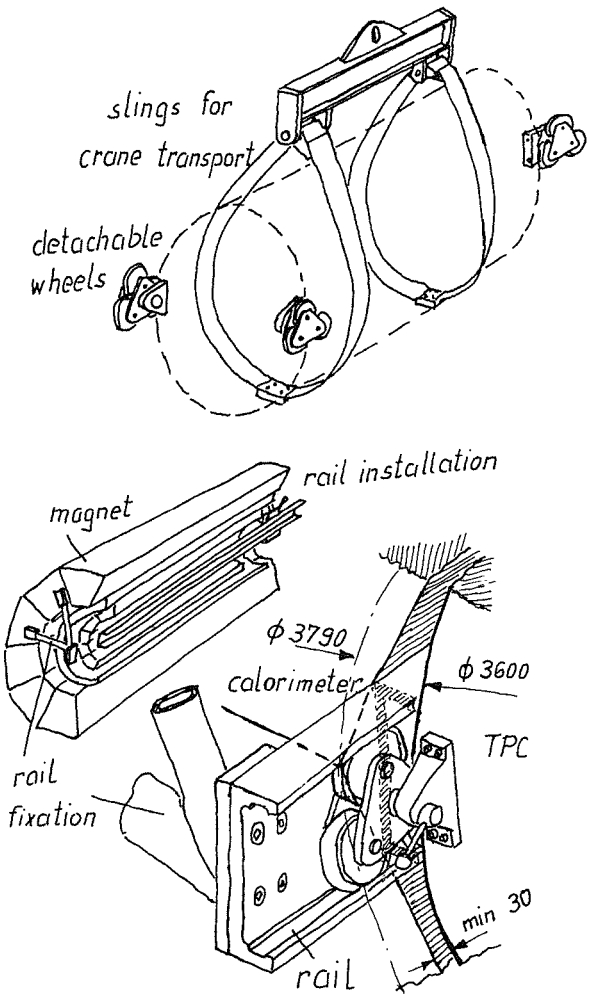

Fig. 4.2.11

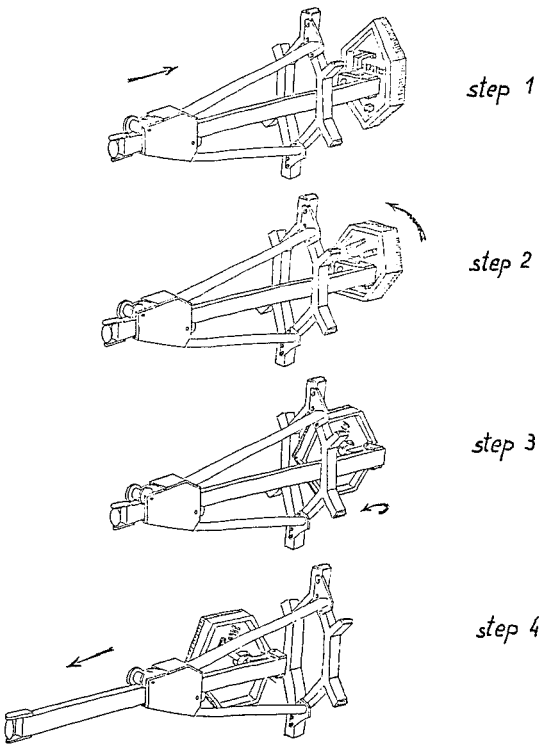

Fig. 4.2.12

4.3 Electronics

4.3.1 Introduction

The information concerning tracks of ionizing particles in the TPC is represented in the charge arriving at the wires and in the induced signals on the segmented cathode pads. The electronics must be able to determine the time of arrival of these signals as well as their amplitude. This will be done by a recurrent sampling of the pulse height of the signals from wires and pads during the entire drift time of $\approx 35\,\mu s$.

Table 4.3.1 gives an overview of the different parameters that limit the resolution of the over-all system. Column 2 lists the factors due to the chamber itself, while columns 3 and 4 give limitations coming from the measuring apparatus. In italics are those parameters where an increase in performance beyond the number given would mean a substantial increase in the cost of the electronics channel.

Table 4.3.1

Limiting effects for the resolution of the TPC

Parameter to be measured	Limitation due to: Chamber	Analog electronics	Digitizing/ Recording system
z-position (drift time)	Longitudinal diffusion ($\sigma \simeq 4$ mm = 60 ns)	Risetime (FWHM $\simeq$ 200 ns) $\simeq$ 200 ns	*Sampling frequency (10–13 MHz) Memory capacity (512 words of 8 bits)*
r, ϕ-position (pulse height on adjacent pads)	– Tranverse diffusion } 230 μm – Angular effect }	*Noise[a] at input of preamplifier* ($\sigma \simeq 600\,e^-$) Electronic pick-up[a] $\sigma < 50\,\mu V$ at preamplifier	*Resolution of ADC* $\sigma_{ADC} \leq 0.1\%$ *of full dynam. range*
dE/dx (pulse height on wires)	Gas gain	Uncritical	

a) Noise and pick-up are critical as the pad-signal cannot be increased arbitrarily if a maximum gas-gain is given ($\simeq$ 20 000).

4.3.2 System architecture

A functional block diagram of the pad and wire signal readout system is given in Fig. 4.3.1.

The first element in the chain which processes pad or wire signals is a low-noise preamplifier-cable driver. These preamplifier-cable drivers are constructed in thick-film hybrid form, and are mounted in groups of 16 on motherboards, directly on the end plate of the TPC.

The preamplified signals are transmitted to the digitizing system via $\approx$ 30 m of high-quality shielded twisted-pair cables.

This digitizing system is designed according to the FASTBUS specifications. It basically consists of three modules, the Time Projection Digitizer (TPD), the Time Projection Processor (TPP), and a Clock Fan-out Trigger Time Interpolator (CFTTI). The Segment Interconnect (SI) is a standard FASTBUS device.

The TPD module is 3U wide and contains (at least) 64 channels of receiver-shaping amplifier–digitizer electronics. The incoming signals are shaped and sampled at regular intervals, and the digitized amplitude information is stored in successive locations of a memory. Logic circuitry, in common to all channels in the module, does the first step in data reduction by measuring the recorded information locally and suppressing everything below a defined zero level (zero skipping). It is assumed that one crate will house seven TPD modules.

The CFTTI module (1U wide) controls the data acquisition in a crate. It distributes the sampling clock ($\approx$ 10 MHz) and the "trigger time" signal to the modules. This "trigger time" signal is synchronized to the clock and is derived from a randomly occurring event trigger signal, of which the time position is measured to ± 25 ns.

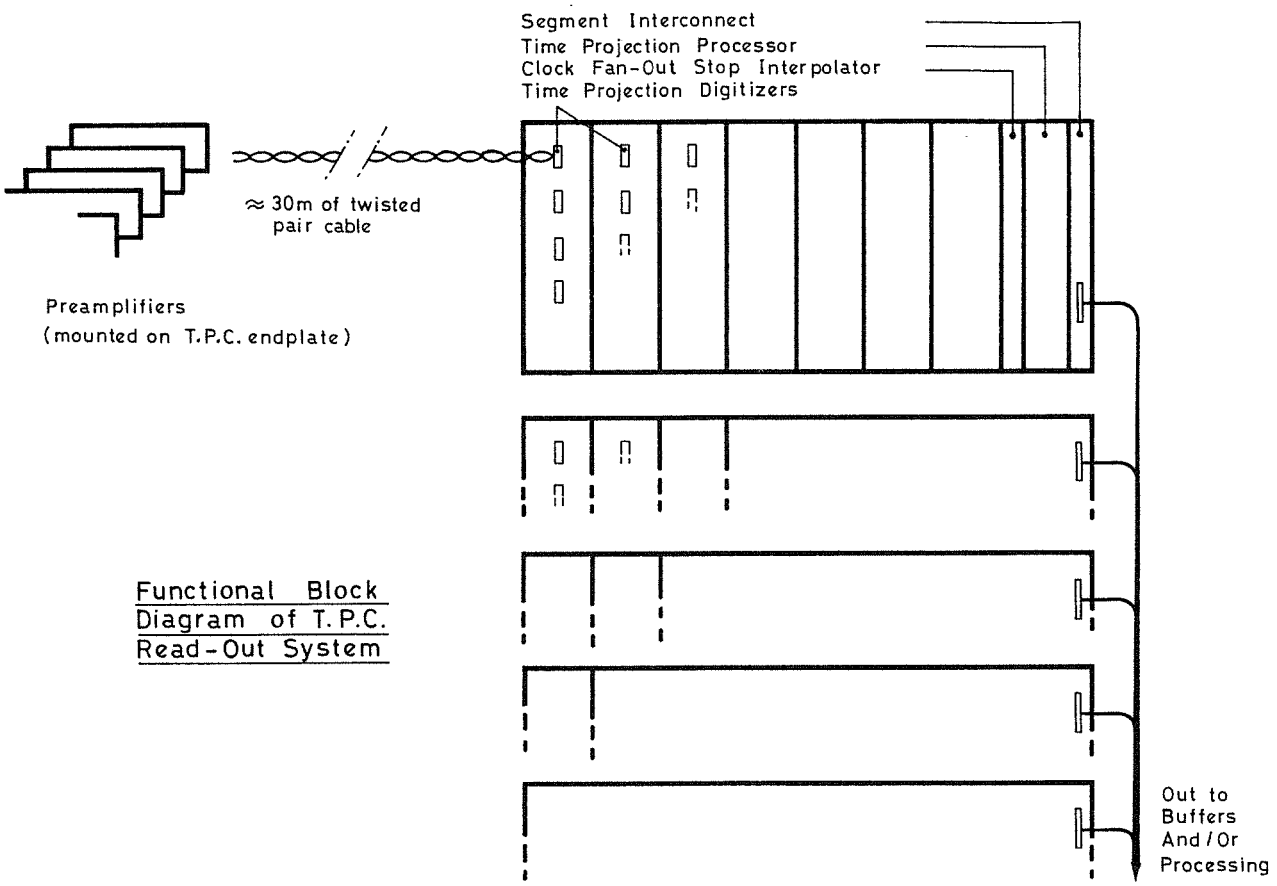

Fig. 4.3.1

The TPP module (2U wide) reads out the valid data from the modules in the crate. It is built around a 16-bit microprocessor, which is complemented by the necessary peripherals. The data from the modules are formatted, prepared, and stored as a block of information in a memory, from where it is accessible for readout.

The Segment Interconnect module is the communication channel to devices outside a crate. It interfaces the backplane of the crate (crate segment) to the cable segment or branch. For the TPC readout system a logical choice could be to group the electronics for all pads and wires of two sectors on a branch, which would result in six crates per branch.

It is foreseen to store the data from one branch store in a buffer memory, from whence it can be addressed for triggering, processing, readout, etc. (see layout of ALEPH data-acquisition system).

It may turn out to be more convenient and space saving to combine a CFTTI and a TPP module in one 2U wide module. Also, it is being considered to have one CFTTI and TPP set serve more than one crate, thus reducing the number of these modules required. The latter may be possible if the data volume to be read out from certain crates is relatively small, and so will take a short time to readout.

Under the assumptions made above, the total number of crates in the TPC readout system will be

for pads : $44000/7 \times 64 \quad \geq 98$,

for wires: $6000/7 \times 64 \quad \geq 14$.

If we assume that one rack will accommodate three crates, then the total number of racks will be ≈ 37.

4.3.3 The preamplifier

The preamplifier is a charge-sensitive amplifier which converts the charge from a pad or wire into a proportional voltage. It is basically an operational amplifier with capacitive feedback (see Fig. 4.3.2).

An amount of charge Q applied to input 1 will cause a voltage V_0 at the output:

$$V_0 = AQ/[(A+1)C_f + C_i] \approx -Q/C_f. \tag{1}$$

In spite of the fact that the input to ground capacitance C_i is 20–50 times higher than the feedback capacity C_f, it can be neglected in the denominator of (1), because the effective value of C_f at the input is amplified by a factor equal to the open-loop gain A, which is of the order of 10 000.

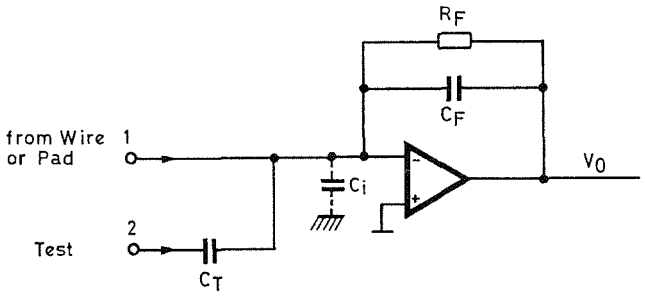

Fig. 4.3.2

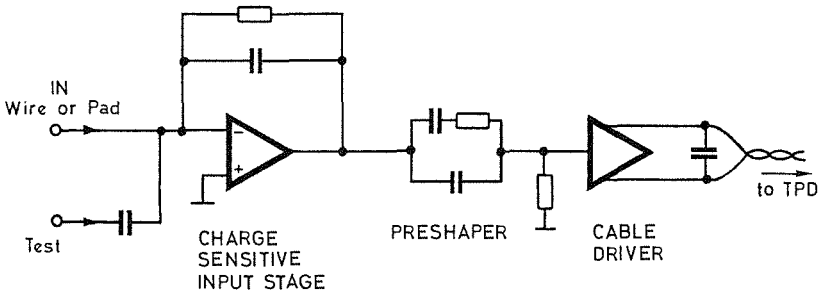

Fig. 4.3.3

For calibration purposes a second input is available. A voltage step at input 2 injects a charge $Q_t = V_t \times C_t$ into the capacitor C_f.

The charge accumulated on C_f will decay with a time constant $R_f \times C_f = 1\,\mu s$. The extremely low input leakage current of the operational amplifier, with a FET input, can be neglected. Using Eq. (1), the r.m.s. noise of 600 e^- will create an r.m.s. noise voltage of 0.096 mV at the output of the input stage, a result that does not depend on the details of the wiring of this stage but uniquely on C_f.

The next stage of the preamplifier is shown in Fig. 4.3.3. This "preshaper" acts as differentiator and reduces the probability of pile-up of subsequent pulses by shortening the tail of the pulse. Without this preshaping, a series of pulses arriving inside a few microseconds could easily reach the limit of linearity of the subsequent stages, especially that of the cable driver. An increase of the dynamic range of the cable driver, however, would mean an increase of the power consumption beyond our design target of 100 mW.

4.3.4 The shaping amplifier

The signal at the output of the "pre-shaper" is asymmetric, with a rise-time of the order of 100 ns and a fall-time of 1 μs. The signal is too short for the minimum sampling interval of CCDs as well as FADCs, and so further shaping is needed.

Figure 4.3.4 shows a diagram of the shaping amplifier. The two integrating stages produce a fairly symmetrical pulse of 200 ns peaking time (10–100%) and at the same time amplify the signal to the level required by the FADC.

Another way of looking at the smoothing of the pulse shape is to say that the shaping amplifier, acting as an integrator (or "low-pass" filter), attenuates the high-frequency components of the incoming signal. A beneficial side effect of this filtering process is that the high frequencies of the noise spectrum as well as from external pick-up will be equally attenuated and thus an important improvement in signal-to-noise ratio is obtained. Also, the cross-talk between twisted pairs in the 30 m cable, being less important at lower frequencies than at higher ones, will profit from this suppression.

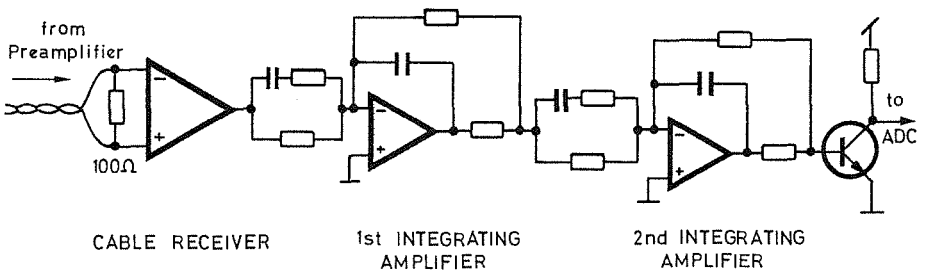

Fig. 4.3.4

Further study will shed more light on the necessity of attenuating the cross-talk after the cable. In contrast to this, the amplitude and frequency spectrum of pick-up from external sources will remain unknown up to the day when the 50 000 channels will be switched on. It is therefore essential to have a safety factor for noise rejection.

The shaping amplifier will be constructed in thick-film hybrid form, in collaboration with industry. The size of this package is expected to be $\approx 1 \times 0.5$ inch.

4.3.5 The time projection digitizer (TPD)

A functional block diagram of the TPD is shown in Fig. 4.3.5. It contains 64 signal processing channels and the necessary logic to read out the data from these channels.

The first element in the signal processing chain is a wide-band linear line receiver for the preamplified pad or wire signals. It can handle input signals up to 1 V.

The line receiver drives a shaping amplifier (see subsection 4.3.4), which transforms the original wire-signal to a signal with Gaussian-like shape. This shaping optimizes the signal-to-noise ratio and improves the two-track resolution by shortening the pulse. The signal shaping is accomplished by filter amplifiers. The output signal of the shaping amplifier has typically a FWHM of 200 ns.

The FADC is driven by the signal from the shaping amplifier. It measures its input signal every 80–100 ns and converts it into a digital quantity which is stored in successive locations of a memory. The FADC should have the equivalent of 9 bits to cope with the required spatial resolution between pads, and the signal variations due to Landau fluctuations and polar angle. A straightforward 9-bit FADC is too costly. Instead, we propose a novel scheme in which the dynamic range is expanded by inserting amplitude-dependent attenuation in the signal path, in synchronism with the signal sampling. The equivalent of 9-bit dynamic range and 7-bit resolution can be obtained with this method at lower cost, as it is less demanding on the linearity error.

The memory is a random access memory (RAM) connected in a circular fashion. Its size should allow the data from at least one event to be stored. With a clock frequency of 10 MHz (100 ns) and 40 μs max. drift time, at least 400 memory locations are required. Memories of adequate speed ($\leq$ 100 ns access time) and dimension (8 $\times$ 1k) are available. Double event buffering at the front end is thus easily implemented.

The readout logic, which is in common to all channels in the module, has the task of sequentially scanning the data stored in the respective memories. It retains data only if it is above a presettable threshold for later readout by the TPP. This part of the process of data reduction and preparation takes place simultaneously in all modules in a crate.

Two possible schemes have been retained for the read-out logic in the TPP module. In one case the data is read from the recording memories in all channels, reduced, and stored in an intermediate buffer memory, where it is kept ready for readout by the TPP. For each valid signal, a presettable number of samples or datawords (e.g. five) are read out and stored. In the other case, the recording memories are scanned and memory addresses of the first sample of data above threshold is stored in a buffer memory, thus forming a "hit" list. The readout by the TPP takes place by scanning the "hit" list memory to find the address of the first sample of valid data of a signal in the recording memory. After this first data sample, a presettable number of samples (e.g. five) are read out by incrementing the memory address counter.

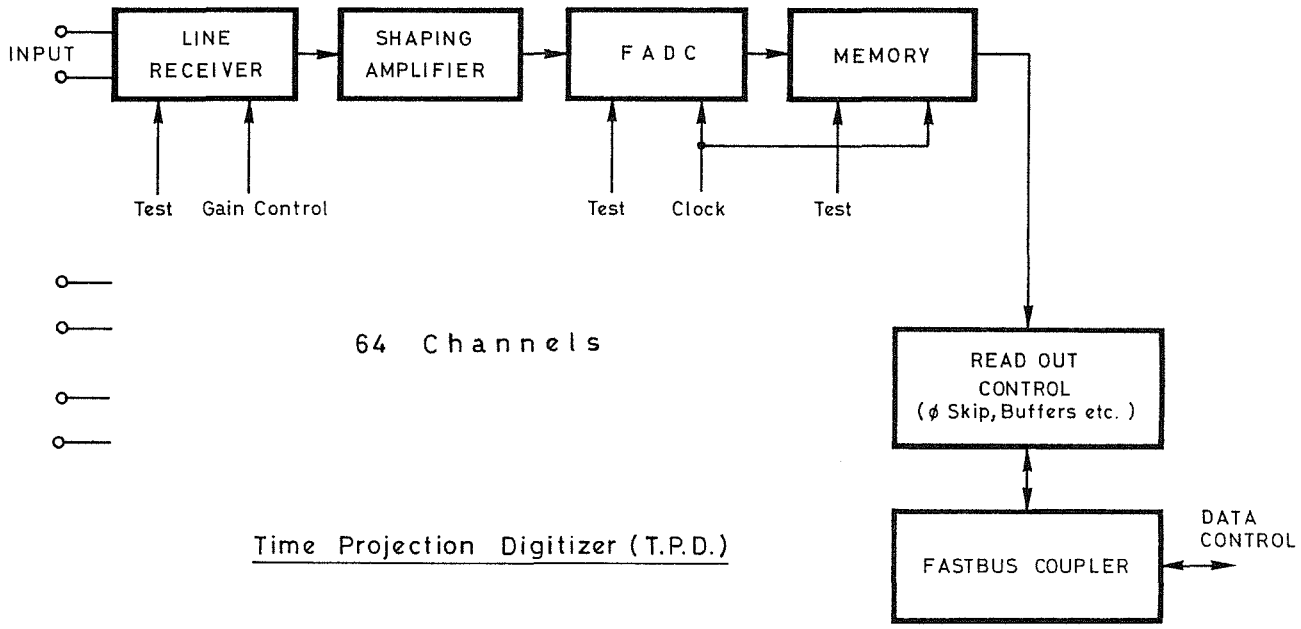

Fig. 4.3.5

Test signals can be injected at the input of the line-receiver and the FADC, whilst a digital test pattern can be injected into the recording memory.

A digital gain control is foreseen to equalize the gain of different channels as much as possible, as well as some digital control of critical d.c. levels.

4.3.6 The time projection processor (TPP)

The TPP organizes the data flow between a set of TPD-modules (typically one crate) and the main data-acquisition system. The unit (see Fig. 4.3.6) incorporates a microprocessor to achieve programmability and flexibility.

The module is built around the 68000 CPU chip, which is backed up by 32 (or 64) kwords of RAM, 8 to 16 kwords of EPROM, a Local Area Network (LAN) interface, and a "List driven" FASTBUS port.

This special FASTBUS port is necessary to make full use of the backplane bandwidth and, under control of a preloaded list, it is executing all input/output transfers using the RAM module as storage device.

As seen from the data-acquisition system, the LAN forms an independent path between the TPPs and the control computer(s). It allows a continuous diagnostic of the system behaviour without interfering with the data taking. The LAN is also a necessary tool for debugging the system.

The transmission standard and type of protocol are not yet chosen but should come from one of the existing standards.

The processor tasks can be divided into four groups:

a) data acquisition and formatting,
b) system behaviour checking,
c) calibration,
d) data processing and reduction.

Points (a), (b) and (c) should be implemented immediately, and (d) is foreseen as a later possible addition.

Data acquisition and formatting is the foremost task when the TPC readout system is active, and consists basically of a transfer algorithm that uses the "hit lists" or other information from the TPDs to generate the variables for the FASTBUS port list. The TPP reads the TPDs and generates a data block containing the valid data together with information such as time references, event number, etc.

The system behaviour check is a background task during data acquisition and takes samples of the data read out from the TPD modules. It generates statistics on the number (and type?) of hits on each channel and produces, in histogram form, an image of the behaviour of individual channels. This allows the system to detect faulty channels, even during data acquisition.

The result is available to the control computer via the LAN.

During calibration runs the TPP executes a set of routines which controls the response from the channels into which a calibration pulse has been injected. There will be a number of adjustments, such as over-all analog gain, offset level, and FADC reference voltage. The processor, knowing what has been injected, adjusts these variables until the required response is achieved. The same technique is used to define the individual channel threshold values.

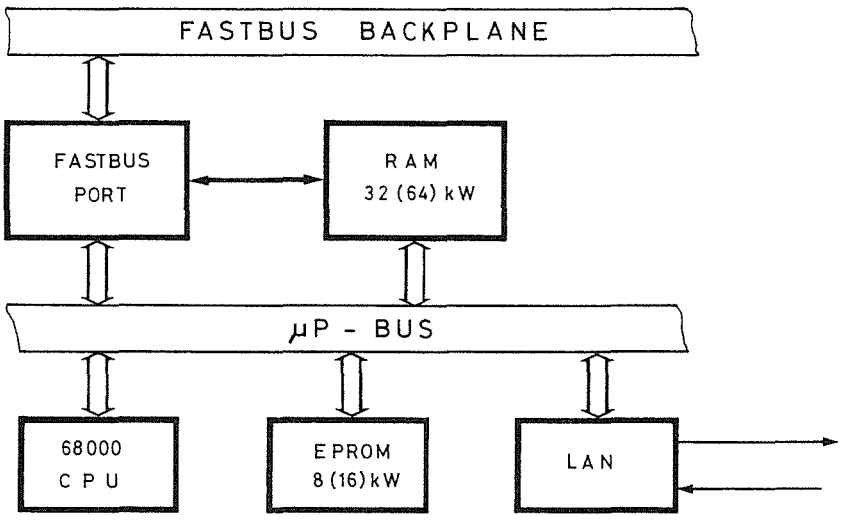

Fig. 4.3.6

The communication between the TPPs, the calibration electronics, and the control computer is via the LAN. The calibration values are also accessible to the control computer via the LAN. If, at a later stage, further on-line data processing and reduction is required, it will be easy to add the necessary firmware, because of the flexibility of the FASTBUS specification.

4.3.7 The clock fan-out and trigger time interpolator (CFTTI)

This module controls the data acquisition within a crate.

A functional block diagram is shown in Fig. 4.3.7. Its prime function is to distribute clock signals ($\approx$ 10 MHz) to the TPD modules in a crate and to measure the arrival of the event trigger and distribute it.

A crystal-controlled 40 MHz clock feeds an output fan-out and a trigger time interpolator. The time of arrival of a trigger signal is measured to 25 ns, within the clock period of 100 ns.

A bidirectional Input/Output port is implemented for conversation between the crate, the trigger and the calibration logic.

4.3.8 The test and calibration system

A test system is in preparation which allows injection of signals of controlled amplitude and controlled timing at the input of the preamplifiers. The control of this system will be via an independent LAN. Its setting can be done at low speed and should not interfere with the TPD data-acquisition system.

4.3.9 Timing of data recording and readout

The data recording by the TPD system will be started at the time of the Level 1 trigger signal ($\gtrsim 1\ \mu$s after beam crossing), when the TPC gate is switched on. Data recording will then take place over the full TPC drift time of 40 μs.

In case of a valid event, a Level 2 trigger arrives shortly after recording has stopped. The process of scanning the memories and zero suppression in the various TPD modules is then started and is accomplished in $\approx$ 2.5 ms.

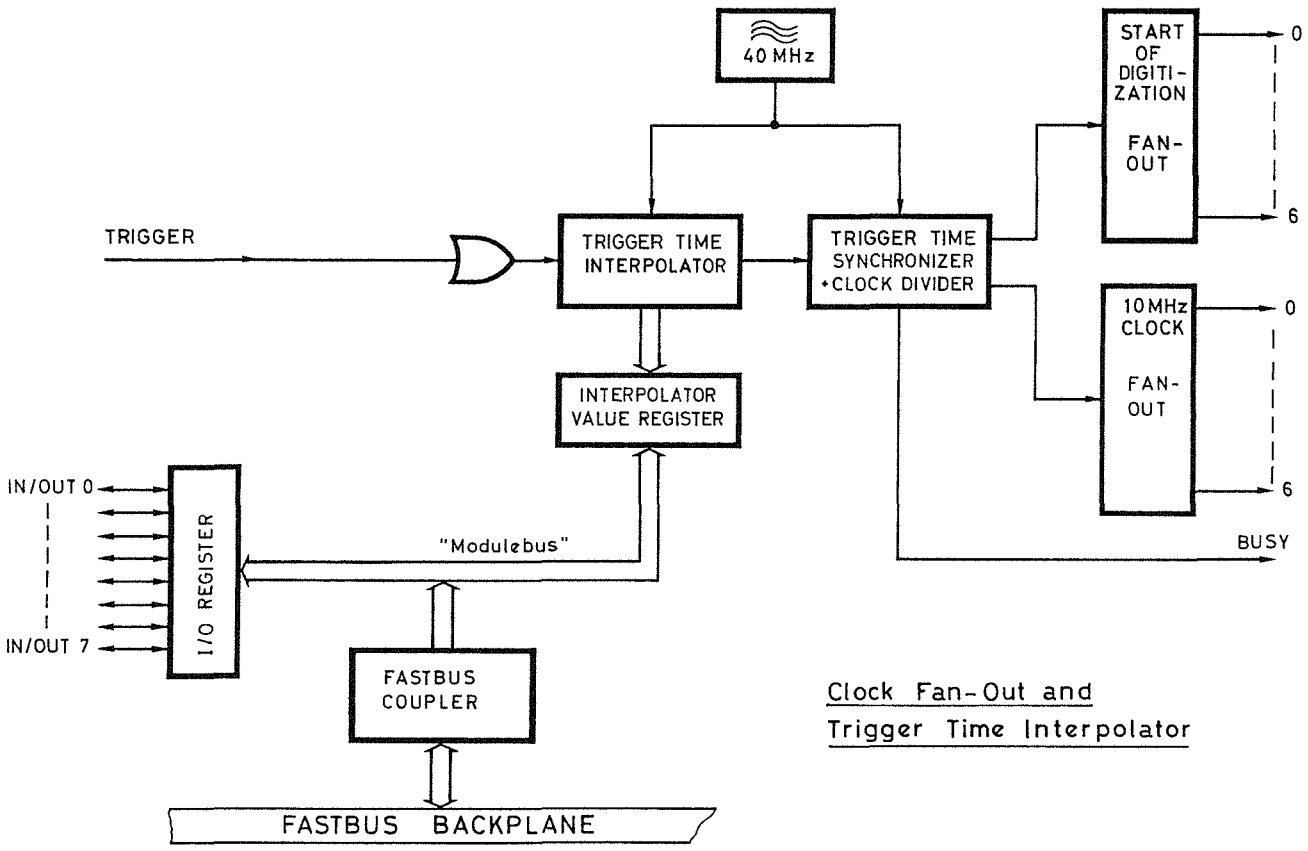

Fig. 4.3.7

4.3.10 Volume of data

The TPC produces a vast amount of raw data per event, which will be filtered and reduced in steps. An estimate of data volume can be made by assuming the following:

- Total number of wires: 6000
- Total number of pads: 44000
- Tracks per event: 20
- Wires hit per track: 340
- Pad rows hit per track: 20
- Pads of interest per row: 2 to 3
- Data recording time (400 slices of 100 ns): 40 μs
- Slices of interest: 5

The raw data corresponding to one event stored in the memories of one TPD module is: $400 \times 64 = 25\,600$ slices or samples. In one crate it is $25\,600 \times 7 = 179\,200$ samples.

Only a fraction of the samples contain useful information related to tracks in the chamber. Crates processing signals from wires will have relatively more useful information than those for pads.

If, for simplicity, we assume the case of a uniform distribution of hits over the wires, which gives approximately one hit in each wire channel, then, under the assumptions made above, the reduced data volume per crate will be:

$$6800/6000 \times 64 \times 7 \times 5 \simeq 2500 \text{ samples}.$$

The readout time of this information from the TPD modules by the TPP, and without taking into account protocol and data-formatting time overheads, will be approximately

$$2500 \times 100\,\text{ns} = 250\,\mu\text{s}.$$

Under the same conditions the volume of the data in crates serving signals from pads will be approximately:

$$1200/44\,000 \times 64 \times 7 \times 5 = 62 \text{ samples},$$

and the readout time of these data by the TPP will be approximately

$$62 \times 100\,\text{ns} = 6.2\,\mu\text{s}.$$

In the light of these readout time estimates, one TPP may be used to serve more than one pad crate.

4.3.11 Performance

We close the section on electronics with an estimate of this resolution as limited by the noise at the preamplifier and by the digitization error.

If 25 electrons of primary ionization are collected from a minimum ionizing track, this will produce a charge of 75 000 electrons at the input of the preamplifier (gas gain = 20000, 50% of the charge collected within the integration time, 30% of the signal induced on the pads). The noise of 600 e^- thus is 0.8% of the signal.

The minimum ionizing signal will correspond to 20% of the full dynamic range of the ADC. The digitization error corresponding to 9-bit resolution is 0.3%. The pulse-height measurement precision is therefore determined by the 0.8% error from noise, which is slightly below the design value of 1%. Referring to Fig. 4.8.1, where the position resolution for a 1% pulse-height error is given as a function of the distance of the track from the centre of the pad, it can be seen that the contribution to the measuring error from electronics is everywhere less than 75 μm, with an average of the order of 60 μm.

4.4 The laser calibration system

4.4.1 Introduction

In the ALEPH TPC the drift paths of the electrons from the track ionization can be as long as 2.2 m. The paths are determined by the electric and magnetic fields in the drift volume. Both are constructed to be as homogeneous and as parallel to one another as possible. In practice, there will be magnetic field deformations due to coil non-uniformities, end-plate misalignment, and the presence of unavoidable holes in the iron yoke; also, the electric field may be at an angle or deformed by clouds of space charge in the drift volume or surface charges in the field cage.

It is important to distinguish global and local field deformations. In contrast to axial wire chambers, TPCs do not suffer from the local track distortions caused by small drift cells. Our aim is to construct the ALEPH TPC in such a way that local field distortions are sufficiently small so that they do not have to be corrected. However, we expect to correct the long-range field deformations on the basis of laser calibration tracks.

In the proposed laser calibration we do not intend to map the electric and magnetic field distortions themselves; we aim rather to find the sagitta corrections directly for nearly straight tracks, since it is only these that matter. We expect to do this for a limited number of laser beam trajectories pointing back to the collision region. In this way we will have a coarse map in polar and azimuthal angles for sagitta corrections to stiff tracks. The laser calibration is therefore limited to corrections which vary slowly in these angles. More rapidly varying distortions, such as, for instance, those which are caused by the holes in the magnet yoke, must be dealt with on the basis of the magnetic field measurements.

Present understanding of the laser ionization mechanism in the TPC chamber gas suggests that Nd–YAG lasers are most suitable. However, it is realized that the nature of the ionization processes are not understood. Substantial modifications to our specifications are to be expected.

4.4.2 Laser calibration apparatus: Present design

Two lasers with specifications listed in Table 4.4.1, will be located on top of the ALEPH iron yoke. Each of them will serve half of the TPC. The lasers are in stable position there, and are accessible for maintenance and alignment. The stands will have a coarse adjustment for beam position and direction.

Table 4.4.1

Laser specification

Type	Q-switched Nd–YAG with frequency quadrupler
Mode	TEM_{00}
Wavelength emitted	265 nm
Pulse energy	4 mJ
Pulse duration	5 ns
Pulse repetition rate	$\leq$ 20 Hz
Beam spot diameter	2 mm, diffraction limited

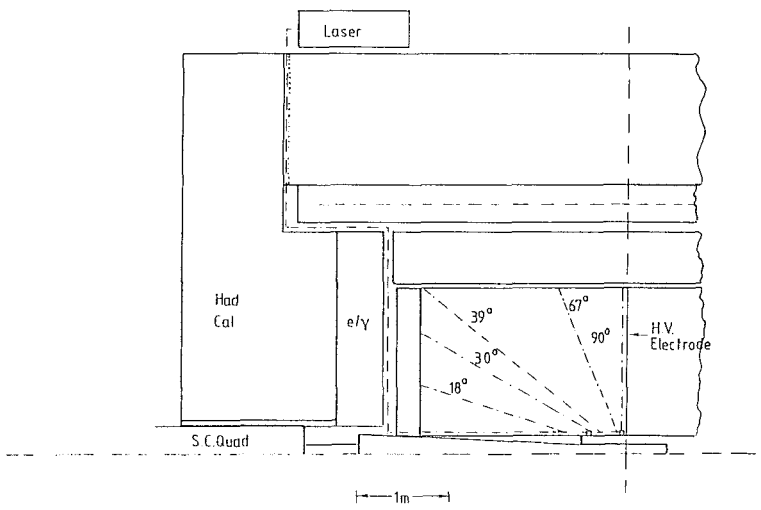

Fig. 4.4.1

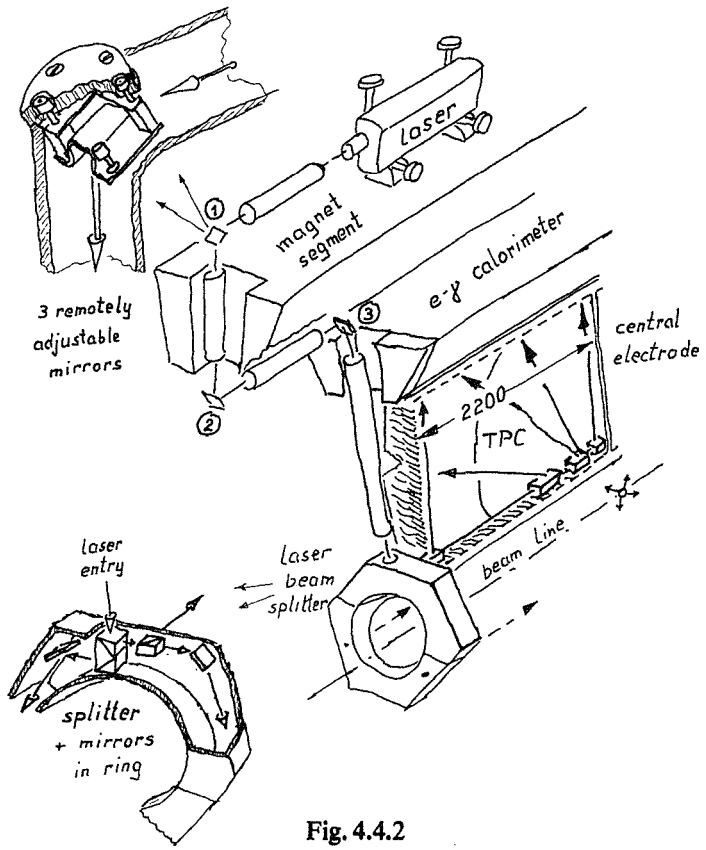

Fig. 4.4.2

The vertical beam will be distributed by a splitter (see Fig. 4.4.1) into three horizontal beams parallel to the e^+e^- direction, at azimuthal angles of 0°, 120°, and 240°. The splitter is a rigid ring-like structure fixed to the TPC frame. It is composed of two halves, which will be optically aligned in the laboratory with reference to a given direction of the incoming laser beam, and then located with two reference pins onto the end-plate. It contains all optical elements needed to create, transport, adjust, and monitor the three outgoing laser beams. The three optical elements used are: fused silica splitter prisms, beam reshaping lenses, and dielectric coated mirrors with maximum reflectivity at 256 nm.

Each of the three axial rays passes through the gas volume inside the TPC at 10 mm distance from the electrodes of the inner field cage. It then traverses five partially transparent quartz prisms, each of which splits off one ray into the appropriate polar angle as if it came from the e^+e^- interaction point. The prisms will be fixed directly onto the electrodes without special alignment mechanisms (see Fig. 4.4.2).

Adjustable mirrors are foreseen for the rectangular deflection along the TPC support arm. Only an angle adjustment around 2 axes must be made, but no translation of the beam. Small changes in the mirror angles will ensure the passage of the laser beam to the next mirror.

The coarse alignment of mirrors is done manually when the end-caps are removed. Once the end-caps are closed, fine adjustment will be done by piezo-electric crystals, which are commonly used in remote-control systems for optical apparatus. The necessary voltages are in the range up to 1 kV, by which corrections of ± 3 mrad can be achieved.

The prisms inside the TPC give a constant and accurate deflection relative to the incoming beam. Therefore the accuracy in the polar angle relative to the TPC frame is given by the accuracy of the incoming beam. The shapes of the different prisms are given in Fig. 4.4.3; the aperture (cross-section) is 10 mm × 10 mm. They will have a metal coating to minimize the distortions of the electric field.

For *beam position control*, each of the three mirrors mounted on the TPC arms will have a position detection device behind it. Only about 1% of the total beam energy is needed for the position measurements. The splitting is done by a 99% reflecting mirror. Quadrant detectors give analog pulses, from which the beam deviation from the centre can be calculated. This information is used to steer the beam by means of the piezo-electric crystals. Since the response of piezo-electric crystals is non-linear and the expansion of one piezo-electric mirror support induces a change in angular deflection in two directions, a feedback system controlled by a microprocessor is foreseen.

The *laser output is monitored* by means of the quadrant-type photodiode behind the first mirror. It will provide a signal proportional to the laser output power, as well as a timing signal for the TPC readout system.

The laser beam position monitors will consist of a fibre-optic pick-up matrix with UV grade fibres, e.g. QSF 400 UV, which have small attenuation losses at 256 nm; the readout of these monitors is done remotely by diode lines or diode matrix arrays.

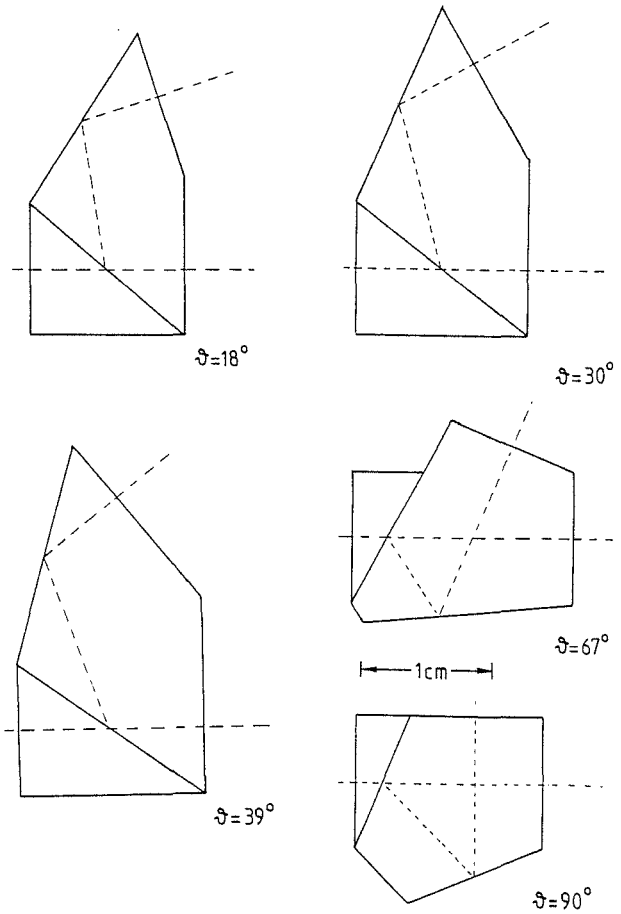

Fig. 4.4.3

4.4.3 Beam cross-section and divergence

The smallest possible size of a long laser beam is determined by diffractive effects and by the scattering on imperfect surfaces. The diffractive effects can be summarized by stating that a Gaussian beam profile will remain Gaussian if the beam transport is done by mirrors or lenses. No diffraction structure will occur except for a beam spread, which gives a diameter

$$w(z) = w_0 [1 + (\lambda z/\pi w_0^2)^2]^{\frac{1}{2}} \quad ;$$

where

w_0 is the starting diameter ($\sim 2 \times 10^{-3}$ m),
z is the length of beam ($\sim$ 10 m),
λ is the wavelength ($\sim 250 \times 10^{-9}$ m).

Using these typical values, one gets a relative spread $[w(z) - w_0]/w_0$ of $\sim$ 2%, which is very small.

The (incoherent) scattering on imperfect surfaces is much more important because it creates a diffuse halo around the beam core. It will be necessary to use optical elements of the best quality. We do not yet know how much effort will be required to reach our aim of having beams with effective diameters of a few millimetres throughout the TPC volume. After the drift, the track ionization has a Gaussian shape due to diffusion, which is σ = 1 mm in the rϕ plane and $\sigma \approx$ 5 mm along z. It should always be possible to measure the laser tracks with much better accuracy than the particle tracks because their measurement can be repeated.

4.5 Gating

4.5.1 Introduction

The TPC, as a continuously sensitive drift chamber of very long drift length, is severely limited in its operation in high-background environments. Part of the positive ions produced in the multiplication process near the sense wires will eventually move back into the drift volume, producing track-distorting space charges. The TPC must therefore be operated in a shutter-like or gated mode.

4.5.2 Principle of gating

In analogy to optical devices, the TPC would remain insensitive as long as no suitable event candidate is present (to be determined by an external trigger). Only in the case of such a pretrigger signal would an electronic shutter be "opened" and the TPC end-plate "exposed" to the particle tracks. One way of achieving this goal is to use a *gating grid*, which can be appropriately operated in order to be either totally opaque or transparent to drifting electrons approaching the detection plane of the TPC. Figures 4.5.1(a,b) show the arrangement of grids in a gated TPC. Since the gating grid is located inside the drift space of the chamber, a suitable common bias must be applied to *all* gating grid wires so as not to absorb any field lines coming from the central drift field, which would result in loss of primary charge. This bias is denoted $\bar{V}_G$. To close the gating grid, opposing voltages $\pm\Delta V_G$ are provided symmetrically on neighbouring wires, such that none of the drift field lines can pass through the grid (see Figs. 4.5.1 a and b).

OPEN AND CLOSED GRID CONFIGURATIONS

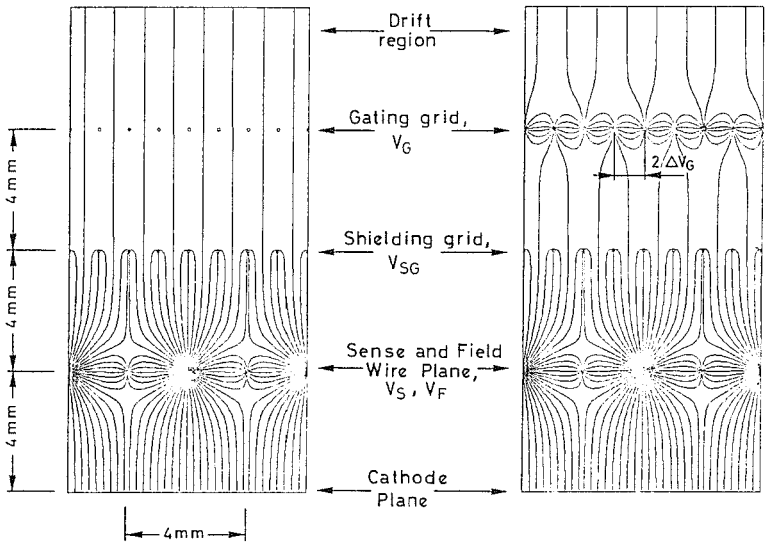

Fig. 4.5.1

4.5.3 Tests and results

Referring to Fig. 4.5.2 the gating grid is to be operated with the potentials:

$$V_+ = \bar{V}_G + \Delta V_G(t),$$
$$V_- = \bar{V}_G - \Delta V_G(t).$$

Using a small test chamber, good values for $\bar{V}_G$, i.e. "gate open" voltage, were established. In our search for a minimum ΔV_G, sufficient to close the gate, we were concerned about the dynamic aspect of gating; lower ΔV_G's produce smaller pick-up transients. Electrons from two collimated ^{90}Sr sources produced primary ionization in the drift space of the test chamber. The electron current in the proportional cell of the TPC was directly monitored, as well as the ion current at the central membrane of the drift field.

In Fig. 4.5.3, electron and ion currents are plotted against $\bar{V}_G$. It can be seen that even at full transparency of the gate, the ion current is only about 10% of the electron current. Calculations of the field configuration for the three-grid arrangement in our geometry show that in order to satisfy the transparency condition, $\bar{V}_G$ must be chosen such that the field between gate and shielding grid is twice as large as the drift field. This is indeed confirmed by our measurements. Also, measurements of the current as a function of ΔV_G on the gating grid are shown in Fig. 4.5.4. When $|\Delta V_G| \geq 15$ V, the current is reduced to noise level, indicating that the gate is effectively closed.

If care is taken in the manner in which the gating voltage is applied, the transient pick-up on the sense wires under these conditions (1 mm wire spacing, $\Delta V_G = \pm 20$ V) can be as low as 8 mV, which is 1/25th of the dynamic range. On the pads it is about one order of magnitude lower. These pick-ups will not give rise to any problem.

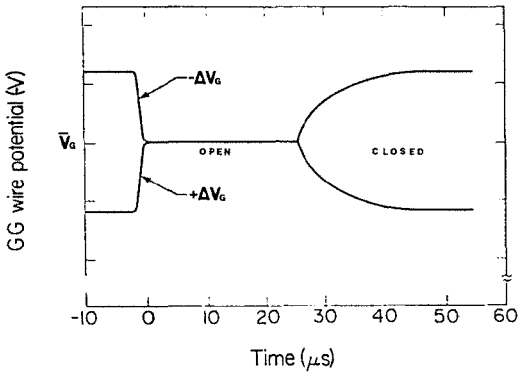

Fig. 4.5.2

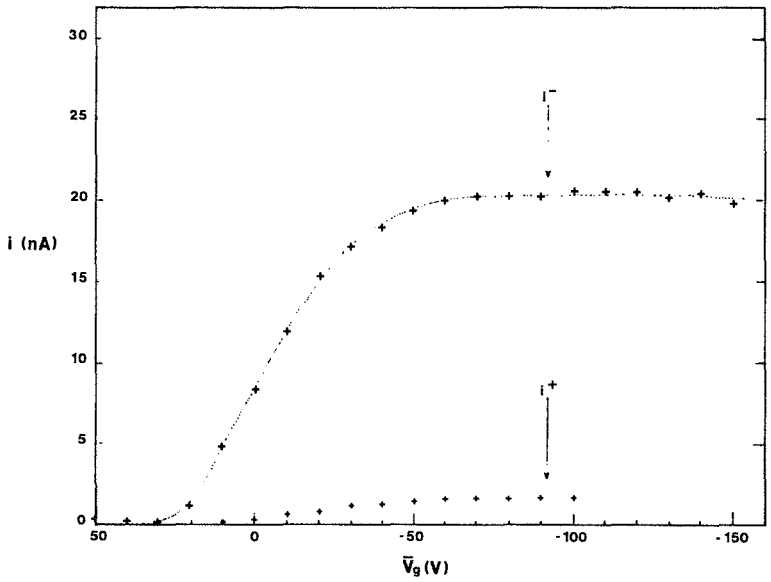

Fig. 4.5.3

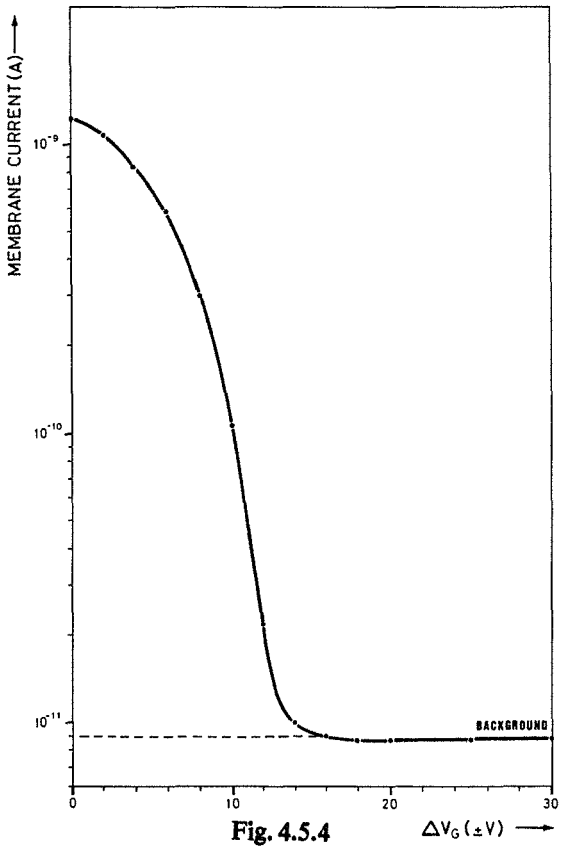

Fig. 4.5.4

4.6 The field cage for the ALEPH TPC

4.6.1 Introduction

The active volume of the ALEPH TPC consists of an outer cylinder of length 4.4 m and 3.6 m diameter and an inner cylinder of about 60 cm diameter. This volume is divided into two halves by a plane central partition which serves as the negative electrode. The working field will be ~ 200 V/cm (i.e. 45 kV over-all), but it is foreseen that tests will be performed up to ~ 270 V/cm (60 kV over-all). This field will be maintained by a system of electrodes on the cylindrical walls.

4.6.2 Physics constraints

Particles produced in e^+e^- interactions traverse the walls of the TPC, making it essential that the field cage should present as little matter as possible to these particles compatible with the safe working of the TPC. This is particularly true of the inner field cage.

In order to reduce the problems of calibration of distortion, it is desirable that the errors introduced by electric field inhomogeneities in the trajectory of the drifted electron should be small compared to other effects (e.g. magnetic field inhomogeneities). Inadequacies of the present Berkeley field-cage performance underlie the difficulties of this pioneer device.

4.6.3 Proposed design

A possible solution for the electrode system is shown in Fig. 4.6.1. The electrodes are 9 mm wide and 2 mm high with an interelectrode gap of 1 mm. These are mounted on a dielectric of 1 mm thickness. Shielding electrodes are applied to its back surface. The insulator which separates the electrode structure from ground potential serves also as the mechanical support.

The fact that the inner field cage should have as small a thickness (measured in radiation lengths) as possible whilst the outer field cage must have a minimum rigidity to prevent buckling, leads to different designs for the electrode support structure in each case.

Table 4.6.1 shows the characteristics of the inner field cage.

Table 4.6.1

Element	Material	Thickness (mm)	Radiation length (cm)	Radiation length (%)	Total (%)
Supporting shell	Al	0.6	9	0.5	18
Insulator	PCTFE	5	48	1	36
Electrode support	Fibre-glass epoxy laminate	2	25	0.8	31
Electrodes	PCTFE metal-coated	2	48	0.4	15
TOTAL		9.6		2.7	

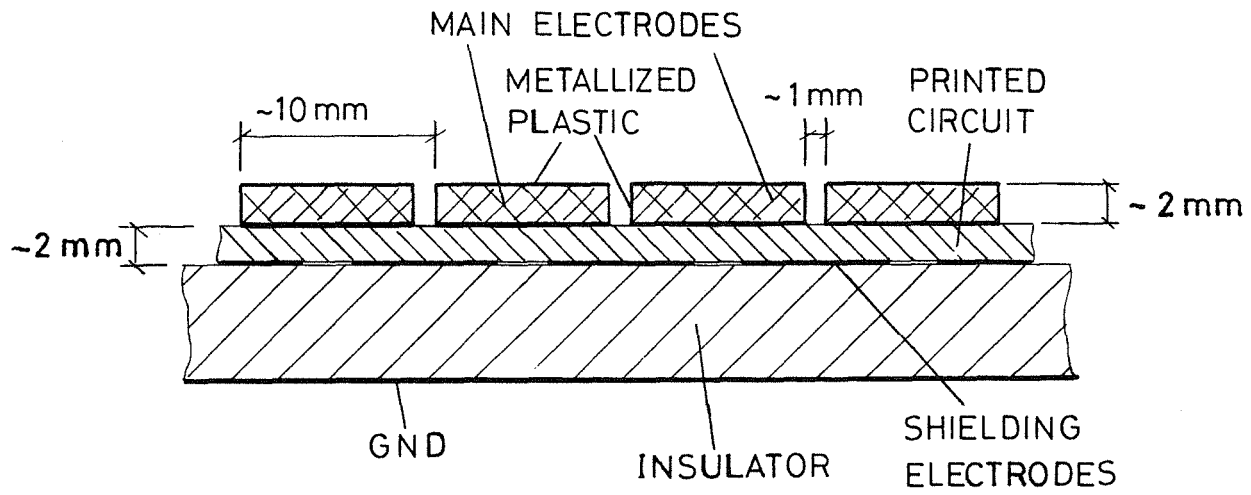

Fig. 4.6.1

Polyethylene is being considered as the insulator mainly because of its availability in the required dimensions; several other plastics are equally suitable.

It is intended to install an interior rather than exterior resistor chain for both the inner and outer parts of the field cage. The mechanical and electrical engineering design is simplified since there would be no need to provide individual voltage feed-throughs. However, heat generated in such a resistor chain is a potential problem. The resistor chain might be installed as shown in Fig. 4.6.2. In this solution the chain can, if necessary, be gas cooled.

A construction of the outer field cage, alternative to the one discussed in subsection 4.2.3, is modular and consists of hoops of fibre-glass epoxy laminate, 20 cm wide and 1 cm thick, on which the electrode system is mounted. The assembly is shown in Fig. 4.6.3.

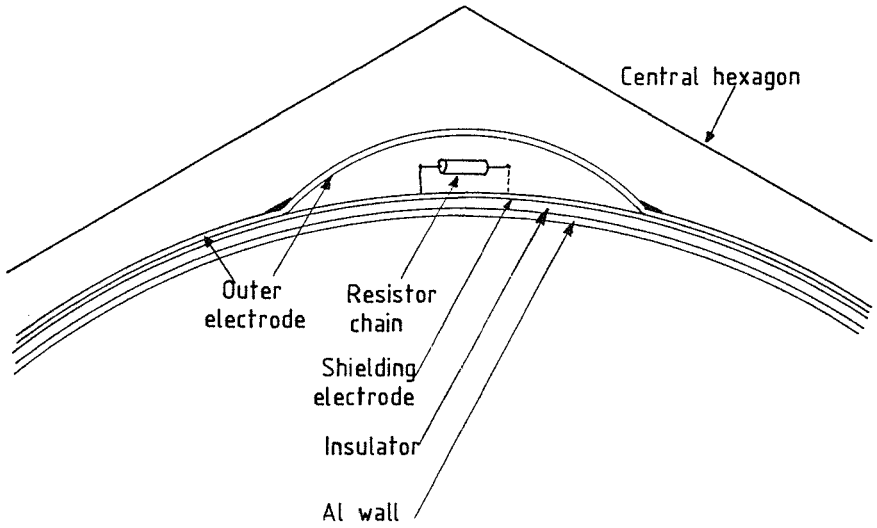

Fig. 4.6.2

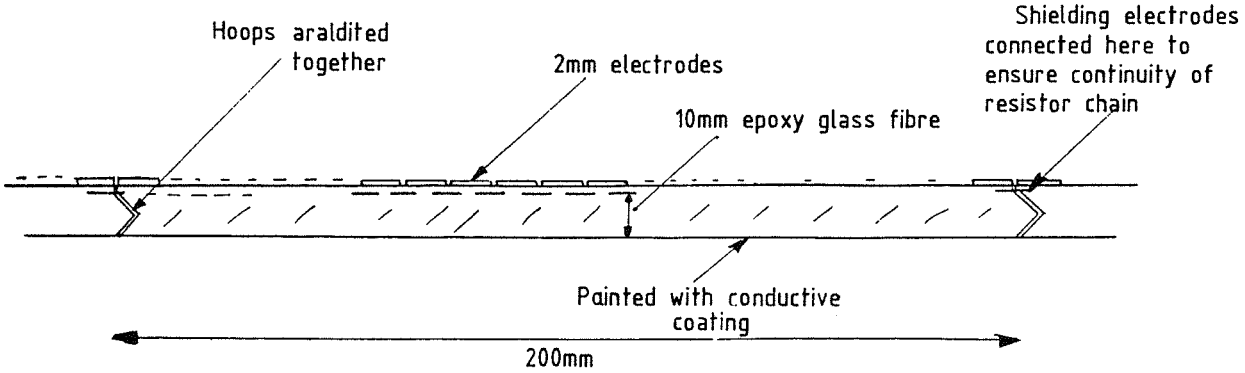

Fig. 4.6.3

4.6.4 Remarks

The design elements presented here are tentative and represent our present knowledge. The final design will probably differ from the above. In particular, if conductive coatings are shown to fulfil the necessary criteria of uniformity and cleanliness, they could simplify the field-cage design.

In the present proposal we are not exploiting the insulating properties of materials to the full. If the practical difficulties of rolling foils can be surmounted, then it is conceivable that insulators of the order of 1 to 2 mm in thickness can be manufactured. This would clearly contribute to reducing the thickness of the inner field cage and could also be used for the outer cage, together with a foam or honeycomb structure to prevent buckling and to reduce the over-all detector weight.

The above points are being actively investigated and tests are being prepared to study the following specific problems:

i) Dielectric strengths of various materials under TPC operating conditions.
ii) Breakdown properties of argon–methane mixtures.
iii) Electrostatic distortions for various electrode designs.
iv) Convection effects.

4.7 Gas system

The gas needed for a good performance of the TPC should have the following properties: i) the drifting electrons should undergo small diffusion transverse to the magnetic field; ii) the drift velocity should be high; iii) the electron attachment probability should be small.

The gas which suits best these requirements is a mixture of argon and methane (10–20%). The exact mixture has still to be found.

4.7.1 Filling and running

The volume of the TPC is $\sim 42\ m^3$.

1) Flushing argon, about five times the volume of the TPC, will reduce the amount of air to about 5×10^{-3}.
2) This will be followed by flushing about five times the volume with the proper mixture, leading to an oxygen content of ~ 10 ppm.
3) For normal operation we foresee reduced continuous flow recirculation with purification. The recycling flow rate will depend on the TPC construction, i.e. leak and outgassing rates. A level of O_2 contamination of $\lesssim 10$ ppm could be handled by OXISORB purifiers. A small fraction of the gas flow will be vented and replaced by fresh gas to compensate for the removed quenching agent and for N_2 contamination.

The operating pressure has to be 3–5 mb above the atmospheric pressure, in order to accommodate pressure transients caused by the zone ventilation. Limitations in the response time of the gas system to fast ($\sim$ 1 min) pressure jumps will create temporary alarm situations whenever the TPC pressure is below atmospheric.

4.7.2 Monitoring and control

The gas mixture, pressure, and purity, as well as temperature, will be monitored and fully or partially servo-controlled. This will be done by measurements at $\sim$ 1/2 hour intervals of the drift velocity, the resolution, and the signal attenuation by attachment. Details of various safety aspects, such as interlocks, pressure, and gas leak detection, will be co-ordinated with other parts of ALEPH.

4.7.3 Location

The monitoring equipment and the gas control system comprise four racks, including the recirculation pumps and purification loop, and should be situated reasonably close to the detector. If required by safety rules, the gas control system will be made "explosion proof" and/or enclosed in an inert atmosphere.

The storage for premixed gas will be on the surface. Because of the vertical pressure gradients, the exhaust requires a booster pump. This exhaust line can be shared with other ALEPH components. Emergency procedures and stand-by conditions between operation periods are to be defined within the framework of the general safety regulations.

4.8 Performance

4.8.1 rφ spatial resolution

The coordinate measurement with cathode pads relies on the measurement of the charge induced on the pads by the avalanche on the proportional wires. The resolution is governed by the following factors: a) electronic noise [1,2]; b) diffusion of the electron swarm drifting towards the anode [3]; c) spread of the ionization collection along the wire due to the E × B effect and to the crossing angle of the track with respect to the anode wire [4,5,6]; and d) fluctuation in the size of the avalanche on each wire contributing to the pad signal [5,6].

a) Electronic noise

The amplitude of the induced signal on a pad, due to an avalanche at a position x along the wire, is well described by the "pad response function" [1,2]

$$P(x) = A \exp[-(x-x_0)^2/2\sigma^2], \tag{1}$$

where x_0 is the position of the centre of the pad and A is the effective amplitude. The width σ depends on the geometry of the cell (pad size, wire spacing, distance between pad plane and anode wires).

The comparison of the induced signal with the electronic noise determines the number of pad signals that can be used to calculate the x coordinate. In our detector, the requirements of a dE/dx measurement limit the acceptable gas amplification to $\approx 10^4$, giving a noise-to-signal ratio of about 1%. This figure implies that only two or three pads can be used for the coordinate measurement. Two algorithms can be used to calculate the x coordinate: one using the two highest pad pulse-heights (P_i, P_{i+1}), and the other using the pulse heights of the two pads adjacent to the one with the largest signal (P_{i-1}, P_{i+1}). They are:

$$x = \sigma^2/s \ln(P_i/P_{i+1}) + (i + 1/2)s, \tag{2a}$$

$$x = \sigma^2/2s \ln(P_{i+1}/P_{i-1}) + is, \tag{2b}$$

where s is the pitch of the pads. The error on the measurement due to the electronic noise is, respectively,

$$dx = \sigma^2/s \sqrt{[(dP_i/P_i)^2 + (dP_{i+1}/P_{i+1})^2]}, \tag{3a}$$

$$dx = \sigma^2/2s \sqrt{[(dP_{i+1}/P_{i+1})^2 + (dP_{i-1}/P_{i-1})^2]}, \tag{3b}$$

where dP_i is the electronic noise on the i^{th} pad.

Figure 4.8.1 shows the calculated resolution as a function of the position along the pad row: the dashed line refers to (3a) and the solid line to (3b). The pad response function (1) has been used with a pad size of 6 mm, position of the pad centres at 0 ± 6 mm, and a σ of 3.2 mm. A noise level of dP/A = 1% has been assumed.

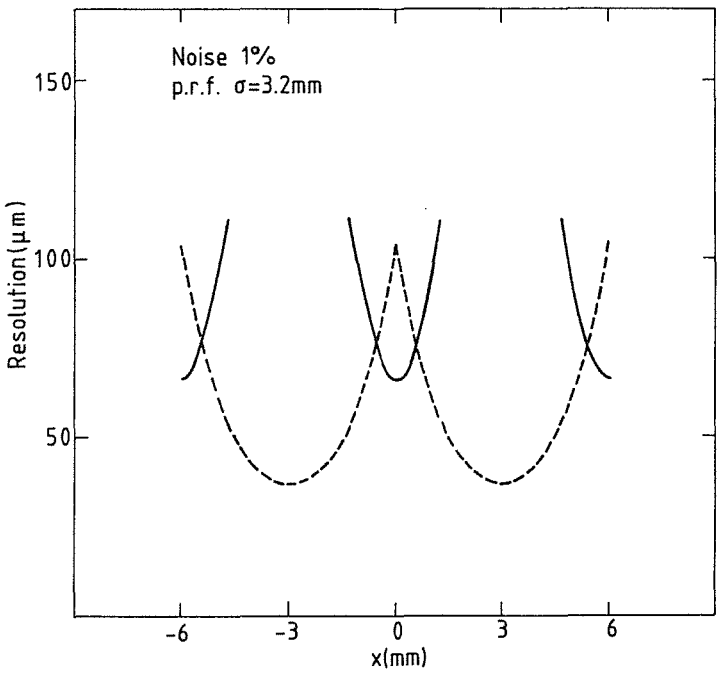

Fig. 4.8.1

We note that the best results are obtained using the algorithm (2b) when the particle trajectory crosses the pad row in a region near the centre of a pad and the algorithm (2a) otherwise. In addition to the noise effect, there is a systematic error due to uncertainties in the relative calibration of the pad signals.

From (2) it follows that a fractional error ε in the relative calibration produces a systematic shift,

$$\Delta x = \sigma^2 \varepsilon / s \quad \text{for the algorithm (2a) and}$$

$$\Delta x = \sigma^2 \varepsilon / 2s \quad \text{for the algorithm (2b).}$$

We see that for $\varepsilon = 4\%$ the maximum systematic error is $\approx 50\,\mu$m.

b) Diffusion

The contribution of the diffusion to the rϕ resolution can be calculated using the data of the PEP-4 collaboration [3].

For 1 m drift length, no magnetic field, and 1 atm pressure, the r.m.s. of a single electron diffusion is $\sigma_D = 4.1$ mm. The presence of the magnetic field reduces the diffusion on the plane normal to B according to

$$\sigma_D(B) = \sigma_D(0)/\sqrt{(1 + \omega^2\tau^2)},$$

where ω is the cyclotron frequency and τ the mean collision time. For B = 15 kG and a drift field of 150 V/cm we expect $\omega\tau = 7$ at atmospheric pressure. The single electron transverse diffusion is reduced to $\sigma_D = 0.58$ mm.

The error on the centre of gravity of the diffused ionization electrons is $\sigma_d = \sigma_D/\sqrt{N}$, where N is the total number of electrons collected on the wires. In our detector $N \simeq 32$, so that we expect

$$\sigma_d \simeq 100\,\mu\text{m}\sqrt{D},$$

where D is the drift length in metres.

c) Angular effect and E × B effect

Figure 4.8.2a shows the projection on the wire plane of a particle track parallel to this plane and making an angle α with the normal to the anode wire. When $\alpha = 0$, the ionization clusters produced by the incident particle are collected at

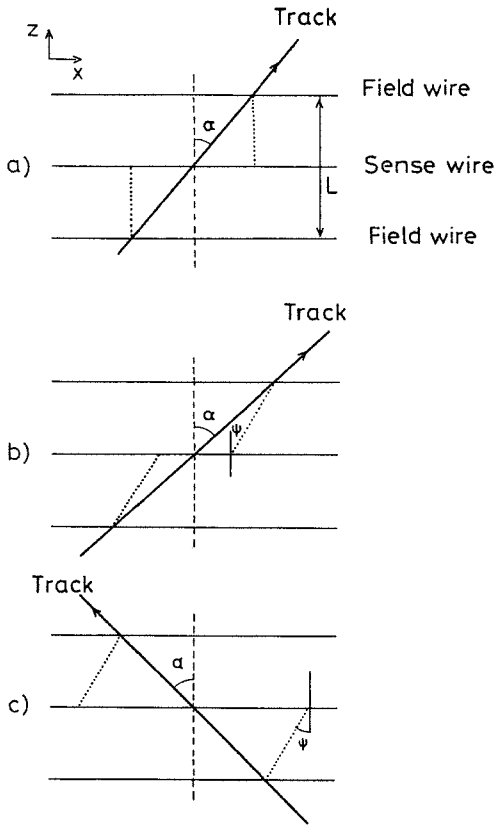

Fig. 4.8.2

a point on the anode wire (neglecting diffusion). When $\alpha \neq 0$ the clusters are spread along the wire in a region $\pm L \text{ tg } \alpha/2$, L being the cell width. Neglecting electronic noise, the precision attainable in the measurement of the coordinate of the crossing point of the track is

$$\sigma = K\sqrt{(L/12\,N)}\sqrt{\cos\alpha}\,|\text{tg}\,\alpha|\,,$$

where N is the number of primary ionization clusters per unit length produced by the minimum ionizing particle, and K is a factor that takes into account the fluctuations in the cluster size and is approximately 1.5 [4].

Near the anode wire the electric and magnetic fields are not parallel, and the electrons acquire a drift velocity component along the E × B direction. This causes the electrons to drift along a trajectory (in the z–y plane) at an angle ψ (the Lorentz angle) with respect to the normal to the wire. The situation is illustrated in Figs. 4.8.2 (b–c). As a consequence, the electron swarm is spread along a region $\pm L(\text{tg}\,\alpha - \text{tg}\,\psi)/2$. The precision attainable is

$$\sigma = K\sqrt{(L/12\,N)}\sqrt{\cos\alpha}\,|\text{tg}\,\alpha - \text{tg}\,\psi|\,.$$

The value of tg ψ is given by the mean value of $\omega\tau$ along the electron trajectory.

In our geometry the pad signal receives contributions from several wires. This led to an improvement of the resolution with respect to the case of only one wire contributing. Indeed, taking as an example the case of the E × B effect at 0°, the measurement of the position is the average on several independent measurements, one for each wire, weighted according to their contribution to the pad signal:

$$x = (\Sigma\, w_i Q_i x_i)/(\Sigma\, w_i Q_i)\,,$$

where x_i is the position measured from wire i; Q_i is the size of the avalanche, the sum is extended to all wires contributing to the pad signal; and the weights are normalized such that $\Sigma\, w_i = 1$. Therefore the resolution is improved by a factor $A = \sqrt{(\Sigma w_i^2)}$.

For tracks at an angle $\alpha \neq 0$ there is, however, a worsening of the resolution owing to the fluctuations in ionization along the track. For instance, in Fig. 4.8.3, a large energy release on wire −2 will move the centroid towards positive x. This shift can be calculated from the measured pulse height of the wires and the position can be corrected accordingly.

d) Parametrization of the resolution

We will parametrize the resolution in the following way

$$\sigma^2(\alpha,\psi) = \sigma_0^2 + \sigma_a^2(\text{tg}\,\alpha - \text{tg}\,\psi)^2 + \sigma_F^2\,\text{tg}^2\,\alpha + \sigma_d^2 D\,,$$

$$\sigma_a = A\,K\sqrt{(L/12\,N)}\,.$$

The first term (σ_0) takes into account the electronic noise and any other effect independent of the angle and the magnetic field. The σ_a term is the parametrization of the angular and E × B effects. The σ_F term is the uncertainty on the angular correction arising from electronic noise on wire pulse-height measurement. The $\sigma_d$term is the contribution from the diffusion for a drift length D (m).

A test with a small TPC prototype has been performed [5] to study the angular effects. The chamber has been operated with an argon (90%) + methane (10%) mixture at atmospheric pressure, a magnetic field of 15 kG, a sense wire potential of 1.3 kV and a drift length of a few centimetres. The geometry of the proportional region and the operating condition were similar to those foreseen for the final TPC.

We have measured the Lorentz angle to be $\psi = 29° \pm 3°$, and σ_a to be $340 \pm 30\,\mu$m. We have also shown that angular corrections are feasible with an uncertainty $\sigma_F = 230\,\mu$m.

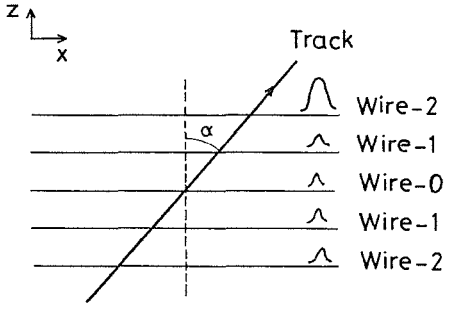

Fig. 4.8.3

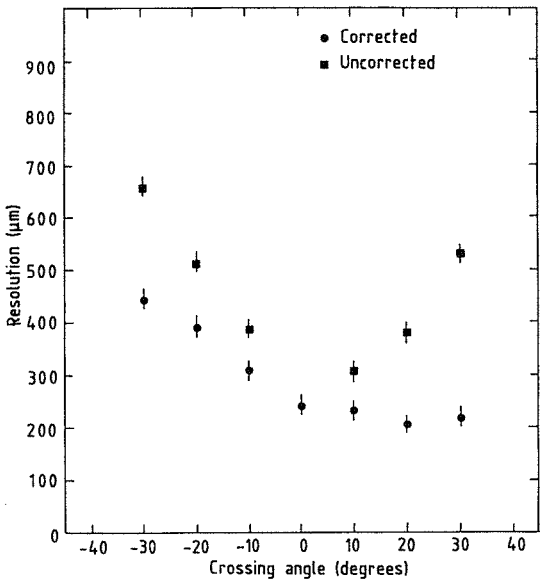

Fig. 4.8.4

The first two results are in a rather good agreement with the expected values [6]. The last one is higher than expected; the reason is probably that during the test the setting of the electronics of the wires was not optimized. It is foreseen to carry out further tests in order to investigate this effect.

Figure 4.8.4 shows our measurements of the resolution as a function of the angle; the dots refer to data with angular correction, the squares to uncorrected data. The contribution from noise is 155 μm and diffusion is negligible.

4.8.2 Momentum resolution

The momentum resolution $\Delta p_T/p_T^2$ can be calculated using the Gluckstern formula [7] assuming 21 equally spaced measurements inside the TPC.

Figure 4.8.5a shows the expected momentum resolution as function of the azimuthal angle without angular correction and assuming a blind region of ± 2.5 cm near the boundary of the sectors. Figure 4.8.5b shows the momentum resolution after angular correction.

We note that in both cases, when the vertex point is used in the fit, the dependence of the momentum resolution on the azimuthal angle is very small. A mean value for the momentum resolution is

$$\Delta p_T/p_T^2 \approx 1 \times 10^{-3}\,(\mathrm{GeV/c})^{-1}.$$

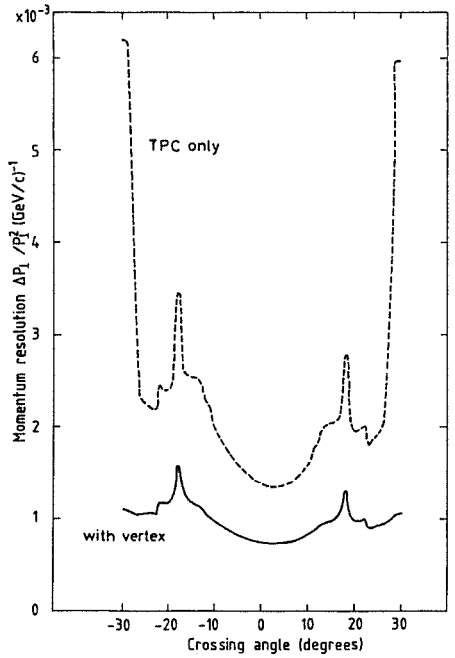

Fig. 4.8.5a

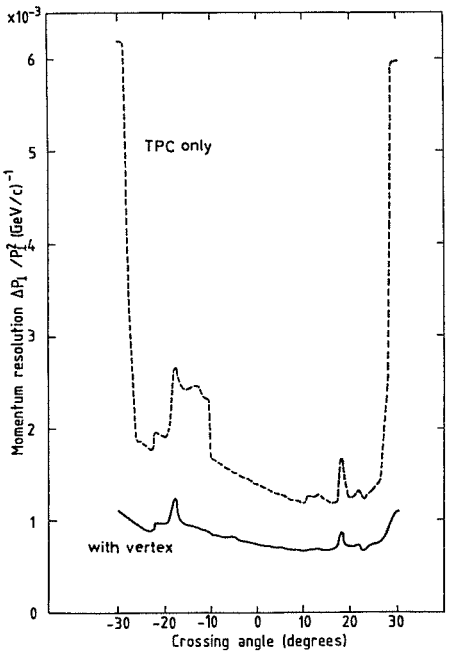

Fig. 4.8.5b

This corresponds to a statistical error on the sagitta measurement of about 150 μm.

It is very hard to estimate the systematic error on this measurement. The laser calibration system allows correction for field distortion, and the systematic error is the uncertainty on this correction. Since the correction is at the most 1 mm, we can assume a systematic error of 100 μm.

If we add quadratically a systematic error of 100 μm to the above, we arrive at a momentum resolution of

$$\Delta p_T/p_T^2 \approx 1.2 \times 10^{-3} (\text{Gev/c})^{-1}.$$

4.8.3 z and polar angle resolution

The z resolution is limited by the longitudinal diffusion and the error on the drift time due to the readout system.

The longitudinal diffusion is not reduced by the magnetic field and the precision attainable on the measurement of the centroid of the electron cloud is $\sigma = 720\,\mu$m for 1 m drift length.

The PEP-4 Group quotes [3] an average z resolution of 857 μm at 1.5 atm. For their conditions we estimate the average contribution of the diffusion to be $\approx 300\,\mu$m. It follows that in their case the readout system error is $\approx 800\,\mu$m.

If we assume that our readout system has the same performances, and using our contribution for the diffusion, we obtain a z resolution of about 1.1 mm.

Assuming an average of 300 z measurements we obtain a polar angle resolution of 0.1 mrad.

4.8.4 Two-track separation capability

Two space points of different tracks cannot be separated if, at the same radius, their $r\phi$ distance is less than a certain amount $\Delta r\phi$ and their z distance is less than Δz. The definition of double track separation capability depends on the definition of Δz and $\Delta r\phi$.

a) $r\phi$ separation

The pad response function in our geometry has a width of about 3.2 mm and our pad width is 6 mm. In this case, the induced signal on the pad row is always limited to two or three pads (see subsection 4.8.1). An optimistic value for $r\phi$ separation is two pad widths (12 mm), a pessimistic one is three pad widths (18 mm).

b) z separation

The physical limit on the z separation capability is the longitudinal diffusion, but this limit is never reached because of the stretching in time of the signals due to the integration time of the shaping amplifier. This long integration time is needed in order to have a good signal-to-noise ratio in pulse-height measurement, important for both dE/dx and $r\phi$ resolutions.

The shaping amplifier pulse width at the base is about 400 ns. With this figure we have an optimistic Δz of 20 mm and a pessimistic one of 30 mm.

c) Two-track separation

Since the quantities $\Delta r\phi$ and Δz are independent of radius, the two-track separation capability increases with the radius owing to the increasing mean distance between the tracks.

The two-track separation has been studied with a Monte Carlo program generating jet events at 80 GeV centre-of-mass energies. Figure 4.8.6 shows the percentage of unambiguous points as a function of the radius for both optimistic and pessimistic figures for $\Delta r\phi$ and Δz.

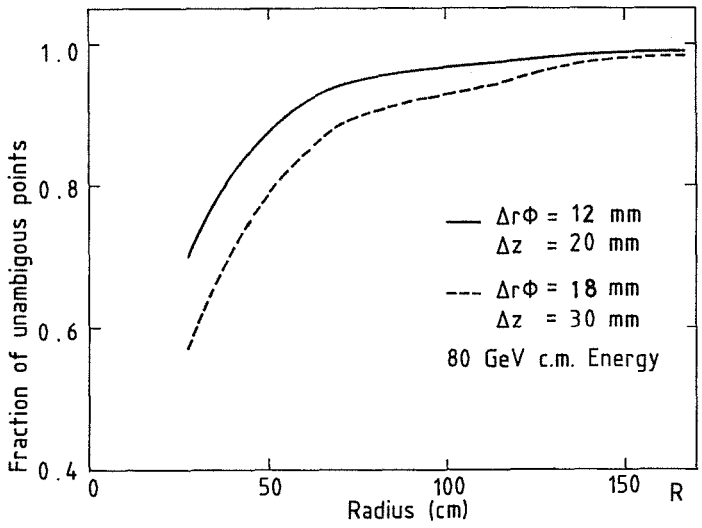

Fig. 4.8.6

4.8.5 Particle identification by dE/dx

The measurement of pulse heights on the TPC proportional wires from all sectors traversed by a charged particle can yield ~ 300 samples of primary ionization, each of projected length 4 mm, corresponding to the wire spacing.

With the proposed argon (90%) + methane (10%) gas mixture at 1 atm, such a measurement is expected to yield particle separations for e−π and π−K in units of ionization resolution (R) which are shown by the dashed curves in Fig. 4.8.7 plotted as a function of momentum (p). Here it is assumed that R varies with the number (n) of ionization samplings as $n^{-0.43}$ [8], and that the relativistic rise can be obtained from a parametrization [8,9] which includes a dependence on the sampling length.

However, it has been argued [9,10] that there may be saturation of R such that no improvement comes from increasing n, and also some experimental results [10] show that the relativistic rise appears to be independent of the sampling length. In this case, the particle separation would be degraded as shown by the solid lines in Fig. 4.8.7, so that dE/dx measurements would only be useful at the level of ≥ 3 st. dev. for e−π below 10 GeV/c.

These estimates take no account of the systematic errors in wire pulse-height calibration, or of angular effects.

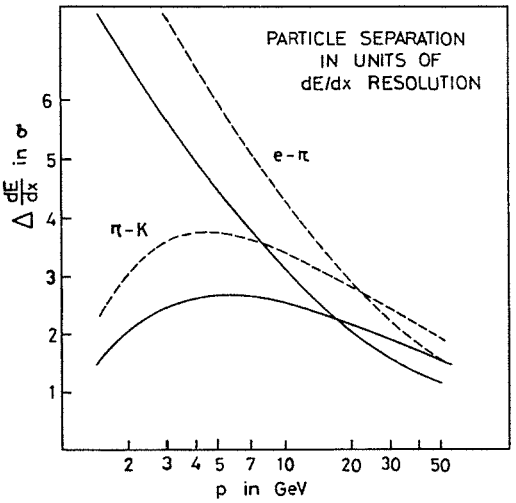

Fig. 4.8.7

[1] D.L. Fancher and A.C. Shaffer, Experimental study of the signals from a segmented cathode drift chamber, IEEE Trans. Nucl. Sci.**NS 26** (1) (1970) 150.

[2] S.R. Amendolia et al., Preliminary results on H4–TPC test, ALEPH Note No. 83 (1982)

[3] A. Barbaro-Galtieri, Tracking with PEP–4 TPC, TPC–LBL–82–24(1982).

[4] C.K. Hargrove et al., The position resolution of the time projection chamber at TRIUMF, TRI–PP–82–9 (1982).

[5] S.R. Amendolia et al., E × B and angular effects in the avalanche localization along the wire with cathode pad readout. To be published in Nucl. Instrum. Methods.

[6] F. Ragusa and L. Rolandi, E × B effect in ALEPH TPC, ALEPH Note No. 77 (1982).

[7] R.L. Gluckstern, Nucl. Instrum. Methods **24**, 381 (1963).

[8] A.H. Walenta et al., Nucl. Instrum. Methods **161**, 45 (1979).

[9] A.H. Walenta, Phys. Scripta **23**, 354 (1981).

[10] I. Lehraus, invited talk at the Vienna Wire Chamber Conf., 1983 [see also CERN/EF 83–3 (1983)].

4.9 TPC 90: construction and tests

The test chamber, TPC 90, is conceived as a prototype of one sector of the ALEPH TPC. The size of the end-plate is close to the size of one of the sectors in the ALEPH TPC. The TPC 90 will be installed in a magnet. Two systems of laser beams will be installed.

Besides the experience gained in this project, we foresee a series of special tests:

- The first goal is to detect the tracks produced by laser beams, to measure deviations from straightness, and to compare these with those expected on the basis of the measured magnetic field inhomogeneities.
- By creating nearby tracks, the two-track resolution in $r\phi$ and in z will be investigated.
- The effects of space charge due to background radiation will be investigated.
- By changing the axis of the field cage with respect to the direction of the magnetic field, it will be possible to study the influence of non-parallel fields.
- Following the studies with laser beams, we intend to perform tests also in particle beams.
- At a later stage we will study the effects of "gating" in the chamber.

The TPC 90 will also serve as a test facility for new electronics, new end-plates, and new ring electrode configurations for the drift field.

4.9.1 Construction of TPC 90

The field cage is an insulating fibre-glass cylinder, 80 cm in diameter and 160 cm long. In it are embedded 74 copper rings, 2 cm wide and 2 mm thick, spaced by 1.5 mm. On one end there is a fibre-glass plate covered with a layer of copper serving as the electrode. On the other end, the proportional chamber is mounted. The electric field is created by applying a high voltage to the plate and appropriate voltages to the copper rings. Several small quartz windows are mounted in the walls to accommodate the laser light.

The proportional chamber has the form of a hexagon. It consists of a fibre-glass plate covered with copper, and two planes of wires glued and soldered to frames, which in turn are glued to the plate. Eight rows of pads, each 8×8 mm^2 are milled in the copper plate. The pads are connected to the preamplifiers sitting outside through metallized holes. The sense wire diameter is 20 μm; all other wires are 75 μm. The distance between sense and field wires is 2 mm. The distances between the pad plane and the anode, and the anode and the upper electrode, are both 4 mm. Both anode and pad preamplifiers are connected via shapers to charge-coupled devices (CCDs), whose contents are digitized and read into a VAX/750 computer.

The detector will be installed inside a magnet producing either a constant field of 0.5 T or a field of 1.2 T in a pulsed mode of operation. The magnetic field will be measured. The inner diameter of the magnet is 90 cm and its length is 175 cm (Fig. 4.9.1).

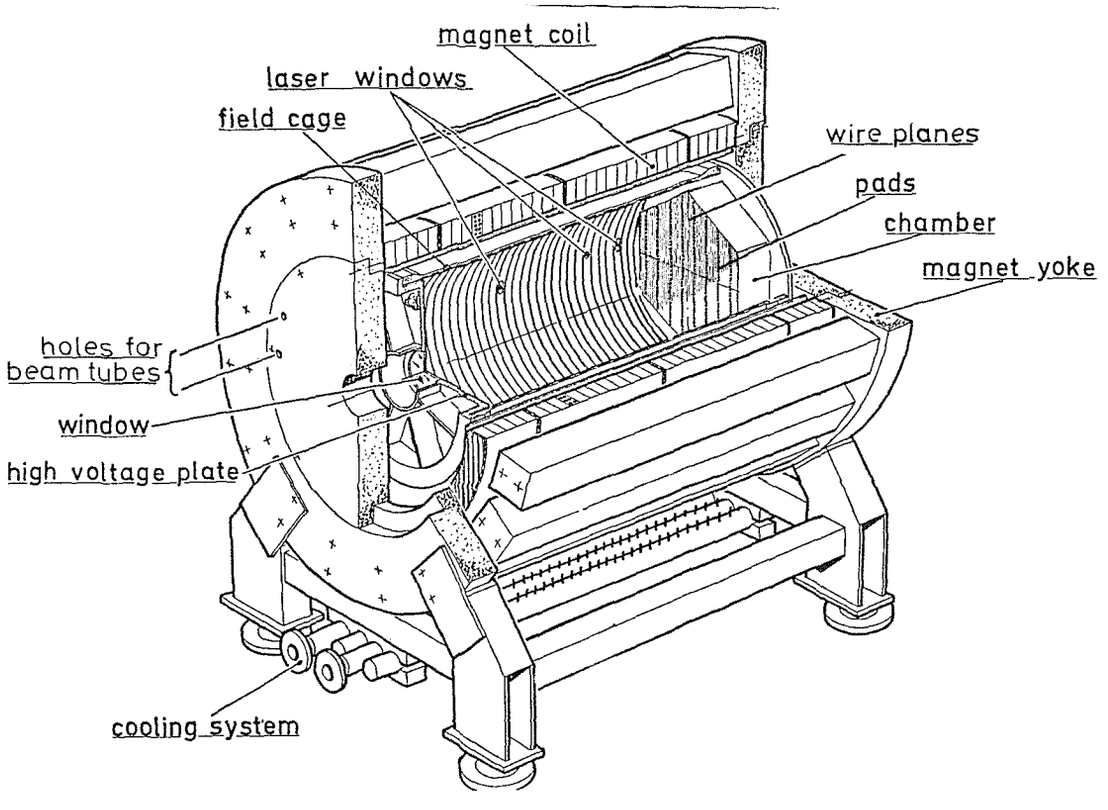

Fig. 4.9.1

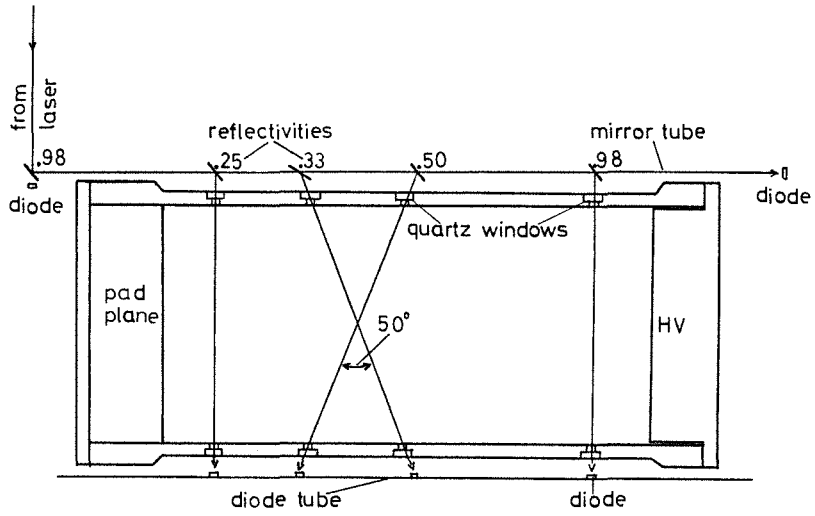

Fig. 4.9.2

Four laser tracks will be produced across the diameter of the TPC 90 volume by a system of mirrors mounted in a tube outside the field cage (Fig. 4.9.2). Alignment of the mirrors and slight adjustments in z will be performed in an alignment jig prior to installation in the TPC 90 system. Position-sensing photodiodes will monitor the laser beam along the mirror tube, and diodes again mounted in a tube outside the field cage will check the positions of all laser tracks after the chamber has been traversed. A small amount of the laser light will be directed onto a fast photodiode to provide a trigger signal for the TPC readout electronics. A lens system at the output of the laser will produce a beam of low divergence and approximately 3 mm diameter. Optical attenuators are envisaged to regulate the light intensity.

4.9.2 Preparation for tests

As mentioned above, the test program of the TPC 90 begins with the detection of straight tracks produced by laser beams. To do this, we need the following:

i) A knowledge of the magnetic field.

ii) Gain calibration. This will be done with a ^{55}Fe source for the wires. For the pads, calibration will be done by pulsing the field wires and will be checked by measurements with a source.

iii) Monitoring of the gas. Two systems are foreseen. In one, two weak radioactive sources are put inside the chamber at different axial positions (end-plate, HV electrode) and the pulse heights compared. In the second, the outgoing gas is checked in a monitor chamber.

iv) The pad response function. This will be measured by translating a laser beam across the pads. Adequate windows in the field cage have been foreseen.

v) Homogeneity of the drift velocity. This can be measured by using two parallel laser tracks.

4.10 Time schedule and cost estimate

4.10.1 Time schedule

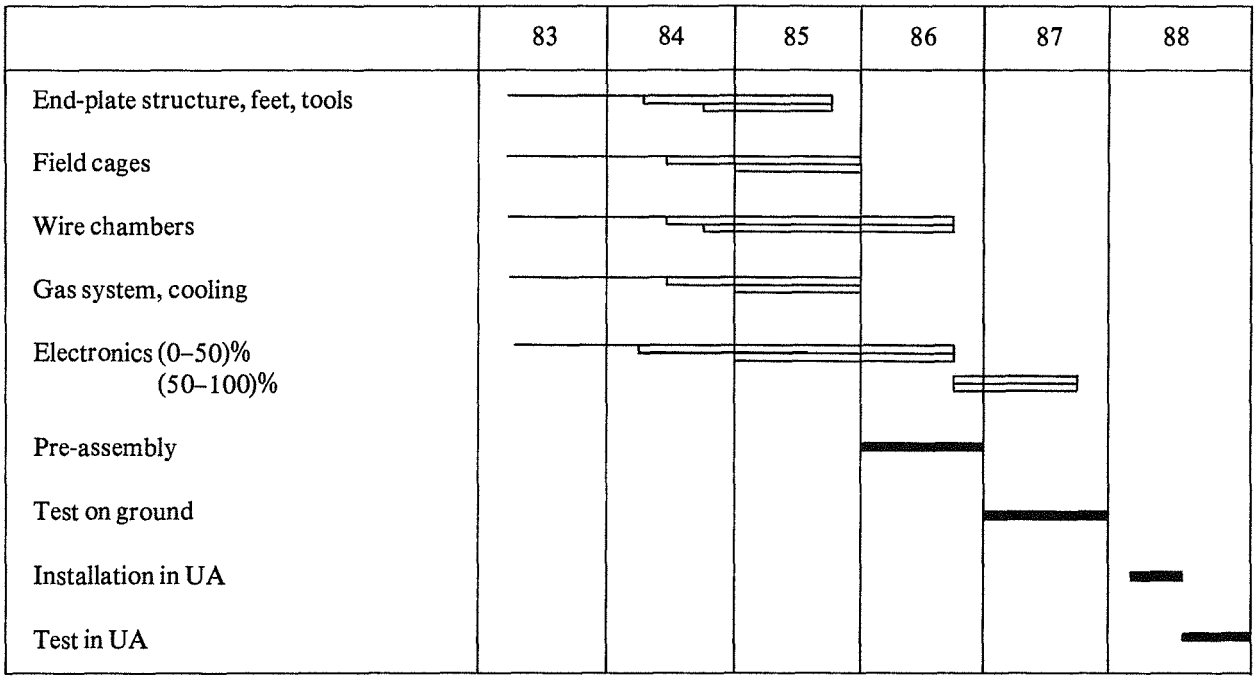

——— test, design, prototype work
▬▬ design completed (minor changes possible), prototype work, tendering
═══ production, production tests

4.10.2 Cost estimate

		MSF
Over-all structure including field cage		0.49
Wire chamber sectors		0.32
Electronics:	MSF	
Preamplifiers and cables	1.5	
Time projection digitizers (TPD), time projection processors (TPP), fan-outs	5.6	
Segment interconnects, crates, power supplies	1.4	
Calibration, test equipment, monitoring, prototypes, installation	0.7	
		9.20
Gas system		0.25
Triggering facilities		0.05
Laser calibration system		0.50
Tests, assembly, tools		0.56
	Total	11.4 MSF

5. THE ELECTROMAGNETIC CALORIMETER

5.1 Basic description and general layout

Various criteria can be used to choose between different designs for an electromagnetic calorimeter. We have decided to emphasize granularity. We believe that good transverse granularity (approximately the size of the electromagnetic shower) is the best possible solution for pattern recognition: it simplifies the identification of electrons inside hadronic jets, and facilitates the separation of photon energy from the background produced by interacting hadrons.

Our choice of an electromagnetic calorimeter is a lead/wire-chamber sandwich placed inside the solenoid. The structure of one layer of the calorimeter is shown in Fig. 5.1. The shower is developed in lead plates 2 mm thick. The secondary electrons from the shower create ionization in the gas. This ionization is amplified in an avalanche around a 25 μm tungsten wire placed at the centre of the extruded aluminium profile. The extrusion is closed along one side with mylar coated with a high-resistivity layer of graphite, permitting the transmission of induced signals. The resistivity of the graphite should be high enough for its presence to have only a negligible effect on the pulse shape of the pad during the integration time of the amplifiers (a few μs). Since the coupling capacity through the mylar is roughly 2 pF for an area of 3.2 mm $\times$ 3.2 mm, which corresponds roughly to the distribution of the induced charge, the leakage resistance (which is approximately equal to one half of the surface resistance of the coating R_0) should be much larger than a few MΩ per square. On the other hand, the resistivity of the graphite should be low enough so that the d.c. current created in the chambers by background particles does not appreciably change the operating voltage. An R_0 of 10^{10} Ω per square causes a voltage drop of well below 1 V. Hence, a value of R_0 between 10^8 and 10^{10} Ω per square is adequate.

The induced signal is read on cathode pads which are roughly 3 cm $\times$ 3 cm. The pads of each layer are connected together so as to form towers pointing to the vertex.

Three such summed signals are brought out for each microtower, corresponding to the sampling in the first 4 radiation lengths (X_0), in the next 8 X_0, and in the last 10 X_0. The exact final division is not yet decided and will result from the analysis of the prototype tests in order to optimize the resolution and the e/π rejection. In the last 10 X_0 we have decided, for reasons of economy, to use coarse sampling of the shower (4 mm lead thickness), thus decreasing the total number of layers to 43.

The detector is organized as a barrel section made of twelve modules, each 5 m long and 30° in azimuth, and two end-caps each made of twelve 30° modules. The general layout and the angular coverage is shown in Fig. 5.2a and b. As shown there, the signals from the microtowers are brought out by flat cables to the end of the detector where the electronics are placed. The total number of microtowers is 48 000 in the barrel and 24 000 in the end-caps, with a total of 216 000 electronic channels.

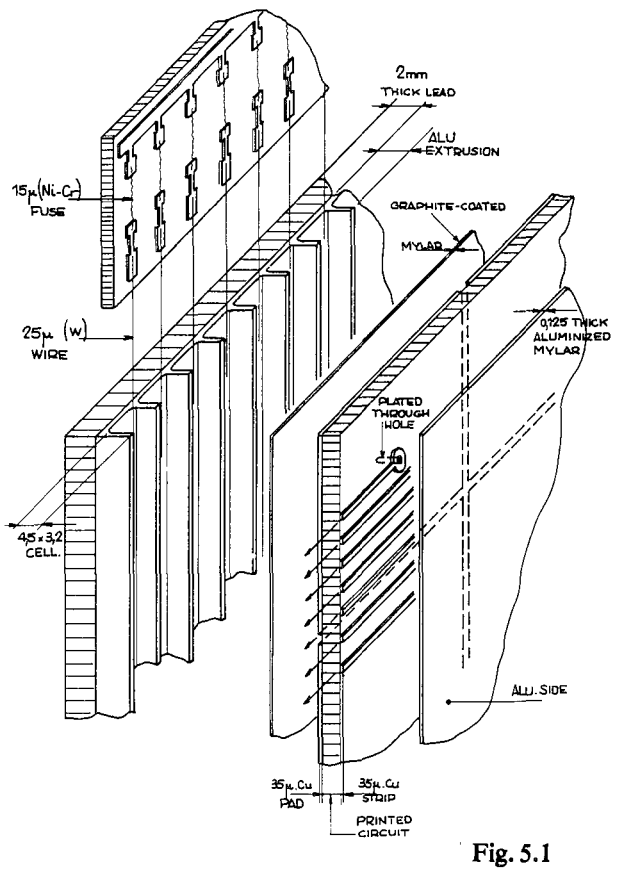

Fig. 5.1

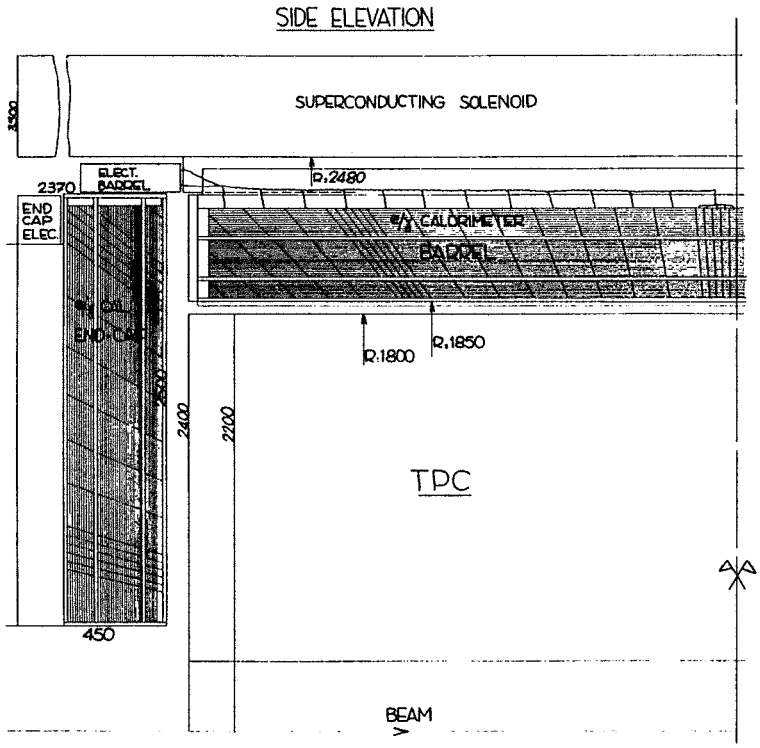

Fig. 5.2a

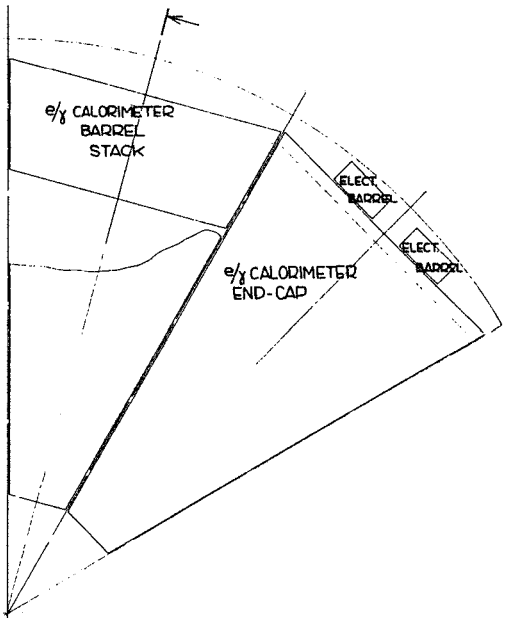

Fig. 5.2b

5.2 Performance

We have built a test calorimeter using the technique of aluminium extrusion, 25 μm tungsten anode wires, and a cathode readout. However since the cathode pads were large (17 cm × 17 cm), the lateral shower extension was not measured. This calorimeter has been exposed to electron beams of different momenta.

The wire chamber is operated in the high-gain proportional mode where there is some resolution improvement, probably due to saturation of large energy deposits from delta rays. However, there is a slight non-linearity as a function of incident electron energy. Results obtained with an argon + ethane (50/50) gas mixture are presented in Figs. 5.3 to 5.5.

The resolution obtained experimentally is

$$\sigma/E = 0.16/\sqrt{E\,(\mathrm{GeV})}$$

Note that the data shown in Fig. 5.3 exhibit a constant term of 0.015 in the energy resolution, to be added quadratically. This term was observed to vary in tests performed in other beams, and is at least partially due to beam resolution and bremsstrahlung.

The linearity, defined as signal (E-measured) divided by incident electron energy (E), is

$$\text{E-measured}/E = 1\text{–}0.05(E/40\ \mathrm{GeV}).$$

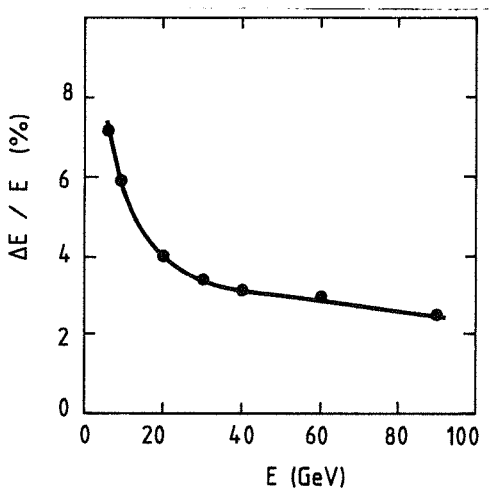

Fig. 5.3

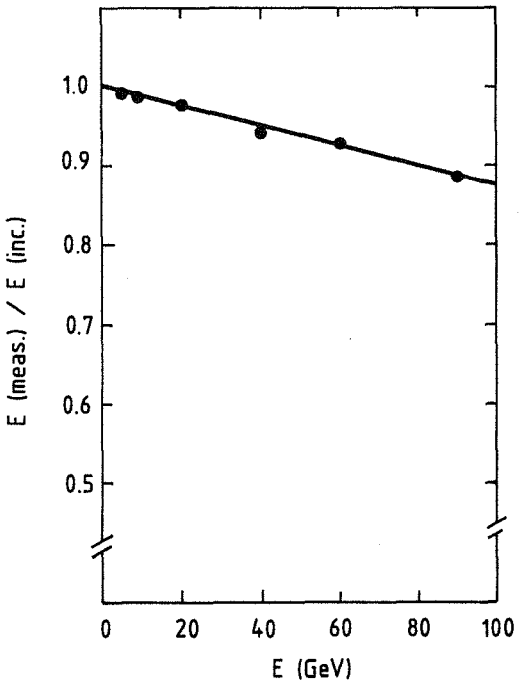

Fig. 5.4

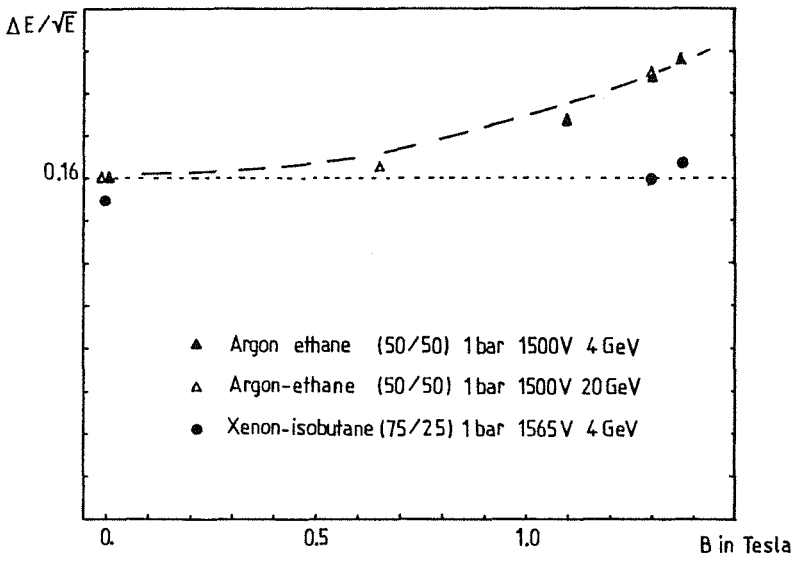

Fig. 5.5

In the same test we also measured the response of the detector as function of angle of incidence. The response was found to be constant to ±3% for ±45° variation. The resolution remained constant for all angles studied.

Measurements in a magnetic field showed that the resolution deteriorated when the field was aligned along the wire direction; in addition, a shift of the average value of about 4% at 1.3 T was observed. The resolution deterioration is most likely due to the magnetic trapping of low-energy electrons which spiral along the wire and deposit a large amount of ionization. We expected that by increasing the multiple scattering in the gas, one could decrease the path of these low-energy electrons. In a further test it was shown that by using an 80% xenon + 20% CO_2 or 75% xenon + 25% isobutane gas mixture, the influence of the magnetic field on the resolution was greatly reduced (see Fig. 5.5). These results show that our calorimeter will meet our performance aims when operating within the 1.5 T magnetic field of ALEPH.

The beam energy available in the tests of the Xe–CO_2 or Xe–isobutane mixture was too low for an accurate measurement of non-linearity. However, the results are compatible with the measurements with argon + ethane.

The expected performance of the detector with a xenon mixture is summarized in Table 5.1.

Table 5.1

Energy resolution:	Barrel	$0.16/\sqrt{E}$ (B field parallel)
	End-cap	$0.15/\sqrt{E}$ (B field transv.)
Linearity:		1.0–0.05(E/40 GeV)
Granularity:	Barrel	17 mrad x 17 mrad at 90°
$(\Delta\theta \times \sin\theta \cdot \Delta\phi)$		12 mrad x 12 mrad at 45°
	End-cap	9 mrad x 10 mrad at 40°
		10 mrad x 14 mrad at 27°

For isolated tracks, the calorimeter design is expected to give a π/e rejection factor of 1.2×10^{-3} at 24 GeV/c momentum.

For electron identification, the high spatial resolution of the calorimeter is important when comparing the track impact point with the position of the electromagnetic shower, to reduce $\pi + \gamma$ background as much as possible. Furthermore, owing to the very fine granularity, the electromagnetic energy — both the total energy and the first energy sample (first 4 X_0) — is obtained, less obscured by interacting hadrons and without pattern recognition problems.

5.3 Mechanical construction

The following design is used to evaluate the cost of the calorimeter. The final mechanical design will be decided after construction of various prototypes to be built and tested in 1983/1984.

5.3.1 The barrel

A section of the calorimeter stack is shown in Fig. 5.6. The barrel modules are mounted on rails which are fixed to the solenoid cryostat. The mechanical rigidity of the calorimeter is obtained by applying pressure (1 kg/cm^2) between a preformed fibre-glass front plate and a 6 cm rigid aluminium back plate. Owing to the friction coefficient of the various elements, measured to be larger than 0.2, the whole stack becomes a rigid body without need of gluing the various layers. Intermediate aluminium plates bolted to the end-plates prevent twisting deformations of the structure. Each module has a length of 4.8 m, a width varying between 0.98 m and 1.22 m, and weighs 11 tons.

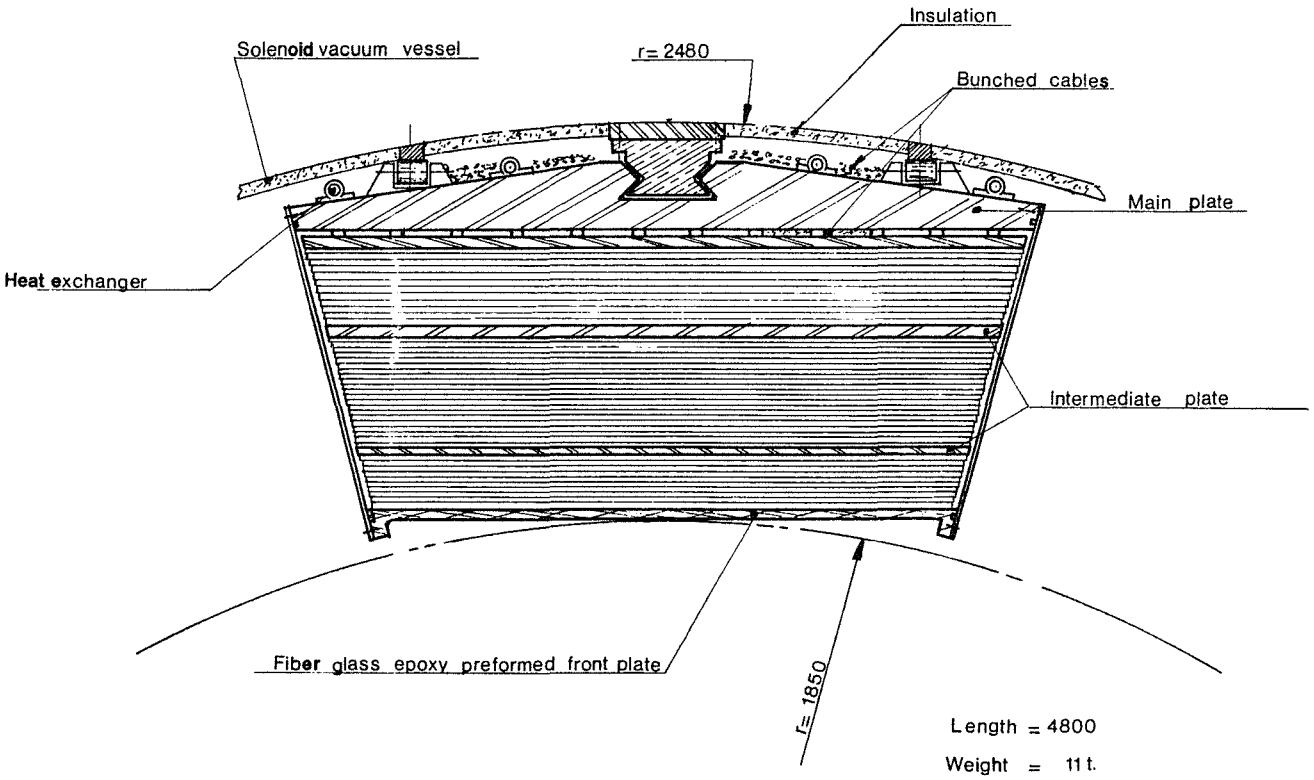

Fig. 5.6

In the present design the pad readout is obtained by double-faced printed circuit boards, where the pads are etched on one side, and the strip lines bringing the signal to the detector edge are etched on the other side. The electrical connection between pads and lines is made using metallized holes. A potentially cheaper version, where the cathode pads are obtained by cutting continuous copper sheets, is at present being studied and will be tested in one of our prototypes. The graphite layer on the mylar is obtained by spraying with a solution of graphite-loaded polyvinyl glue. The possibility of using commercially made graphite-loaded polythene is also being studied.

The wires are supported, roughly each 80 cm, by molded plastic supports which are press-fitted into the aluminium extrusion.

At the end of the module the wires are connected to high voltage (around 1500 V). A possible design for this HV layout is shown in Fig. 5.1. The wires are connected to high voltage via fuses of 15 μm NiCr wire. We have verified in tests that broken or shorted sense wires can be disconnected from the system by burning these fuses.

5.3.2 The end-cap

Each end-cap is constructed of 12 identical "petals", each weighing 3.2 t, as shown in Fig. 5.7. The mechanical construction of each petal is virtually identical to that of a barrel module, as described above and in particular the mechanical rigidity is obtained here also by applying pressure between a preformed fibre-glass front plate and a rigid aluminium back plate. The petals can then be attached to the front iron plate of the end-cap. The only significant difference in construction is that the wires and aluminium profiles can be parallel to only one of the sides and hence the wires differ in length across the surface.

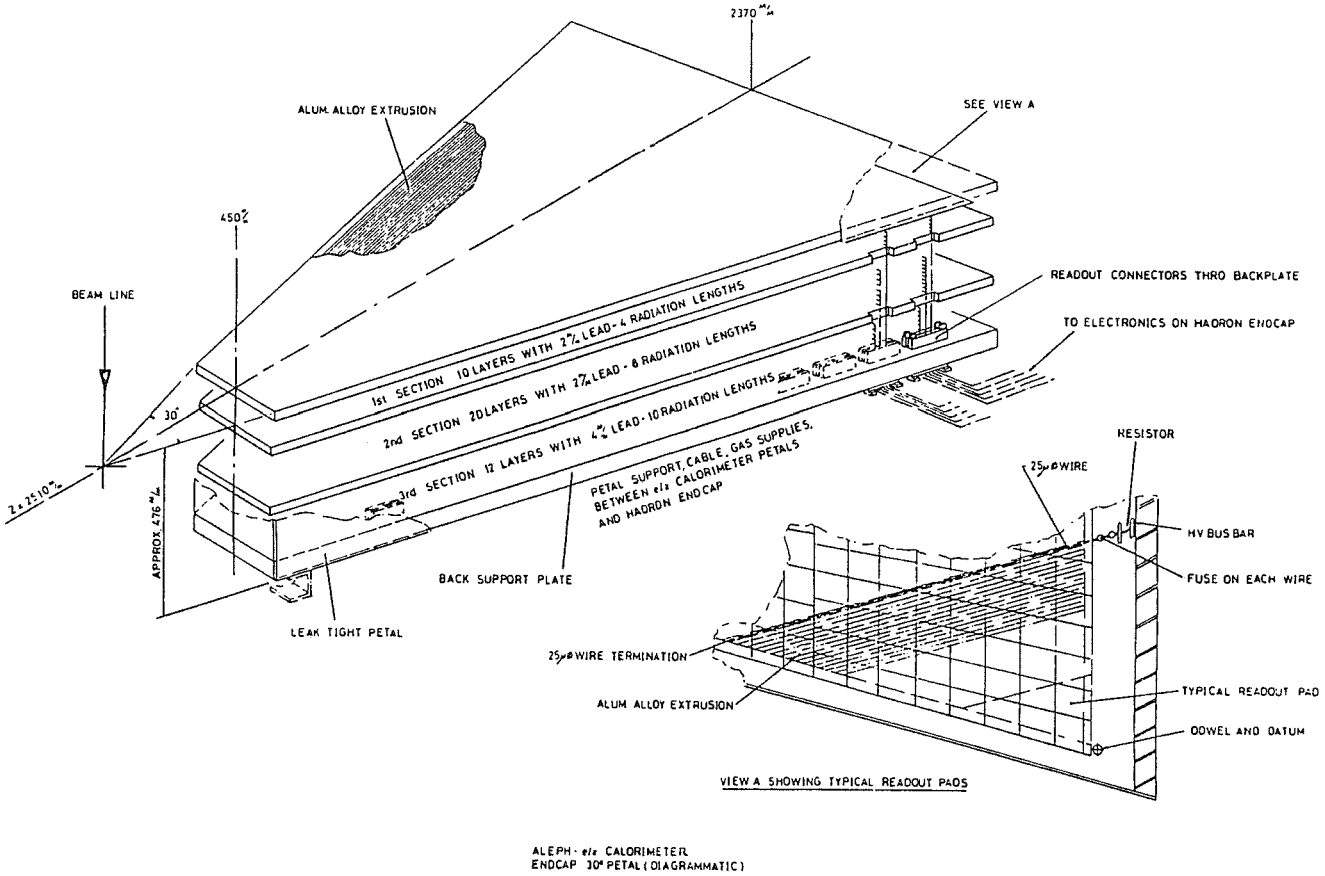

Fig. 5.7

5.4 The electronics

In order to obtain the excellent granularity of the detector, we need a large number of electronics channels. This can be realistically achieved by multiplexing the signals directly at the detector modules.

Since the signal level delivered by the detector is large ($\simeq$ 6 pC/GeV), we can use low-cost commercial integrating amplifiers and CMOS switches as the first stages of the detector.

The schematic diagram is given in Fig. 5.8. As can be seen in this diagram, there is a first-stage multiplexing by 32 on the detector and a further multiplexing by 8 later at the ADC cards. The ADCs have a dynamic range of 12 bits, and digitize within 3 μs by successive approximation. The dynamic range is extended using two readouts (Gain 1 and Gain 10) for each channel. This also reduces the problem of pick-up noise in the twisted-pair transmission.

The operation of the multiplexing integrating system can be understood by the following simplified description. One can consider three modes of operation (see Fig. 5.8):

i) a reset mode with all switches closed;
ii) a data storage mode with the A switches closed and B, C, D open; at the same time the summed output is transmitted to the trigger electronics;
iii) a readout mode; switches A are opened and the 32 B switches are closed in sequence, the C switch being used to reset the summing amplifier between each measurement.

Tests on bench models are continuing in order to select the best amplifiers, switches, and modes of operation. We hope to achieve an input noise of $\simeq$ 0.05 pC, corresponding to 8 MeV equivalent shower energy.

Discussions have started with manufacturers to integrate eight input-stage integrating amplifiers and switches in one hybrid circuit. The possibility of obtaining a monolithic circuit including 16 input stages is also being pursued.

5.5 Calibration

5.5.1 Electronics

The electronics chain is calibrated by injecting test charges on the summing amplifier. This tests the summing amplifier, the driver, the line receiver, the voltage multiplexer, and the ADC. Both hybrid and monolithic manufacturers

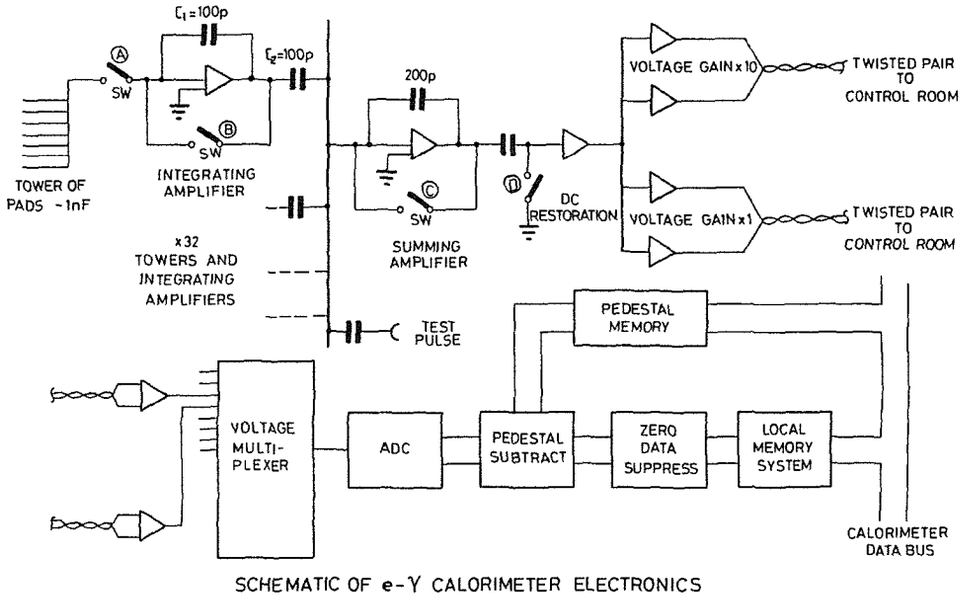

SCHEMATIC OF e-Y CALORIMETER ELECTRONICS

Fig. 5.8

assure us that the paired 100 pF capacitors C_1 and C_2 (Fig. 5.8) can be matched to better than 0.5%. Therefore after a reception test, we do not foresee the need to calibrate the input stage any further.

5.5.2 Missing wires or pads

For a fixed electronics gain and gas amplification, a missing wire (disconnected by a burnt fuse) or a missing pad (bad contact or defect on the printed circuit) would change the calibration. This state of the apparatus can be checked by pulsing the wire planes sequentially, thus injecting a known charge (6 pC/10 V) into the readout chain. Missing wires and pads are then easily detected and corrected for.

5.5.3 Over-all detector stability and uniformity

The voltage, pressure, and temperature dependence were measured to be V^{14}, P^7, T^7, respectively. There is no difficulty in keeping V constant to the required accuracy (< 1 V).

The detector modules are built in such a way that they can be pumped down, filled with the desired gas, and isolated; a closed-loop pump will slowly circulate the gas through the module. Such a fixed volume system will be insensitive to over-all temperature and atmospheric pressure variations. Gas amplification will be measured with small test chambers.

The uniformity of the detector response depends on variables such as temperature (which should be uniform within 0.5 °C) and mechanical tolerances. It should be noted that a high-energy shower is measured typically over $\simeq$ 100 different wires, thus smoothing random irregularities. Studies are being pursued to understand the various sources of non-uniformity in order to fix the permissible construction tolerances consistent with adequate uniformity.

We aim for a uniformity in energy response over the calorimeter of about 1%. This will be checked in a test beam. Should the device fail to achieve this uniformity, a map obtained by scanning the modules in a test beam will be used. The over-all calibration will be done with Bhabha events, as is usual at e^+e^- machines, using the above mapping to apply small corrections if necessary. Variations due to temperature, pressure, or voltage are monitored continuously with time.

5.6 Plans for prototypes

In 1983 we are planning the construction of three small prototypes of lateral size 25 cm × 25 cm, to be operated at CERN. Various components will be tested (different aluminium profiles, printed-circuit cathodes, wire support, fuse system, etc.).

We will also continue our study of the magnetic field effect and of various gases. In these new tests the cathode readout will be done using small pads, 3 cm × 3 cm, and therefore we will be able to test the lateral shower development and the shower centroid accuracy and their effect on the π/e rejection.

Finally, 256 channels of the multiplexed electronics will be available and will be tested together with these prototypes. Initially this will be done with a discrete component version, but at least one of the prototypes will be tested with a preliminary hybridized version of the integrating amplifiers.

5.7 Construction planning

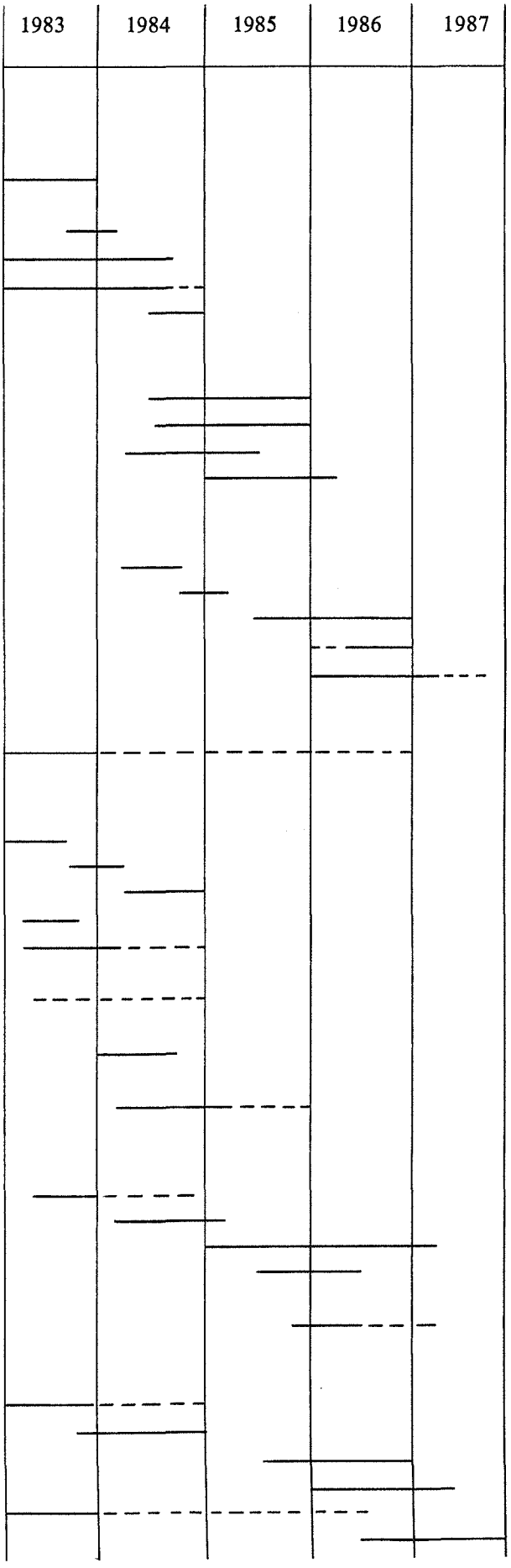

5.8 Cost and manpower

5.8.1 The barrel (cost in French francs)

	kFF
Aluminium extrusion	360
+tooling	20
Lead (93 tons)	545
Printed-circuit boards	5370
Mylar (graphite coated)	90
Aluminized mylar	120
12 back plates	526
Intermediate + front plates	376
Side panels	256
Wire supports	278
NiCr wire for fuses	55
Wire	174
Rail system	150
Assembly tools	1300
Miscellaneous connections	1200
TOTAL	10820 kFF

Manpower for construction: 35 man-years total.

5.8.2 The end-caps (cost in British pounds)

	k£
Lead	36
Wire	25
Extrusions	32
PCBs	350
Aluminium plates	95
Gas box and clamps	25
Mylar with adhesive	12
High resistive plastics	15
NiCr wire and fuse boards	10
Wire supports	20
Lifting gear	20
Assembly tools	60
Presses	20
Support structure	12
Gas, water, electrical connections	95
TOTAL	827 k£ + VAT

Manpower: 36 man-years total.

5.8.3 The electronics (220 000 channels — cost in French francs)

		kFF
Front-end hybrids 8 channels/hybrid	25 FF/channel	5500
Front-end cards + summing amplifiers + drivers + cables	15 FF/channel	3300
ADC cards + crates + crate controller	15 FF/channel	3300
TOTAL		12100 kF

5.8.4 Cost summary

		kFF
Barrel		10820
End-cap		8270
Electronics		12100
Gas system		250
Gas filling (xenon)		1000
VAX computer		1200
Installation tools + test beam		1000
Installation in zone		1100
Subtotal:		35740
Labour		
Barrel:	35 man-years	2000
End-cap:	36 man-years	0
Cost of hired manpower		
Barrel:		2000
End-cap:		0
GRAND TOTAL		37740 kFF
		(or 11.35 MSF)

6. HADRON CALORIMETER AND MUON DETECTOR

6.1 Introduction

The large iron structure which constitutes the main support of ALEPH and the return yoke for the magnetic field is fully instrumented in order to measure the flux of hadronic energy and to identify muons.

The iron barrel around the superconducting coil and the two end-caps are subdivided into 23 slabs. The outer one is 10 cm thick, all others are 5 cm thick, for a total of 120 cm of iron. The active part of the detector consists of planes of streamer tubes interleaved between subsequent slabs. The basic element is a plastic tube with an outer cross-section of 1×1 cm^2 and an active cross-section of 0.9×0.9 cm^2, as sketched in Fig. 6.1. A 100μm wire runs at 4 mm from the lower wall and is kept in place every half a metre by a plastic support. The gas mixture used is one part of argon, two parts of CO_2, and one part of n-pentane. The inner walls of the tube have a graphite coating, characterized by a resistivity from 0.1 mΩ to 1 MΩ per square, following the experience gained in the Mont Blanc experiment on proton decay.

Each tube layer in the hadron calorimeter is equipped with pad readouts on one side for integrated energy flux measurement, and with strips, parallel to each tube, on the other side, for digital reconstruction of the pattern of individual events. Each strip is 0.4 cm wide, with a pitch of 1 cm. This digital information, which is read also on two double layers positioned outside the magnet, is the basic tool for muon identification. Pads and strips are made from a PVC support, 1 mm thick, covered by aluminium foils 40μm thick.

The low price of raw materials, the easy assembly procedure, the simplicity of the automatic calibration system, and the fine-grained pattern information have been the decisive elements for the choice of this detector.

6.2 The hadron calorimeter

The geometrical shape of the iron structure defines the different arrangements of the tubes in the barrel and in the end-caps. In the barrel, 7 m long tubes are grouped in 24 modules of 23 layers. The first layer of each module contains 71 tubes and the last one 110 tubes. For mechanical reasons and for simplicity of gas flow, several tubes are grouped into larger boxes. The mixing of boxes with 7 tubes and with 8 tubes allows the intermediate layers to be filled completely, with an accuracy always better than one cm, as shown in Fig. 6.2. Each module contains 2324 tubes for a total of 55 776 tubes in the barrel.

In the end-caps, tubes of decreasing length are arranged into the sextants of the iron structure as shown in Fig. 6.3. The 2 cm spacers which couple successive iron sheets every 92 cm define the lateral dimension of the boxes. A total of 82 200 tubes, ranging from 0.5 m to 3.85 m in length, constitute the active volume of the end-caps.

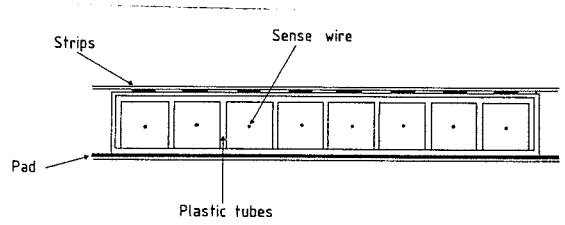

Fig. 6.1

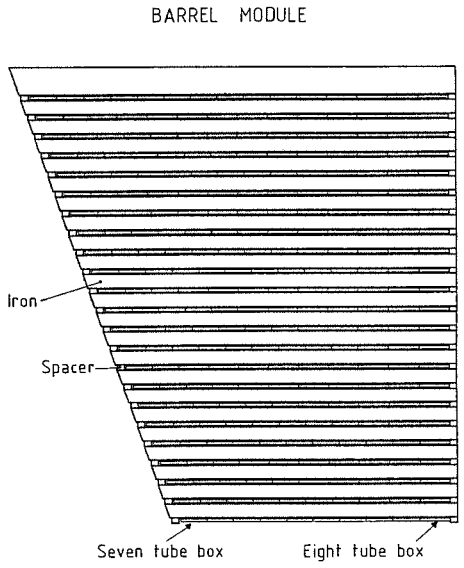

Fig. 6.2

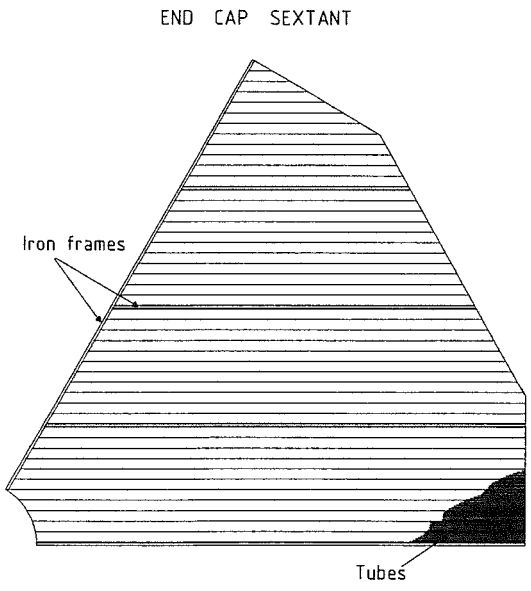

Fig. 6.3

In several regions the geometry of the magnet forbids the installation of tubes. The main dead regions are the following:

1) Along the sides of the barrel modules, iron bars, 2 cm wide, connect successive slabs. This dead space amounts to ~ 5 cm every 15°, equivalent to 5% of the average barrel surface.
2) In the end-caps, the spacers described above, together with the external frames surrounding the sextants (2.5 cm thick), cause a fraction of 6% of the end-cap surface to be insensitive.
3) At the end of the barrel modules, notches are cut to permit the passage of the cables from the inner detectors. The insensitive area is 14 cm wide, over the whole azimuthal angle. Two-thirds of this surface is covered with iron, but not with tubes, one-third is filled with cables. In two positions, at the top and bottom of the apparatus, these holes are enlarged to allow free space for the pipes of the cryostat. The presence of these insensitive regions causes local degradation of the energy resolution of the calorimeter but does not entail a loss of angular coverage.

The pulse height is read from pads connected in a projective geometry. The lateral width of hadronic showers (about 30 cm) and the geometry of the iron structure suggest that each barrel module be subdivided into 40 towers. A single tower covers the angular ranges $\Delta\phi = 7.5°$ and $\Delta\theta \simeq 5°$, as shown in Fig. 6.4. A total of 768 towers are fully contained in the barrel itself ($\theta > 50°$), whilst 96 towers on each side of the barrel continue smoothly into similar towers, with crossed geometry, in the external part of the end-caps ($40° < \theta < 50°$). These define, therefore, also the tower dimensions in the end-caps, except for the innermost four rings, where the angular granularity becomes larger to avoid towers of too small dimensions ($\Delta\phi = 15°$ for $15° < \theta < 30°$, and $\Delta\phi = 30°$ for $6° < \theta < 15°$). A description of the pad arrangement in the end-caps is given in Fig. 6.5. Pads which are interrupted by the reinforcement spacers are reconstructed at the electronic level, by summing the signals of the two parts.

A total of 384 towers are fully contained in the end-caps, in addition to the 192 shared with the barrel.

Cables from all pads of the barrel run along the tube layers, towards the notches cut at the ends of the modules, reaching the front-end electronics installed on the outer parts of the magnet. In a similar way, pad cables in the end-caps are collected on the external sides of the sextants.

In addition, the firing of individual tubes is recorded by means of strips running parallel to the tubes themselves. Electronic boards containing preamplifiers and serial readout logic are installed at one end of the strips. In the barrel, they are located between the iron plates on the sides of the notches used to get cables of inner detectors out, and are easily accessible when the end-caps are displaced, as sketched in Fig. 6.6. In the end-caps they are always accessible along the outer sides of the sextants.

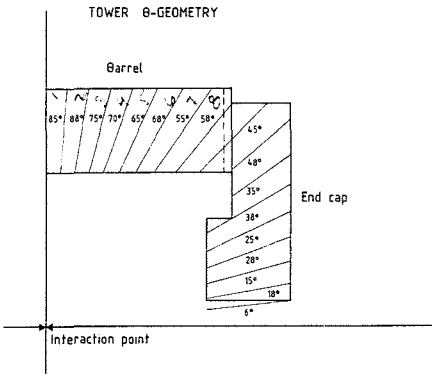

Fig. 6.4

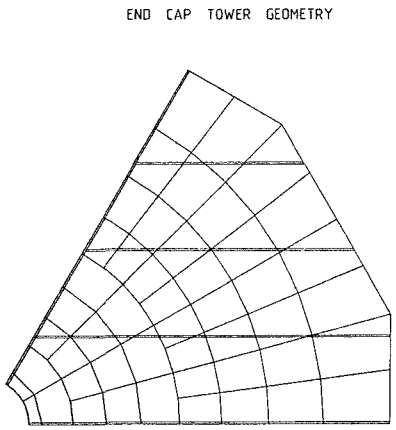

Fig. 6.5

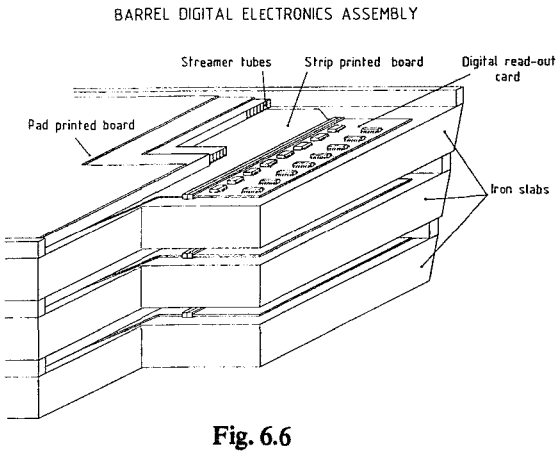

Fig. 6.6

6.3 The muon detector

The digital information on individual strips in the hadron calorimeter is already an essential part of the muon detector. In addition to it, external to the magnet, both in the barrel and in the end-caps, two double layers of streamer tubes are installed to identify tracks crossing the full iron and to measure their angle. The readout strips are arranged in two projections each with an effective pitch of 5 mm (see Fig. 6.7). In the barrel, the projections are orthogonal, in the end-caps the strips cross at 60°. Since layers backing the barrel and the end-caps reproduce the structure of the hadron calorimeter, additional tubes are needed to cover the gaps left open in the boundary regions. This solution has been chosen, in contrast to lengthening the barrel tubes, to leave the space facing the barrel notches free for all outgoing cables (see Fig. 6.8).

The first double layer is placed just behind the last iron slab, whilst the second is placed 50 cm further away in order to measure the angle of outgoing particles.

The double layers around the barrel are structured in 12 parts, corresponding to the dodecagonal shape of the magnet. A possible solution for supporting these tubes is shown in Fig. 6.9. The iron joint between two barrel modules extends radially for ~ 15 cm and terminates with two wings. Honeycomb aluminium slabs are attached to these wings: the lower one acts as a support for the tubes of the first double layer, the upper one acts as a solid support for all cables of the apparatus on their way towards the barracks. The distance between two adjacent tube layers is 1.5 cm, corresponding to 0.5% of the full coverage of the barrel. Columns 50 cm high and 50 cm apart support a second, lighter, honeycomb slab which holds the second double layer of tubes. This second part of the detector cannot follow the regular shape of the magnet, since cables leave the detector at three levels towards the barracks, as sketched in Fig. 6.10. This means that three sides of the dodecagon are positioned at a longer distance (typically 1 m) and are enlarged to avoid dead areas.

A total of 18 720 and 19 928 tubes constitute the first and the second double layer. The corresponding readout channels are 43 968 and 45 176, respectively.

The number of tubes and readout channels in the various parts of the detector are summarized in Table 6.1.

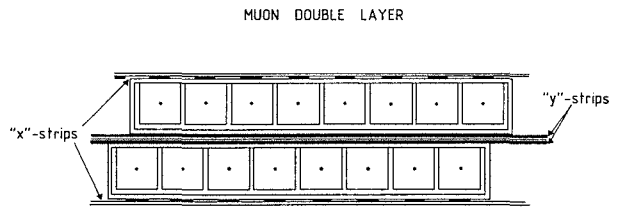

Fig. 6.7

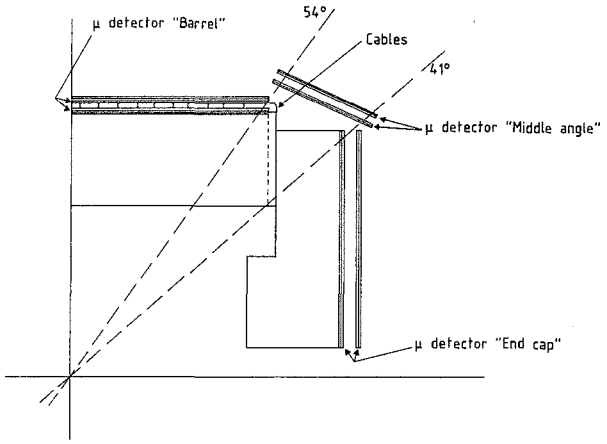

Fig. 6.8

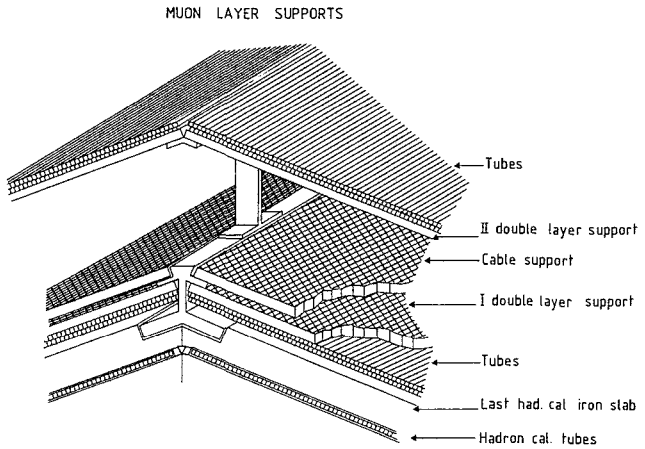

Fig. 6.9

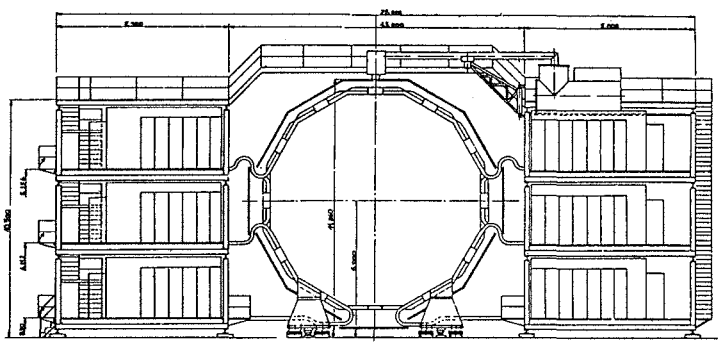

Fig. 6.10

Table 6.1

Item	Tubes	Towers	Digital readout
Hadron calorimeter			
Barrel	55776	768 + 192	55776
End-caps	82200	384 + 192	82200
Total	137976	1152 + 192	137976
μ detector			
Barrel			
inner layer	5952		22752
outer layer	6600		23400
End-caps			
inner layer	8448		16896
outer layer	8448		16896
Middle angle			
inner layer	4320		4320
outer layer	4880		4880
Total	38648		89144
Over-all total	176624	1344	227120

6.4 Gas mixture and monitoring system

6.4.1 Gas mixture

The gas used in the apparatus is a mixture of one part of argon, two parts of CO_2, and one part of n-pentane. This mixture, the one used for the Mont Blanc experiment, is preferred for safety reasons, the total amount of hydrocarbons being only 60 kg. Independent gas lines will be connected to each plane of the detector.

6.4.2 Monitoring system

The main factors affecting the stability of the detector response are the power supply variations and the gas mixture fluctuations. Power supply fluctuations have an effect according to $\Delta Q/Q \simeq 7\,\Delta V/V$. Since power supplies are easily controlled to 1%, this is not a problem.

Gas mixture fluctuations are a more serious problem. The main parameters to control are the pressure and the gas composition. A lower pressure and/or a lower quenching tend to lower the plateau and vice versa, leading to variations in the collected charge.

An easy way to monitor and control this effect is to put a monitoring streamer tube in series with the gas-flow pipe to the apparatus, with a collimated β source on it. A pulse-height analysis of the signal coming from the tube with a dedicated processor can drive gas control equipment to re-adjust the gas composition. With a rate of 100 Hz from the source, a sampling rate of 100 s will lead to a 1% accuracy in the measurement.

Moreover, a continuous and independent check is provided by the comparison of the digital and analog responses of the apparatus, because the hit multiplicity from the digital readout does not change for small gain fluctuations.

6.5 Front-end electronics

The basic information from the hadron calorimeter and from the muon detector consists of the analog signals of the 1344 towers and the digital signals of the 227 120 strips.

A single streamer induces a pulse of about 2 mV on a 50 × 50 cm^2 pad, with a rise-time of ~ 20 ns and a time jitter of $\sigma = 50$ ns, corresponding to the drift-time inside the tube. Pulses from all pads of a tower are linearly added through an operational amplifier and processed in three different ways:

i) pulses are discriminated in order to provide a fast minimum ionizing trigger signal;
ii) signals from about 20 towers are added and analysed by flash ADCs for energy triggering;
iii) signals are fed to sample-and-hold circuits for multiplexed ADC analysis.

Pulses induced on strips, about 5 mV high on 50 Ω impedance, are immediately amplified, shaped by one-shot circuits, and stored in shift registers. All these electronic elements are on boards placed at the end of the strips. The small power consumption of the cards, about 10 W per barrel module, ensures that the gas gain will not be affected by any heat flow. All channels contained in a plane of a double module (71 × 2 to 110 × 2 strips) are then serially read out by a processor, mounted externally to the detector, which codes the information of the whole module, transferring only the addresses of the hit strips. Cluster data are transferred in a single word containing the cluster centre and width. The mean number of clusters per track has been measured to be of the order of 30 for a 10 GeV track. With a mean multiplicity of 20 tracks per event, we can assume an upper limit for the number of transferred words of ~ 600. Adding the analog information from towers and control words, a safe estimate of ~ 800 words per event can be made.

6.6 Performances of the hadron calorimeter

6.6.1 Hadron energy measurement

A prototype of the hadron calorimeter has been tested at the SPS. The dimensions of this test module, corresponding roughly to a single tower of the final detector, consisted of 27 tube layers with pads of 60 × 60 cm^2, interleaved with iron slabs 4 cm thick. Tubes were also coupled to strips to record the digital pattern of the hadronic shower.

Part of the data have been taken with an e.m. calorimeter in front, similar in thickness to the ALEPH e-γ detector.

Figure 6.11 shows the pulse-height distributions for muons and pions at 20 GeV, whilst Figs. 6.12 and 6.13 show the average and the standard deviation of the pulse-height distributions as a function of energy. The response of the calorimeter is linear up to 50 GeV and shows a deviation of less than 10% (possibly due to rate effects) at 100 GeV. In the same way, the quantity $\sigma/\sqrt{E}$ is constant and equal to 0.78 up to 50 GeV, and increases at higher energies.

These performances approach, within 15%, those of a scintillator-iron sandwich of the same sampling.

6.6.2 Trigger on hadrons and muons

The time response of the hadron calorimeter is very fast and can be easily used to trigger on hadrons and muons. The time jitter of the tower signals is 5 ns for hadrons (containing several tens of streamers) and 17 ns for muons (≤ 26 streamers). Figure 6.14 shows on an enlarged scale the pulse-height distribution for muons, together with the pedestal peak which provides a direct measurement of the noise of the system. Setting the threshold of the discriminators at 1/3 of a minimum ionizing particle ensures full efficiency for detection of muons crossing a whole tower, and guarantees an efficiency of greater than 99% for muons equally shared between two nearby towers. The probability of a minimum ionizing trigger from random noise is negligible if one asks for a coincidence of two towers.

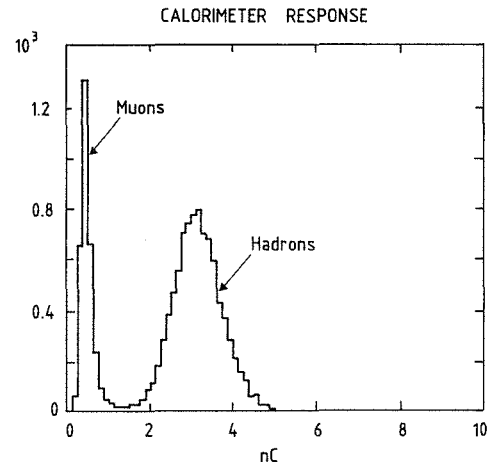

Fig. 6.11

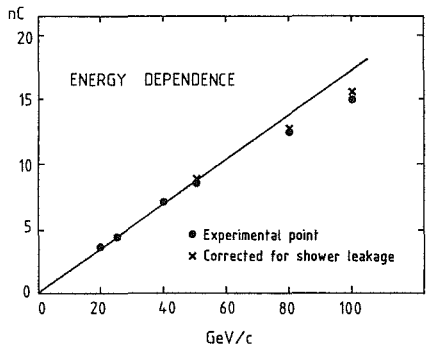

Fig. 6.12

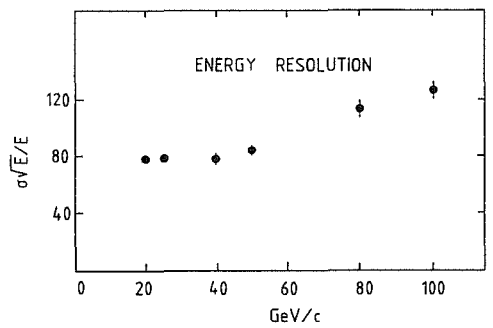

Fig. 6.13

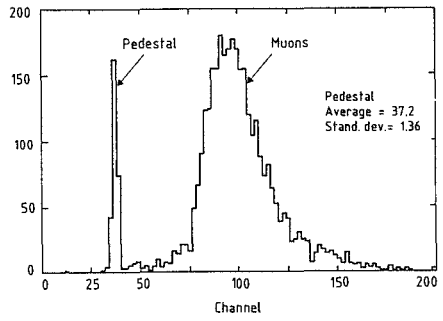

Fig. 6.14

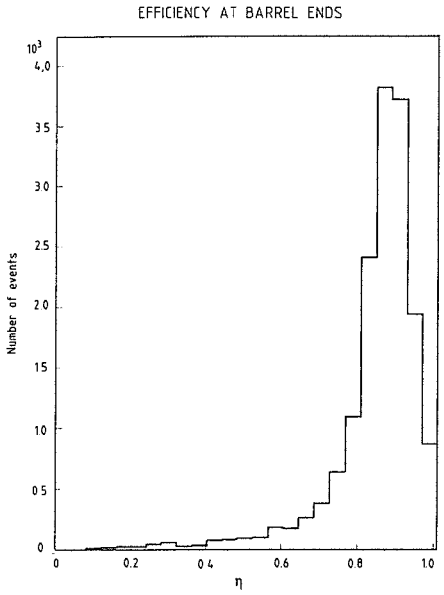

Fig. 6.15

The loss of efficiency for triggering on muons due to the dead regions of the detector has been evaluated with a Monte Carlo calculation. Muons have been produced with the momentum spectrum expected for the decay of heavy quarks and traced through the central detector and the magnetized iron. With the chosen threshold of 1/3 of a minimum ionizing particle we get an over-all efficiency of 97%. Analogous results are obtained for the end-caps.

The notches cut at the end of the barrel modules do not introduce any appreciable loss, owing to the large θ angle at which particles cross the insensitive volume ($40° < \theta < 50°$). The ratio n of the number of hit planes to the number of crossed planes is shown in Fig. 6.15.

6.7 Muon identification

The whole detector acts as a good tracking device through the magnet yoke and behind it. The hadron calorimeter has a very good granularity in the $r\phi$ plane, allowing the identification of straight-through tracks even in towers which already contain a hadronic shower. This is shown in Fig. 6.16, where a muon and a hadron cross the test module simultaneously. Several algorithms are under study to make full use of this information, by identifying the individual particles entering the calorimeter, their local energy releases, and the continuity of their trajectories throughout the iron.

The external chambers (each one consisting of a double layer of tubes) provide two points in θ, ϕ, half a metre apart. Each point is measured with a space resolution $\sigma < 2$ mm in both coordinates. The staggering of the two planes of tubes guarantees the full efficiency of each chamber even if one plane is crossed in the plastic wall separating two tubes.

A complete Monte Carlo simulation of the hadron–muon detector is under preparation, and its predictions will be compared with the results provided by the test of a realistic prototype. This is at present under construction and will

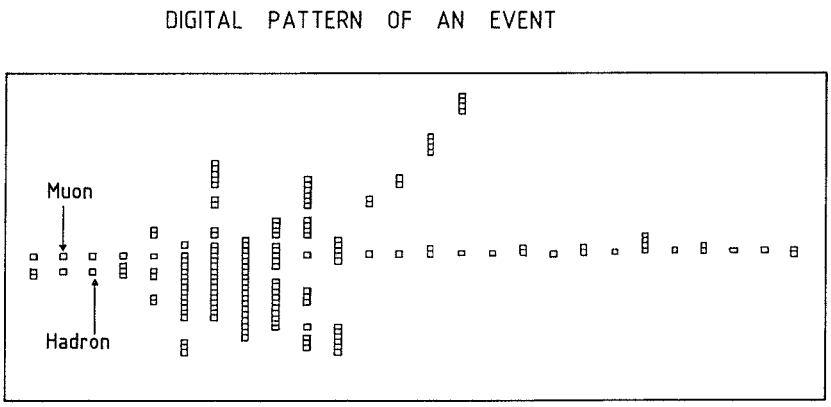

Fig. 6.16

come into operation in the summer of 1983. The expected performances for hadron rejection have been evaluated in two different configurations:

i) the identification of the track in the second half of the hadron calorimeter in the $r\phi$ projection and a point in the first external chambers allow a rejection against punch-through of better than 2.5×10^{-3} at 10 GeV/c and 5×10^{-3} at 30 GeV/c;
ii) the additional use of the second double layer provides the angle of the outgoing particles with an error of 5.6 mrad in projection.

Together with this information, the punch-through rejection becomes 2×10^{-3} independent of energy. These figures can be considered as upper limits to the contamination since they do not make full use of the information of the calorimetric towers and of the $r\phi$ pattern of the event. However this level of contamination is already very close to that expected for π, K decay which ranges from 8×10^{-3} to 2×10^{-3} for 2 to 10 GeV/c.

6.8 Construction and time schedule

The laboratories involved in the construction of the hadron calorimeter and of the external muon layers are Bari, Frascati, Pisa, and Beijing. Part of the machines needed for coating and cutting the tubes, and for preparing the strips and the pads, already exist in Frascati and will be completed in 1983. The preparation of the 7- or 8-fold tubes will be done for the whole detector in this laboratory, as well as the full wiring and testing of the barrel tubes.

The end-cap tubes are different in length and require an *ad hoc* assembly, more similar to that of normal chambers because of the width (92 cm) of each module. Wiring and testing of these tubes will be shared between Bari and Pisa. Table 6.2 summarizes the share of responsibilities.

Discussions are under way with collaborators of the Institute of High-Energy Physics, Beijing, to explore the possibility that the second muon double layer and the tubes covering the angular range $40° < \theta < 50°$ be built in Beijing.

The production of tubes will start during 1984 and will be completed in 1985. Barrel layers, completed with pads and strips, can be ready for installation at the beginning of 1986. End-cap layers will be available six months later.

Priority will be given to hardware construction to meet the time schedule of the magnet assembly. This will delay the construction of the electronics for financial reasons. However, we expect to order the electronics in 1985 for installation in 1987.

Table 6.2

Item	Laboratory	Person responsible
Tube preparation	Frascati	P. Picchi
Barrel layers	Frascati	P. Picchi
First end-cap	Bari	G. Maggi
Second end-cap	Pisa	C. Bradaschia

6.9 Cost estimate and staging

The basic elements for evaluating the over-all price of the detector are:

1) the barrel tubes, 7 m long, cost 8 SF each;
2) the end-cap tubes, owing to the shorter lengths, cost 7 SF each on the average;
3) the pad and strip printed boards cost 25 SF/m^2;
4) the complete readout chain of one tower, including pulse-height analysis, discriminator, and trigger electronics, is 200 SF;
5) a digital channel for strip readout costs 10 SF.

These unitary prices, times the number of elements corresponding to each item, give the over-all costs summarized in Table 6.3.

In addition, cabling, power supply, gas system, computer, special tooling, transport to CERN, and so on, are also given in Table 6.3.

Since the total cost of 7 MSF exceeds the over-all expenditure of 5 MSF recommended by the Collaboration for the hadron and muon detectors, the installation will not be complete at the beginning of the experiment.

The parts of the detector which will be ready at the machine start-up will be:

i) all the mechanical parts of the hadron calorimeter (tubes, printed boards, and so on);
ii) the readout electronics of the hadron calorimeter towers;
iii) all the mechanical and electronic elements of the first muon double layer.

The instrumentation of the individual tube readouts of the calorimeter, as well as the second muon double layer will be constructed later, depending on the budget for the following years.

Table 6.3

	Cost without manpower and taxes (kSF 1983)		Manpower man-years
Hadron calorimeter			
Mechanics (137976 wires, 1344 towers)	1400		20
Electronics			
a) analog tower readout (1344)	270		
b) digital wire readout (137976)	1400		
Cables, racks, connectors	350		2
Gas system	200		1
Computer (VAX 11/730)	100		
Monitoring, calibration high + low power supply	285		
Prototype, tests	170		2
Tooling	230		4
Transport to CERN	50		
Assembly	100	(+300 manpower)	5
Total hadron calorimeter	4855		34
μ detector			
Mechanics (38648 wires, 89144 strips)	450		13
Electronics digital readout (89144)	900		
Cables, racks, connectors	230		1.5
Gas system	85		0.5
Monitoring, calibration, high + low power supply	140		
Prototype and tests	80		1.5
Transport to CERN	25		
Assembly	50	(+100 manpower)	3.5
Total μ detector	2060		20
Over-all total	6915		54

7. THE INNER CHAMBER

The Inner Chamber (IC) has two functions. One is to provide an essential part of the Level 1 trigger, the second is to enhance the over-all charged particle tracking of ALEPH particularly in the critical area close to the beam pipe. The design, which is described in detail, has lightweight shells carrying cathode strips to measure the z-coordinate. An alternative design, which would obtain the z-coordinate by an analogue method, is also being investigated; it is briefly described.

7.1 Dimensions

The position of the IC relative to adjacent parts of the detector is shown in Fig. 7.1. The chamber is a fairly conventional, small cell, drift chamber; it has eight layers of sense wires each with 128 cells. These are separated into four sub-chambers, using polystyrene shells which support hooped cathode strips on the inner and outer walls to provide the z readout. The important dimensions are given in Table 7.1.

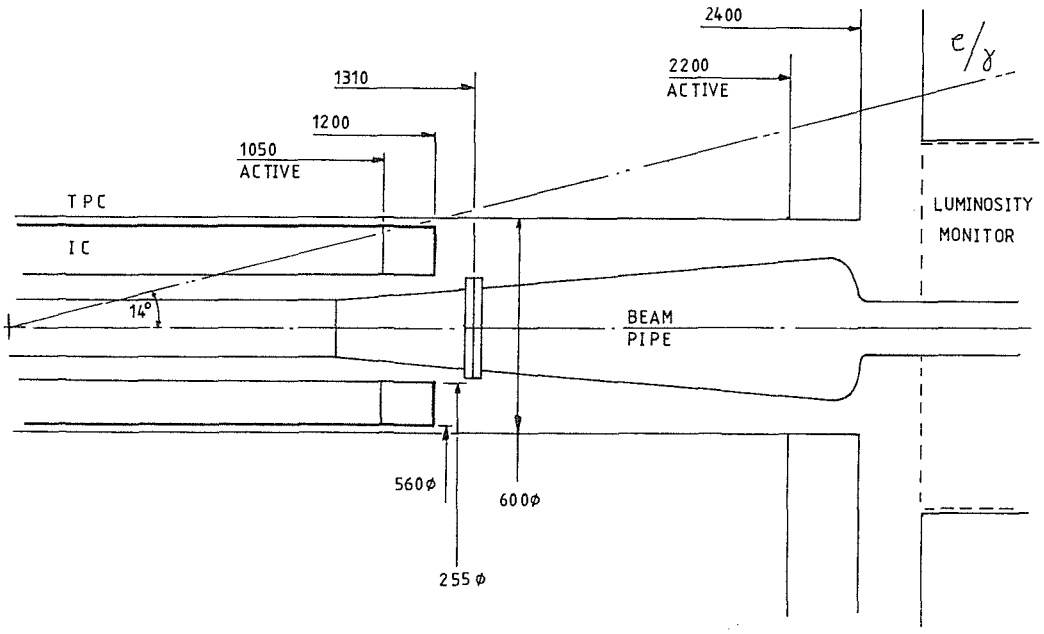

Fig. 7.1

Table 7.1
Dimensions of the inner chamber

Inner radius	128 mm
Outer radius	280 mm
Over-all length	2400 mm
Radii of sensitive layers	142 mm
	152 mm
	170 mm
	180 mm
	222 mm
	232 mm
	250 mm
	260 mm
Active length	±1050 mm
Number of cells/sensitive layer	128
Cathode strip width	20 mm
No. of cathodes/sub-chamber	104
Sense wires W/Au	30 μm diameter
Field and guard wires BeCu/Ag	100 μm diameter

7.2 Mechanical construction

The basic construction is shown in Fig. 7.2. The chamber is divided into four sub-chambers, rigidly connected. Each of these contains two layers of 128 sense wires alternating with pairs of field wires; they are separated by a layer with 256 guard wires. The azimuthal position of the sense wires is offset by half a cell from layer to layer in order to resolve left–right ambiguities and achieve good two-track resolution. The tentative layout is shown in Fig. 7.3, although the actual cell configuration is still being optimized. The wires are held in aluminium end-pieces in feedthroughs, the position of which is known after optical alignment to better than 20 μm. The sub-chambers share a common gas system (see Fig. 7.2). An argon/CO_2 mixture is anticipated, although the addition of a small amount of hydrocarbon may become necessary in order to achieve a reasonable drift velocity and the required precision. If this is so, the mixture will not be explosive.

To reduce the material in the detector to a minimum, the walls of each sub-chamber will be constructed by bonding together 1 mm thick polystyrene sheets. Present estimates suggest that a 6 mm thickness is necessary for the internal walls between sub-chambers and 8 mm for the over-all inner and outer walls. Estimates of the radiation lengths are given in Table 7.2. For the z readout hooped cathode strips, 20 mm wide, are provided by etching aluminized kapton sheets which form the inner walls of each sub-chamber. The cathode signals are extracted by fine wires, spot-welded to the aluminium and then passed through the kapton and then to the ends.

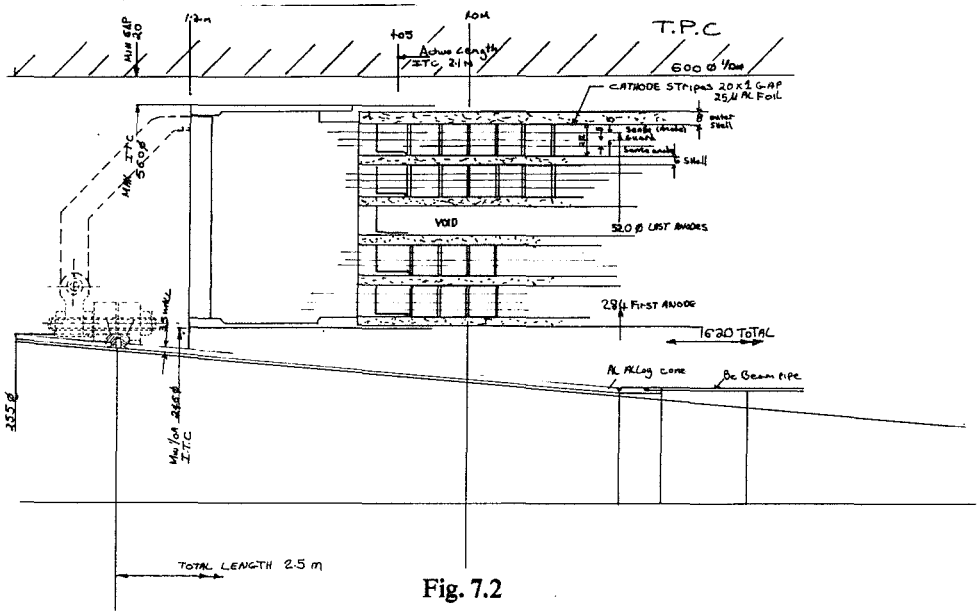

Fig. 7.2

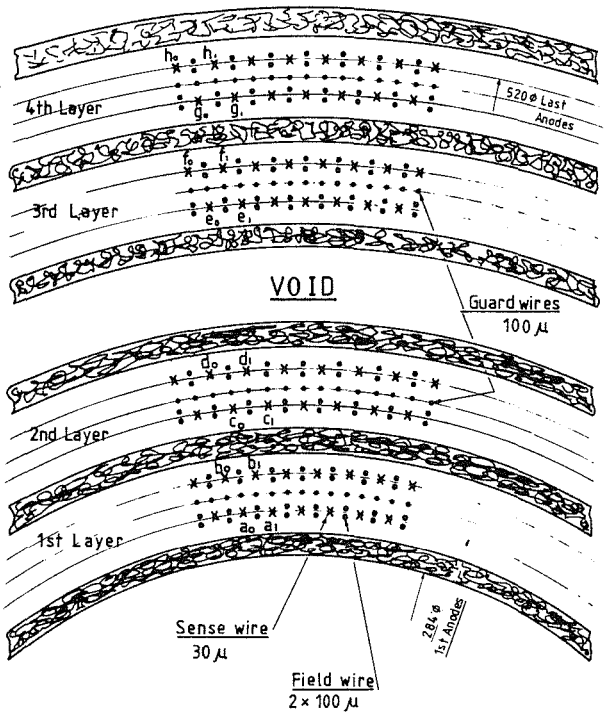

Fig. 7.3

Table 7.2
Average radiation length for normal track (%)

6 shells (polystyrene, araldite, aluminized kapton)	0.86
1024 sense wires	0.02
2048 field wires	0.11
1024 guard wires	0.06
Argon	0.12
Inner wall	0.15
Total to middle of chamber	~ 0.6
Total for the whole chamber	~ 1.2

As the chamber provides an essential part of the Level 1 trigger, it must be highly reliable and must not be made inoperative by a broken wire. The shells also perform this function, as a broken wire will affect at most two layers. Additionally, the high-voltage supply will be highly segmented so that small groups of cells will be able to be switched off independently.

The mechanical support of the chamber is not finalized. It will be connected rigidly to the TPC and will move with it when the TPC is aligned. It is anticipated that it will also be connected to the flange in the beam cone just beyond the end of the chamber.

7.3 Electronics

7.3.1 Drift-time measurement

Single-hit electronics is used, the important two-track resolution being obtained by means of high granularity and staggered cells. The anode wires are taken through the feed-throughs to a compartment still within the gas volume where decoupling capacitors and terminating resistors are located. This arrangement isolates the high-voltage system inside the gas volume, apart from the external high-voltage connections to the supply cables. The anode signals then pass via coaxial cable into emitter followers mounted in an electronics box situated in front of the upper part of the forward detector. From the emitter followers, the signals pass via coaxial cable to amplifiers and constant fraction discriminators located close to but outside the detector. The discriminator output is fed into the TDC system. A schematic diagram is shown in Fig. 7.4.

7.3.2 Cathode readout

The cathode signals are fed via coaxial cable to amplifiers in the electronics box situated near the forward detector. They then travel via twisted pairs to discriminators outside the detector, and digital signals from the discriminators go to the trigger processor. This is also shown in Fig. 7.4.

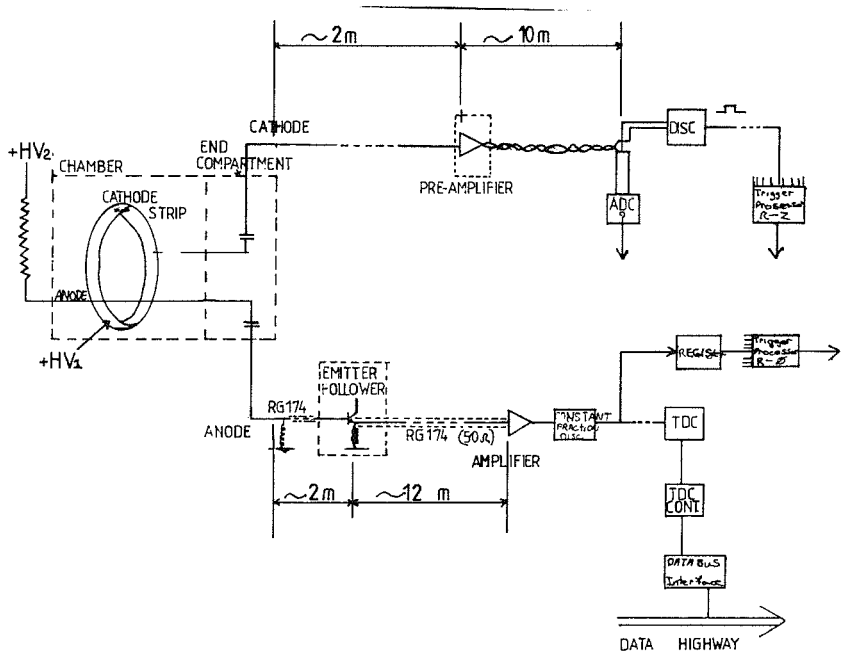

Fig. 7.4

7.4 Trigger processors

7.4.1 The (rφ) trigger

This will use an algorithm based on patterns of hit anode wires to give an estimate of the number of tracks, $n_{r\phi}$, emanating from the origin with $p_T > 1$ GeV/c. The pattern of sense wires is shown in Fig. 7.3. The 256 track cells can be defined by

i) a_0 AND (b_0OR b_1) AND c_0 AND (d_0 OR d_1) AND e_0 AND (f_0 OR f_1) AND g_0 AND (h_0 OR h_1),

ii) (a_0 OR a_1) AND b_1 AND (c_0 OR c_1) AND d_1 AND (e_0OR e_1) AND f_1 AND (g_0 OR g_1) AND h_1, etc.

Each track cell has 8 inputs which define an address in a 256-word memory. The memory contents can reveal the number of inputs present and this can be compared with a programmed number to decide if that cell contained a valid trajectory. The positive outputs from the comparators are summed to give $n_{r\phi}$, which is sent to the Level 1 trigger logic.

7.4.2 The (rz) trigger

Patterns of cathode hits are compared with masks corresponding to tracks leaving the origin in z in the range $0 \pm \Delta z$. The logic is similar to that for the (rφ) trigger; sufficient cathodes are ORed together to define all possible valid trajectories passing through each of the innermost cathodes. The number of cathodes to define a trajectory is again programmable, and the number of masks satisfied gives n_{rz}, which is sent to the Level 1 trigger logic.

7.5 An alternative design

An alternative design is being actively investigated. This would also have eight anode layers, but there would be no shells separating the chamber into sub-chambers and no cathode strips. The wires for all layers would be strung from single aluminium end-plates in two groups of four. A possible design of the end-plate showing the wire configuration is shown in Fig. 7.5. Reliability against broken wires in this case would be provided by wrapping a spiral thread of nylon around the guard wire layers as well as splitting the high-voltage supply into groups.

This design is mechanically considerably more simple; the main difficulty is the z readout for the rz trigger. Two analog methods using the anode signals, namely timing the signal to both ends and charge division, are being considered to see if the necessary accuracy and consistency can be achieved and an adequate fast trigger signal produced.

If this design were adopted, the rφ processor would be very similar to the one described above. For the rz trigger an analog method would probably be necessary to obtain the decision in time for the Level 1 trigger. An advantage of this design is that the (rφ) and (rz) trigger outputs will be correlated, i.e. (rz) trajectories will only be allowed on wires contributing to a valid (rφ) trajectory.

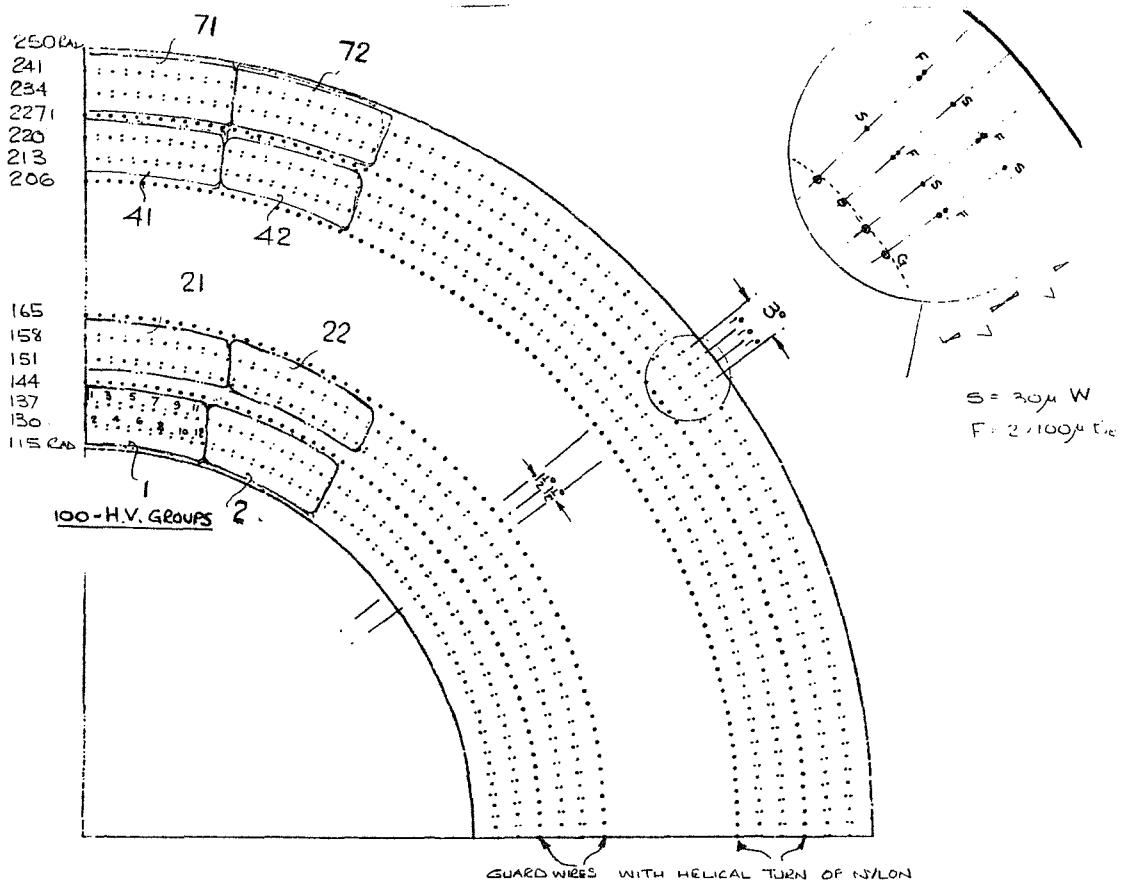

Fig. 7.5

7.6 Performance

7.6.1 Triggering

Any track with a $p_T > 1$ GeV/c leaving the origin with a polar angle in the range $-0.97 < \cos\theta < 0.97$ will pass through all sensitive layers and will give a positive output from the processors. Majority logic will be employed so that a trajectory will be allowed as long as the number of anodes or cathodes is greater than some programmable minima. These will be set at run-time depending upon backgrounds, the state of the chamber, etc. A 'fail-safe' system will be employed so that the processors will tend to overcount the number of trajectories if there is noise in the chamber. The time for a decision from the processors will be < 500 ns; the over-all time, including drift times, cable and electronics delays for the signals to be delivered to the Level 1 trigger processor, will be < 800 ns.

7.6.2 Tracking

The IC will give good tracking close to the beam-pipe and hence will complement the TPC. The aim will be for a setting error in $r\phi$ of 100 μm. The z information will not be used for tracking. The principal benefits are the following:

a) Two-track resolution: The small staggered cells enable the IC to give excellent two-track resolution in $r\phi$ although none in rz. If two close tracks pass through a common set of cells, each will record in half of them, and hence the two-track resolution depends upon the setting accuracy and the ability of the tracking programs to appreciate that the points do not all lie on the same track. This is $\sim 2\sigma_{r\phi}$ or 200 μm.

b) Improved track parameters: For tracks not emanating from the origin, the vertex point cannot be used. There are many such tracks resulting from decays, wall interactions, and conversions. The IC is important for establishing whether the vertex point can be used; if it cannot, it gives a valuable improvement in accuracy over the TPC alone. For tracks with momentum above ~ 5 GeV/c at $\cos\theta = 0$ the IC measurements yield an improvement of 1.5 in momentum resolution, a factor of 1.8 in ϕ resolution, and a factor of 3 in the error on the extrapolated position of the track at the origin.

c) Improved tracking efficiency: Low-momentum tracks and tracks at high $|\cos\theta|$ will only record on a few of the pad rows of the TPC. The efficiency of detecting such tracks will be greatly enhanced using the eight points from the IC. These tracks are important as they frequently result from conversions, decays and secondaries, and can be crucial to fully understanding an event.

7.7 Prototypes

A design for a prototype chamber is shown in Fig. 7.6. It is of full length but has only two sub-chambers. Work on methods of construction of the 2.4 m long polystyrene/kapton shells and on extraction of the cathode signals is in progress. The prototype chamber will be strung and ready for testing early in 1984.

For the alternative design, a second test chamber will be constructed to examine the timing and charge division methods for z measurement. Some encouraging results with timing the signals to both ends have already been obtained with a simple test cell containing a single sense wire. A σ_z of 6 cm over much of the length of the wire has been achieved.

Other investigations in progress concern the wire stability and whether supports will be needed. If they prove necessary, a scheme already designed for accurately locating the wires in the supports will require examination.

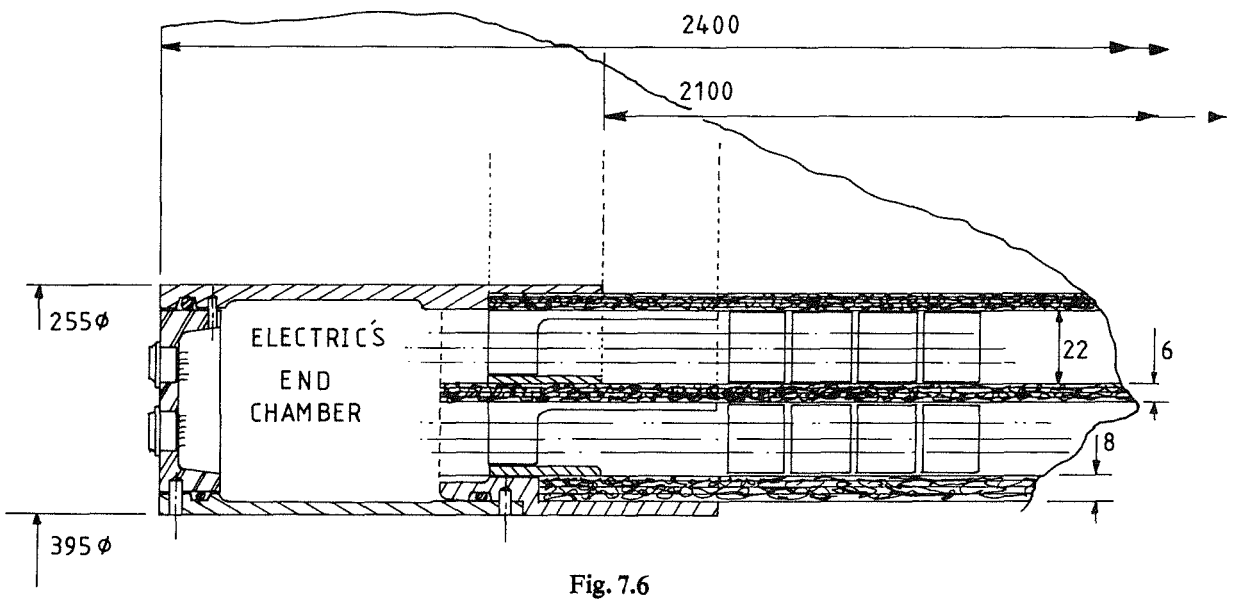

Fig. 7.6

7.8 Construction schedule

1983–1984 : Construction and testing of prototypes. Examination of methods of analog z readout. Tests of analog (rz) processor.

Early 1985 : Final decision on type of chamber. Detailed design of final chamber.

Mid-1985–End 1986 : Construction of Chamber

1987 : Chamber to CERN for tests and installation.

7.9 Costs

Cost estimates are given in Table 7.3.

Table 7.3
Cost estimate of inner chamber

		k£
Mechanical	Shells	20
	End flanges	14
	Wires/Capacitors/Cathodes/Feedthroughs	13
	Gas system	6
	Installation	20
		73
Electrics	Cables/connectors	30
	Amplifiers	33
	TDC system	50
	Cathode system	15
	Trigger processors	60
	High-voltage system	6
	Spares/contingency	20
		214
	TOTAL	287 k£

8. THE LUMINOSITY MONITOR

8.1 Introduction

The luminosity will be determined from the rate of Bhabha events at small scattering angles. There, the interference between γ and Z^0 is negligible and the cross-section is well known from pure QED. We aim at a systematic uncertainty of below 2%, so that the error in the annihilation cross-section will not be dominated by the uncertainty of the luminosity.

Such a precision can be obtained with detectors in which the scattered electrons are measured in coincidence on both sides of the interaction region. A precise measurement of angles is necessary since the Bhabha cross-section is a steep function of the scattering angle, and an energy measurement is essential to reject background both in the trigger and in the off-line analysis.

The basic element of the detector is an electromagnetic calorimeter. Its spatial resolution, however, is not adequate enough to define the acceptance domain with the required precision. A single-plane device to measure the impact point precisely is still not adequate because of the back-scattering from the shower counter itself, which generates false hits. A tracking device is then needed in order to measure the angle of the incoming electron.

The space reserved for the luminosity measurements consists of two zones symmetrically situated on each side of the interaction point in the distance 2450 to 3050 mm. Here the funnel of the beam pipe ensures an undisturbed acceptance for polar angles between 45 and 80 mrad.

We will install in these zones a pair of counting devices, each being a combination of a precision tracking device and a shower counter (see Fig. 8.1). For $\sqrt{s}$ = 100 GeV and the design luminosity ($L = 4 \times 10^{31}$ cm^{-2} s^{-1}), the expected rate of Bhabha events in the counters is $\sim$ 2 Hz.

Especially during periods when LEP operates below design luminosity, or when the energy is increased, it will be useful to have a device giving a more immediate, albeit less precise, measurement of the luminosity. We propose to build a forward monitor composed of a pair of shower counters placed at an equal distance from the interaction region behind the two superconducting quadrupoles (see Fig. 8.2). For the same luminosity, the rate of Bhabha events in this monitor will be two orders of magnitude higher, mainly because of the smaller scattering angles covered (> 8 mrad as compared to > 45 mrad).

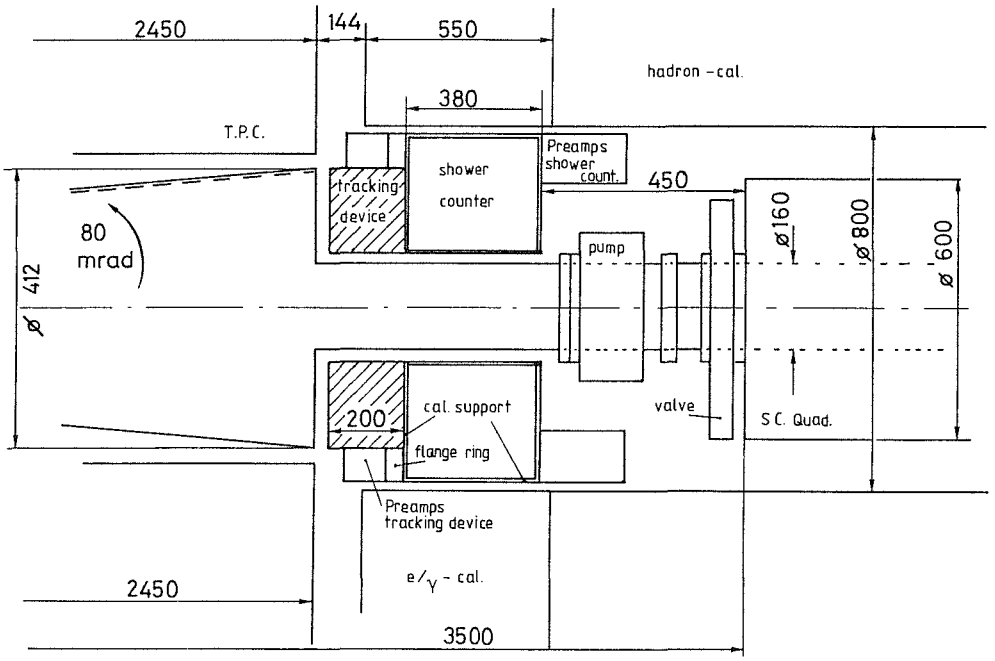

Fig. 8.1

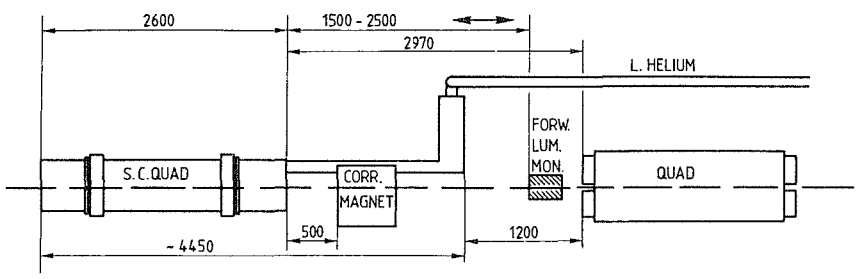

Fig. 8.2

8.2 The tracking device

8.2.1 Design

The tracking device consists of nine layers of tube chambers, separated in depth into three groups of three layers each. Each group has the same mechanical structure. A construction with separated tubes has been chosen, because they are known to work better than multiwire chambers in a high background. We use brass tubes, 10×10 mm^2 with 0.2 mm wall thickness.

Each layer consists of eight 45° sectors of identical design. There are three types of sectors, called A, B, and C, with different tube alignment as shown in Fig. 8.3. The first layer of each group is made of sectors of type A, the second of type B, and the third of type C. The relative orientation of the tube chambers within one group, as seen from the collision point, is shown in Fig. 8.4.

To avoid dead zones, the second group is rotated by 15° in the azimuthal angle with respect to the first group, and the third by 30°.

Each sector consists of 14 tubes covering the acceptance up to the opening angle of the beam-pipe funnel (80 mrad).

To minimize dead zones between two adjacent sectors, the wires are fixed to a "pertinax comb" at the end of the tubes (Fig. 8.5). In this way the dead space between the sectors — due to mechanics — is reduced to 6 mm. There is, however, a wider dead space due to the fact that the tubes are not cut perpendicular to the wires, giving a loss of sensitivity close to the end.

So as to make the mounting around the beam tube possible, the groups have been split vertically into two halves. Each half is contained in a gas box divided into three packages, each containing a group of three layers. The total amount of material in the tracking device corresponds to 0.5 radiation lengths.

The sectors in one half are fixed to an Al half-ring behind the nine layers with precision dowel pins. During the mounting of the device, the relative position of the two aluminium rings will likewise be fixed with precision dowels. This ensures the relative position of tubes and wires in sectors and between sectors to be within 100 μm.

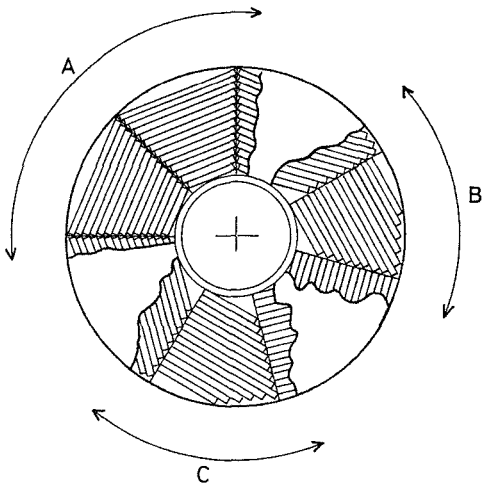

Fig. 8.3

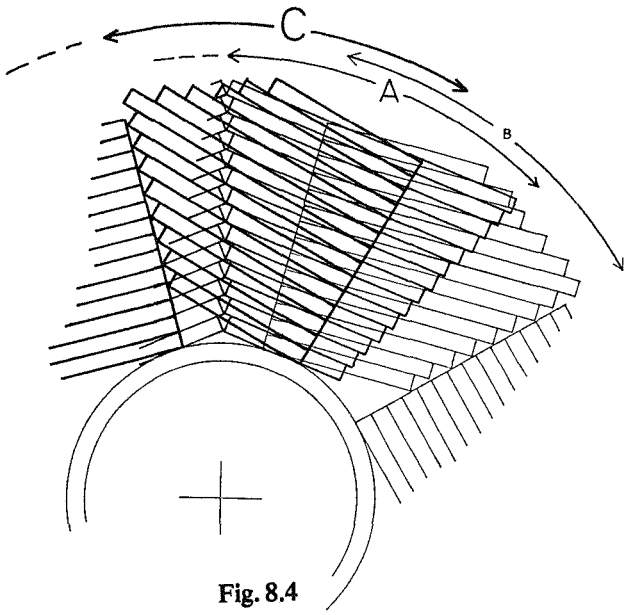

Fig. 8.4

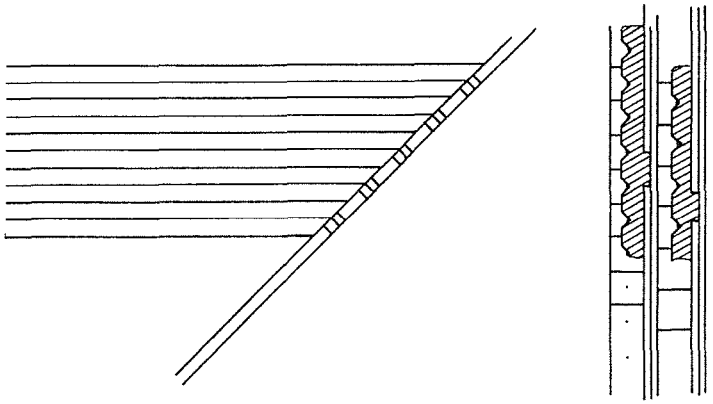

Fig. 8.5

8.2.2 Performance

The tubes are read out with TDCs. The acceptance is better determined off-line with a cut in the time distribution, to avoid the influence of the walls and of the inclination between them and the particle trajectories. The acceptance boundary is then known to $\sim 200\,\mu m$.

It can be shown [J.F. Crawford et al., Nucl. Instrum. Methods 127 (1975) 173] that by arranging the detector in sectors symmetrically with respect to the beam line, the acceptance can be calculated to first order knowing the radial distances between the acceptance borders. Misalignment with respect to the beam line is a second-order effect which can be accounted for, knowing the counting rate in the different sectors. This applies to our design.

The systematic error in the measured luminosity due to uncertainties in the acceptance is expected to be below 1%.

The reconstruction of tracks in the nine-layer device is precise enough to determine whether a track penetrating the acceptance zone points to the interaction region and enters the shower counter close to the centroid of the shower.

8.3 The shower counter

8.3.1 Design

The design of the calorimeter following the tracking device is similar to that of the electromagnetic calorimeter. It consists of 41 layers of wire tubes, operated in saturated proportional mode, interspersed between Pb converter sheets which are 3 mm thick (0.54 radiation lengths). The tubes have the same small cross-section, i.e. $(4.5 \times 3.5)\ mm^2$, as in the electromagnetic calorimeter.

The induced pulses from the wires are read on small cathode pads ($\sim 36 \times 36\ mm^2$) and transported to the edge of the calorimeter by strip lines. The size and position of the pads are arranged in projective tower geometry (~ 0.2 msr) as seen from the interaction region. The signals from the first 10, the middle 21, and the last 10 pads inside the towers are added separately to improve the π/e rejection.

The over-all structure of the shower counter is shown in Fig. 8.6 and the layout of the pads in Fig. 8.7.

As shown in Fig. 8.6, each of the two shower counters are split into half cylinders, contained in tightly fitting support shells.

The shower counter extends the angular coverage of the electromagnetic calorimeter. Only the four innermost rings of towers are used for luminosity measurement and triggering.

The total number of channels per shower counter is ~ 900, of which ~ 360 are part of the luminosity trigger and counter. The first stage of the readout electronics, which will be identical to that used in the large e–γ calorimeter, will be placed on the back end-plate of the shower counter. Thanks to multiplexers, the resulting signals from one counter can be transported to the remote stations by ~ 60 twisted-pair cables only.

The weight of each shower counter, including the support shell, is ~ 1100 kg.

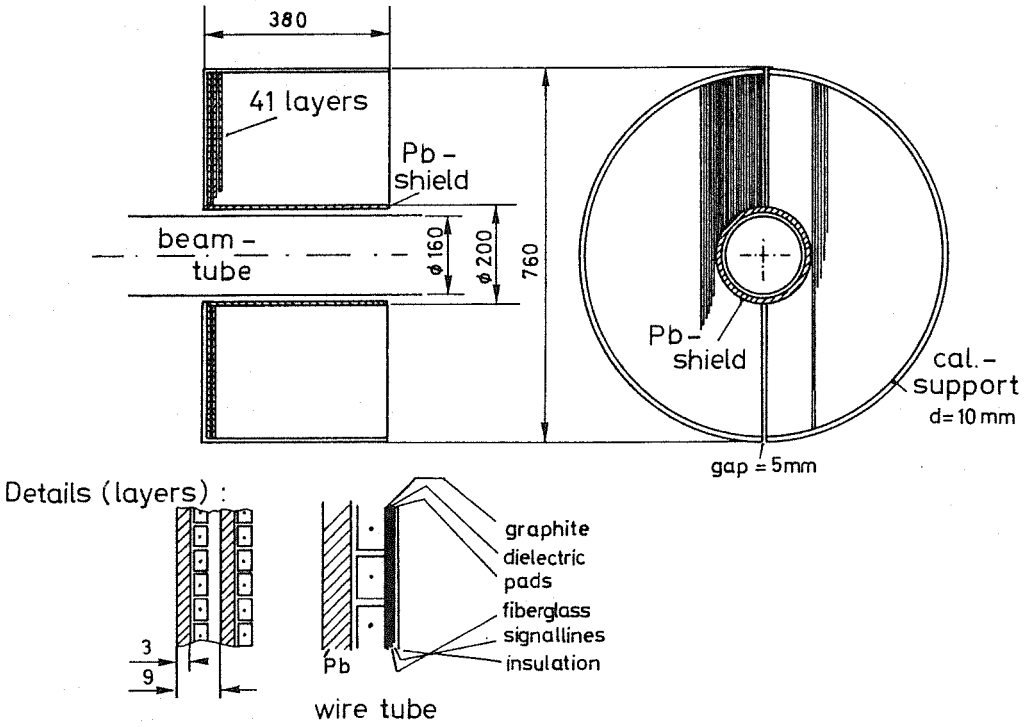

Fig. 8.6

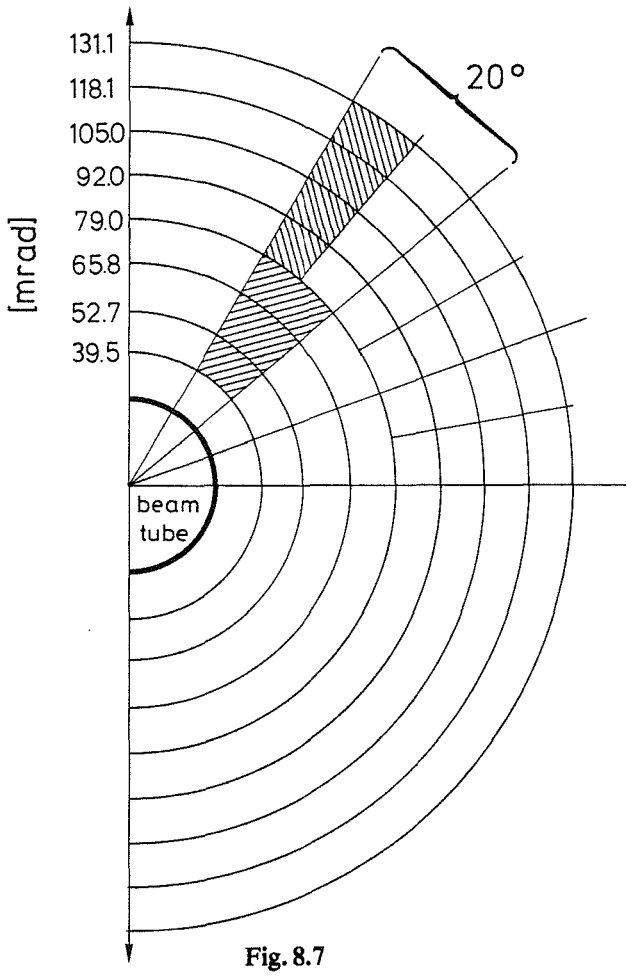

Fig. 8.7

8.3.2 Performance

The energy resolution, as extrapolated from the test results of a similar design, is $\sim 18\%/\sqrt{E}$. This is adequate, since the device is constructed to measure the energy of high-momentum electrons. The position accuracy for the electron as measured from the centroid of the shower is expected to be better than 5 mm.

The energy resolution for high-momentum electrons, combined with the angular accuracy of the tracking device, makes the luminosity monitor a useful device for tagging the photon–photon type of events.

8.4 Background

We do not envisage serious background to the Bhabha events in this counting device. In its angular range and at energies compatible with the beam energy, the e/μ and e/γ ratios are much more favourable than in any other kinematical region. Also, the fact that two electron-like signals are required, virtually limits the background to events with at least one genuine electron in the counter.

One otherwise serious background, the back-scattering of secondary electrons produced in the shower counter into the acceptance region, is greatly reduced by the track reconstruction of the tracking device.

8.5 Forward monitor

8.5.1 Introduction

Because of its much higher rate of Bhabha events, the forward monitor is useful under running conditions with low luminosity. It is an on-line monitor for the status of the machine and is of importance for beam steering. The systematic error is larger because the acceptance is less well defined.

8.5.2 Design

The monitor consists of a pair of calorimeters placed behind the two superconducting quadrupoles. The distance from the interaction region, which will be somewhere between 7.5 and 8.5 m, has to be determined together with the machine group.

Each calorimeter consists of 30 radiation lengths of 5 mm Pb converter sheets interspersed with 5 mm scintillator plates. The light is read out by photomultipliers via wavelength shifting light-guides (see Fig. 8.8).

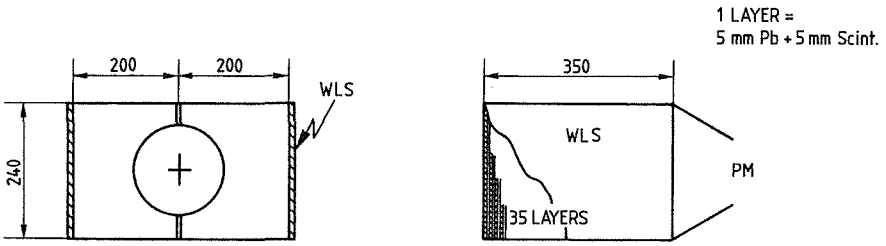

Fig. 8.8

8.5.3 Performance

The increase in the Bhabha rate compared to the rate in the luminosity monitor is two orders of magnitude. This is because the forward monitor covers smaller polar angles, and because of the outward deflection in the horizontal direction due to the superconducting quadrupole. In this way, scattered electrons from about 7 to 13 mrad are accessible but not for the full azimuthal range.

8.6 Construction schedules

Owing to the relative smallness of the device, the actual construction will not take place before 1986–87. Especially for the shower counter, it is possible that the final choice will be based on a different technique. We will continue construction studies based on the presented ideas, and the construction of the first prototypes will start at the end of 1983.

9. MINIVERTEX DETECTOR

9.1 Mechanical structure

The envisaged structure of the Minivertex detector is shown in Fig. 9.1.

The detector is dodecagonal in shape, made out of two layers of thin multi-electrode silicon detectors (MESDs) surrounding the pipe at a distance from the beam line of 85 and 105 mm, respectively; the angular coverage is $44° \leq \theta \leq 136°$ and $0 \leq \phi \leq 360°$. The whole structure of the assembled detectors looks like two concentric barrels.

For the inner barrel, which we call the "θ layer", the readout strips of MESDs run round about the beam line, whilst the outer "ϕ layer" has strips parallel to the beams. The total length of the barrels along the pipe is 230 mm; each detection layer is a mosaic of MESDs, 300 μm thick, with readout strips 20 μm wide and 250 μm apart.

The whole minivertex detector will be tightly assembled around the beam pipe in such a way as to be easily dismounted. To account for the requirement that charged particles and photons should not pass through high-density and high-Z mechanical supports, the material employed for the assembly of the detector is Rohacell 71 (manufactured by Röhm). It is a material of relatively good hardness, machinable, and with very low density (0.07 g/cm^3).

The "θ layer" is assembled on a Rohacell support made with eight independent "roman arches" shown in Fig. 9.2a; four assembled adjacent "roman arches" make up one half of the inner barrel. The two halves are mounted around the pipe and are held by a swallowtail-shaped plastic rod (Fig. 9.2b) which fits into suitable notches machined in the Rohacell. Six silicon crystals forming a θ layer element are glued with an amine-free epoxy on each "roman arch", as shown in Fig. 9.2a.

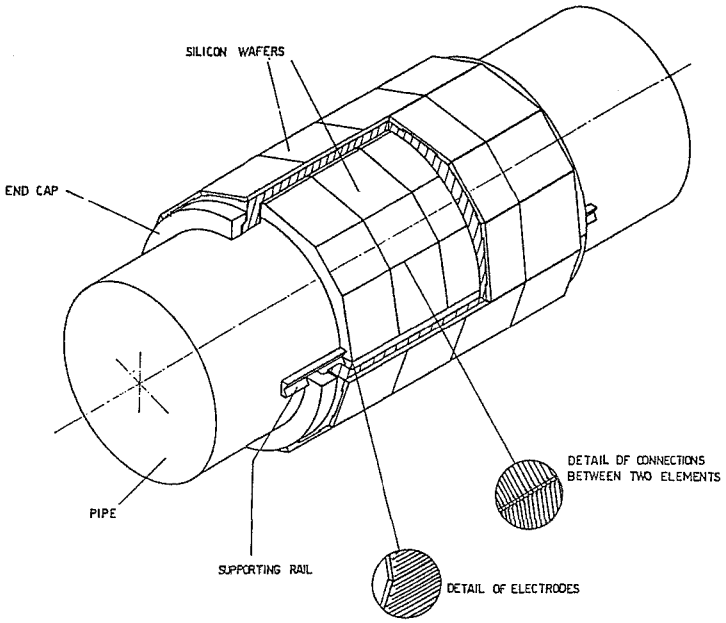

Fig. 9.1

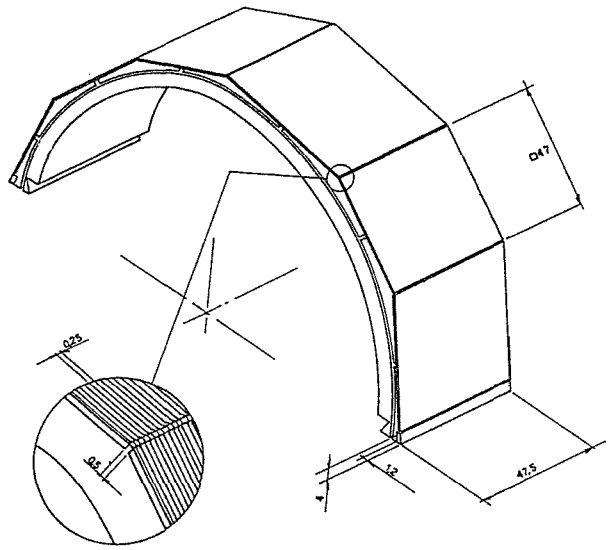

Fig. 9.2a

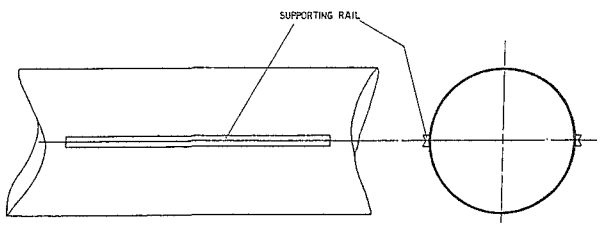

Fig. 9.2b

The two "roman arches" of the outer barrel (ϕ-layer) can be mounted after the θ layer assembly and are supported by the two end-caps shown in Fig. 9.1.

Twelve independent slides, each one carrying four MESDs, are mounted on the supporting outer structure. Each ϕ-layer element can be independently slid in and out of each side of the outer barrel on rails machined on the Rohacell surface (Fig. 9.3).

The modular structure makes the assembly of the whole detector easier, and ensures that a failure of some detectors can be repaired by simply replacing the corrresponding modules.

The readout ϕ strips of each crystal are microbonded to the corresponding strips of the adjacent crystal by means of an ultrasonic bonding machine using a 20 μm pure gold wire. The resulting element of four crystals is therefore equivalent to a single detector 23 cm long. In analogy, the readout strips of each of the six θ crystals glued onto a "roman arch" of the inner barrel are microbonded to the corresponding strips of adjacent MESDs to make a detection element acting as a single polygon-shaped crystal. At the extreme borders of each slide for the ϕ layer and of each "roman arch" for the θ layers are fixed two thin alumina (Al_2O_3) sheets, 0.6 mm thick, 4.2 mm wide, glued together for housing the required preamplifiers (see Fig. 9.4). The total weight of the two layers, including Rohacell structures, MESDs and alumina sheets, is about 400 g.

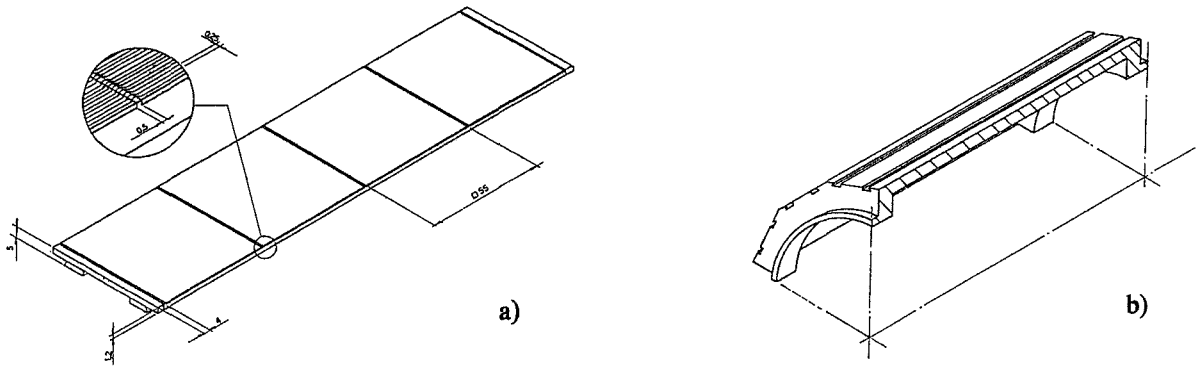

Fig. 9.3

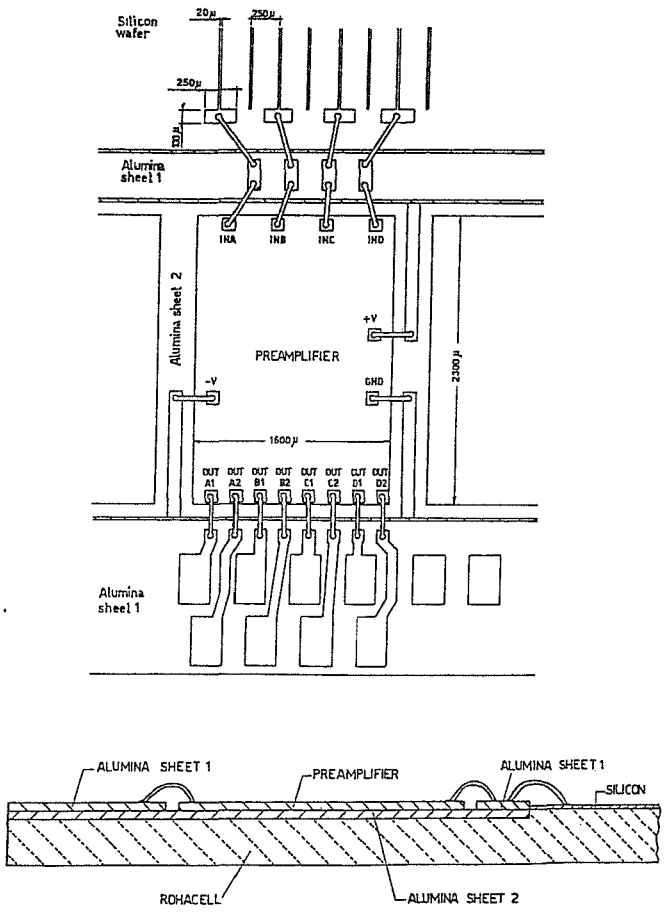

Fig. 9.4

9.2 Manufacturing of the silicon detectors

A single crystal will be a multi-electrode silicon detector working with resistive charge partition. Parallel strips will be deposited on one face of the crystal, and the junction on the opposite face will be covered by a uniform electrode. A resistive layer obtained in the interstrip space will allow resistive partition of the charge collected on the surface with a global resistance between two adjacent readout strips of $10^5\ \Omega$.

The manufacturing process will follow standard techniques in use in the electronic industry, such as silicon dioxide passivation, window opening, and lithography. Technology for detector building has already been developed in home laboratories, where the basic necessary equipment is either already installed, or will be very shortly. A contour area 200 μm around the edges of the individual crystal will remain protected by dioxide passivation to prevent superficial edge current leakage.

9.3 Readout electronics

Summing 1760 circular θ and 2640 longitudinal ϕ strips, we obtain 4400 readout channels. Table 9.1 shows the main features of a commercial preamplifier, developed specifically for MESDs.

Preamplifiers such as TRA 403 can be densely packed on a ceramic sheet with a density of one channel every 400–500 μm, satisfying our needs.

Figure 9.4 shows the proposed assembly of preamplifiers on the alumina sheets. The naked die is glued to the outer alumina sheet which contains power supply leads, whilst the inner sheet is used for the signals. Ultrasonic bonded gold wires transmit the input signals to the monolithic circuit, and the output pulses to the large output pads. The signal must be pulse-height analysed, so it is transmitted from the pads to the ADCs through specially-developed "twisted hair" whose characteristics are given in Table 9.2.

Table 9.1

Minivertex preamplifiers

LeCroy TRA 403	
Channel per die	4
Input impedance	$\leq 100\ \Omega$ d.c. (intended to be driven from a current source)
Outputs	Two per channel, complementary
Linear range	± 0.5 V each output
Gain	380 mV/μA $\pm$ 15%
Power consumption	$\leq$ 50 mW per channel
Rise and fall times	$\leq$ 12 ns for input capacity C $<$ 10 pF
Noise	25 nA for C $<$ 5 pF
Dimensions	1600 μm $\times$ 2300 μm

Table 9.2

Minivertex "twisted hair"

50 μm ϕ wire: coated copper
0.25 turns/cm
6 ns/m specific delay
0.3 dB/m attenuation
80 Ω characteristic impededence

Figure 9.5 shows the readout wiring. Considering that one charged track gives signals on two strips and assuming on the average 20 hits per event in each layer, the average meaningful information per event is 20 $\times$ 2 layers $\times$ 2 strips = 80 pulse heights + 80 addresses. Pulse-height analysis needs, for charge partition calculation, 10- or 12-bit ADCs; addresses need at least 10 bits. Thus one hit needs a 16-bit word for pulse height and a 16-bit word for address and, on the average, we have 160 16-bit words/event.

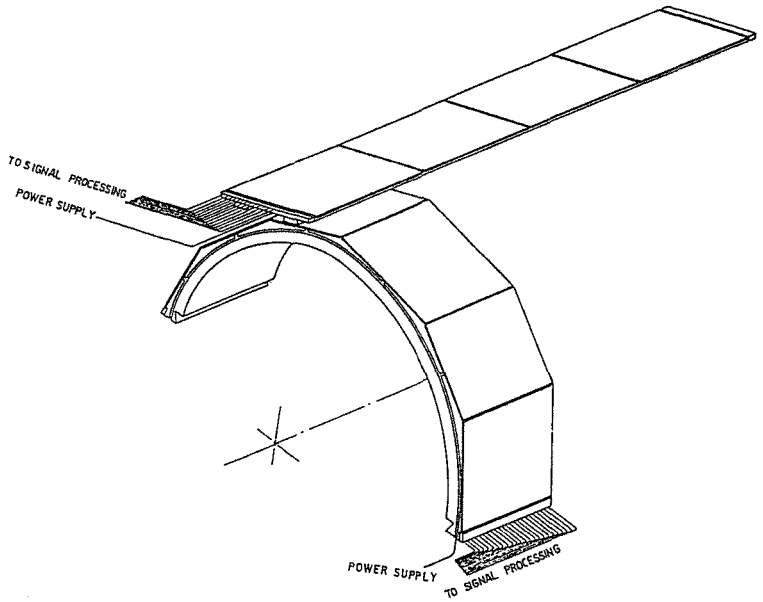

Fig. 9.5

Further improvements are expected in the next couple of years in the front-end electronics: noise reduction, increase of dynamic range, higher packing, possibility of reducing readout channels by a factor of 4 to 8 by multiplexing. Any of these improvements will simplify the packing and reduce dimensions, power consumption and wiring of the whole electronics.

9.4 Performance

The expected spatial resolution of MESDs operating in charge partition mode can roughly be evaluated by

$$\sigma = \ell \cdot \sigma_{\text{noise}} / \langle E \rangle ,$$

where ℓ is the pitch of the strips and $\langle E \rangle$ is the average energy loss in the detector.

Figure 9.6 shows results obtained for minimum ionizing particles using 0.8 mm thick MESDs with strips 120 μm wide, 400 μm apart. With $\sigma_{\text{noise}} = 15$ keV the resulting resolution is $\sigma = 21$ μm. An equivalent resolution can be achieved by decreasing ℓ and the thickness together.

For the ALEPH minivertex detector we have 300 μm thick silicon wafers, giving $\langle E \rangle = 80$ keV, and $\ell = 250\,\mu$m. With improved electronics we envisage $\sigma_{\text{noise}} = 8$ keV, giving a spatial resolution $\sigma = 25\,\mu$m.

In large multiplicity events, sometimes the charge partition and hence the position measurement is confused. The fact of the confusion, however, is known from the measurement of the ionization loss. A Monte Carlo study indicates that in 50% of heavy-flavour decays, all pertinent charged prongs are not confused.

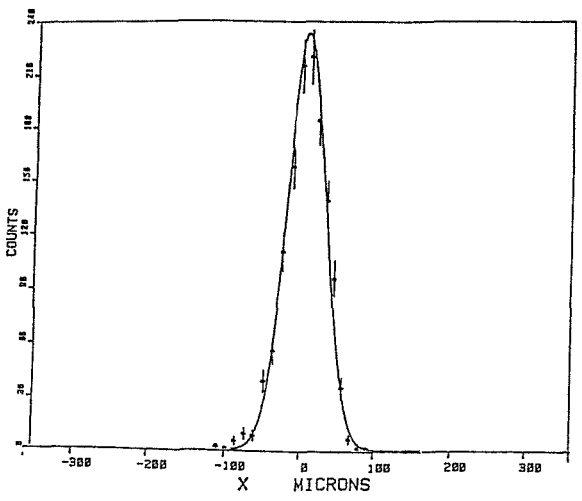

Fig. 9.6

9.5 Dead regions and radiation length

Excluding a 200 μm wide region at every edge, the entire surface of each detector element is active: so, inside the angular range covered, less than 1% may be considered as a dead region.

The over-all material traversed by particles emerging from the interaction region is less than 0.01 radiation lengths. The copper wires of the twisted hair coming out of the ϕ layer run along the end-caps and those from the θ layer along the supporting rail. In these two small regions, about 0.05 radiation lengths are concentrated. Further reduction of these figures could be achieved by introducing the multiplexing just after the preamplifier.

Costs schedule are summarized in Table 9.3.

Table 9.3

Costs

	kSF
96 silicon wafers + mechanics	90
Power supply	90
5000 channel preamps (15 SF each)	75
* Shift registers 8 to 1	106
Cables + connectors (30 m length)	65
* ADC × 700 channels	70
4 crates ACD	37
Air conditioning and humidity control	30
Data reduction	53
Calibration	30
Monitoring	15
Test and assembly	200
Tooling (ultrasonic μbonding machine, μ-positioner, precision lapping machine)	286
External mechanical work	80
Total	1227 kSF

* If multiplexing is not considered, these two items are unified under the item 4400 ADC channels for a cost of 440 kSF. In this case the grand total becomes 1597 kSF.

10. BEAM PIPE AND BACKGROUNDS

From experience at PETRA, a beam-pipe design can be at best only temporary: it is therefore necessary to retain some flexibility in the detector design around the pipe. The proposed beam-pipe arrangement relies on current background calculations [1,2].

10.1 Expected backgrounds

10.1.1 Synchrotron radiation

We expect direct synchrotron radiation from the LEP bending magnets to be taken care of by remote collimators in the straight section (at ~ 100 m from the intersection region). The yield from the insertion quadrupoles is very much model-dependent, being quite sensitive to the beam size. Calculations indicate that no special masking is required in the part of the beam pipe which is within the experiment, provided that the pipe diameter is in excess of 120 mm. Since the photon yield depends crucially on the tails of the beam profile, it appears reasonable to allow for some safety. For a diameter of 160 mm and collimators at ±8 m, one expects [2] within the detector (±2 m), a few $\times 10^4$ γ /(s/mA) leading to $< 10^5$ γ/s at normal LEP operating conditions (50 GeV). This is typically one order of magnitude less than the (observed) PETRA yield at 17 GeV, and it is presumably due to the smaller solid angle of the detector for photons back-scattered on far-away collimators.

10.1.2 Off-momentum particles

Bremsstrahlung of the beams on residual gas will produce degraded particles which can be dispersed outside of the nominal phase space. Such a halo will initiate showers when striking the beam wall next to the experiment, therefore producing background triggers. The corresponding yield depends crucially on the vacuum quality in the whole straight section and the weak-bend part of the arcs. With 10^{-9} Torr in the arcs and 10^{-10} Torr in the straight section, calculations indicate [2] that about 2×10^{-2} particles will exit the beam pipe in the experiment for every beam crossing. These particles will be confined very closely to the beam pipe; furthermore, it is necessary to shield against showers produced upstream of the experiment by covering the beam pipe with a lead sleeve, thick enough to contain showers laterally. Also, a reduced pipe diameter beyond ±2.4 m will help in that respect. In any case it would appear desirable to lower the yield of scattered particles: since collimating is not easy, one should try to reduce the residual pressure as much as possible.

10.2 Beam-pipe design

The currently foreseen beam pipe is shown in Fig. 10.1 and consists of three sections:

- a central part, 160 mm in diameter, 1.5 mm thick (Be), extending to ±750 mm;
- a trumpet-shaped part to clear a maximum angle of 80 mrad for the luminosity monitor free of excessive material thickness; the flange at ±750 mm is necessary for mounting the inner chamber;
- an external part, 140 mm in diameter, with lead lining, extending through the luminosity monitor and the low-β quadrupoles.

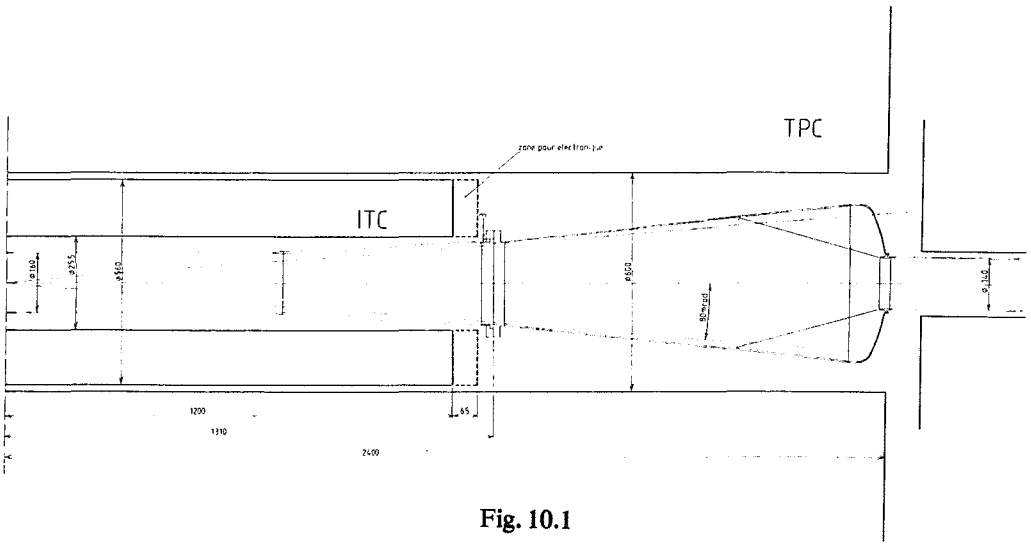

Fig. 10.1

[1] The Pink Book, CERN/ISR/LEP/79-33 (August 1979).
K. Potter, Background prospects at LEP, Villars meeting, ECFA 81/54 (June 1981).
[2] K. Potter, private commmunication.
P. Roudeau, private communication, LEP-note to be published.

11. THE TRIGGER

11.1 Introduction

The aim of the trigger is to reduce the rate of background events to a level acceptable for the TPC (a few hundred hertz) while accepting all good events. It is worth noting that the expected rate of good events under the Z^0 peak, assuming the design luminosity, is of the order of 1 Hz. The first trigger signal should come within $\approx$ 1.5 μs, and open the gate of the TPC; subsequent trigger signals will then reduce the rate to a level tolerable for tape writing. In general, the detectors start their digitization upon arrival of a bunch crossing signal. The readout is then inhibited in case the trigger condition fails. A high level of flexibility has to be built into the triggers since the nature of backgrounds and their rates are not well known. The main source of background events, which should be rejected by the trigger, are beam–wall interactions of off-momentum particles. The end-cap calorimeters and the inner chamber will be most affected by this background. Synchrotron radiation, on the other hand, will probably not be seen by the calorimeters but will produce random hits in the chambers.

The trigger system is organized in three levels:

1) Level 1 trigger: This trigger will be fast. The total delay from beam crossing to input of the TPC gating system will be $\approx$ 1.5 μs. This corresponds to $\approx$ 10 cm lost space close to the TPC end-plates. The rate must not exceed a few hundred hertz. The trigger serves to open the TPC gate and to initialize the Level 2 trigger. It will not introduce any dead-time, since beam crossing occurs only every 23 μs.
2) Level 2 trigger: This is based mainly on the TPC and decides whether to continue processing the data or to clear the data acquisition system in case of failure. This trigger should reduce the rate to less than $\sim$ 10 Hz. The information is available a few microseconds after the end of the TPC drift-time, say 50 μs after beam crossing. The dead-time introduced in this stage will be of the order of a few percent.
3) Level 3 trigger: To reduce the Level 2 trigger rate to a rate acceptable for tape writing (1–2 Hz) a post read-out selection process, based on sophisticated processors acting on the whole data, will be used. To reduce dead-times to a tolerable level, several processors will have to be operated in parallel.

A readout supervisor will be the central logic to coordinate the various trigger levels and to distribute the appropriate signals to the TPC and the data-acquisition system.

11.2 The Level 1 trigger

The main idea of this trigger is to be sensitive to tracks and/or energy deposits. Inspired by the experience of PETRA and PEP experiments, we propose a trigger which is satisfied by any one of the following conditions:

i) at least two minimum ionizing tracks (minions);
ii) at least one minion track and one energy cluster (low threshold);
iii) total electromagnetic or hadronic energy (high threshold).

In addition to these three main triggers there will be a number of special triggers: for instance, triggers on single photons; two-photon events with an electron tag; very low angle e^+e^- or $\mu^+\mu^-$ events.

The topological acceptance of two tracks and the energy threshold of clusters can be varied to find the best compromise between the acceptance of good events and the background rate. The trigger system is redundant, i.e. most of the events will fulfil more than one trigger condition.

The detector elements used in the Level 1 trigger are:

1) the inner chamber (IC),
2) the hadron calorimeter,
3) the electromagnetic calorimeter,
4) the muon chambers,
5) the luminosity monitor.

All input to the trigger logic will be digital. Discriminators are used to set a minion threshold, and flash ADCs will be needed to obtain energy. The components will be placed close to the subdetector electronics, whereas the trigger logic will aim at being compact, and will be situated as close as possible to the TPC gating control.

Tracks will be defined by a track segment found in the IC and a signal above minion threshold in a segment of the hadron calorimeter. Track segments in the IC alone may not be sufficient, since this chamber is very close to the beam pipe and is therefore exposed to heavy background. Geometrical correlations between the track segments in the IC and the calorimeter information will not be required.

1) The IC has eight layers of sense wires and eight cathode layers, one before and one behind each of the four pairs of sense wire planes. Two trigger processors are used to search for track segments in the rϕ plane and in the rz plane.
   The rϕ trigger will use an algorithm based on patterns of hit anode wires to give an estimate of the number of tracks $n_{r\phi}$ emanating from the origin in x,y with $p_T > p_{Tmin}$. At present, a p_{Tmin} of 1 GeV/c is envisaged. We are examining the possibility of making p_{Tmin} programmable.
   With the digital z information from the cathode strips, a similar technique to that in rϕ can be employed for the rz trigger. The patterns of cathode hits are compared with masks corresponding to tracks leaving the origin in z in the range $\pm\Delta z$. The value of Δz is chosen depending upon the expected σ_z of the primary vertex and the resolution from

the cathode hits. Basically, each cathode on the innermost layer can define an rz trajectory, and then sufficient cathodes on the outer layers are ORed together to cover all possible z trajectories from $0 \pm \Delta z$ passing through the particular innermost strip. The number of such trajectories is n_{rz}. The numbers $n_{r\phi}$ and n_{rz} from the IC processors are passed to the Level 1 trigger logic.

A special logic will be set up to search for back-to-back pairs in $r\phi$ and rz. This trigger is of particular interest for e^+e^- or $\mu^+\mu^-$ pairs at very small angles, where the TPC trigger logic might not be fully efficient.

2) The hadron calorimeter uses layers of streamer tubes, with pad readout arranged in 1344 towers. A minion particle deposits an energy equivalent to 2.5 GeV. The signals are fast, and the signal-to-noise ratio is large enough to set a safe threshold for minimum ionizing particles.

   For triggering on energy the granularity of 1344 towers is too large. Several towers must be added to form one trigger segment. A reasonable choice of one such segment is 30° times 30° solid angle coverage. The barrel would then be divided into 12 ϕ-bins and 4 θ-bins. For the end-caps, 6 ϕ-bins and 2 θ-bins are adequate. This leads to a total of 72 trigger segments. On the average, 22 towers will be summed to one of the 72 trigger segments, and 6-bit FADCs digitize the energy for further analysis in the trigger logic.

   Discriminators set a threshold for minions in each single tower. Minions passing from one tower to the next are recognized in at least one of them if the discriminator threshold is lower than half the signal. Dead zones between the calorimeter elements will, however, create losses in acceptance. Depending on the angle of incidence, inefficiencies of the order of a few percent for one track are expected.

   To ensure a uniform energy response for clusters, four segments (2 ϕ-bins times 2 θ-bins) are summed after digitization. So we obtain 72 overlapping segments, four times the size of the original segments. A threshold is then set to recognize energy clusters. The lowest possible level above minimum ionizing must be of the order of 4–5 GeV.

3) The electromagnetic calorimeter consists of a total of 72000 towers, multiplexed in groups of 32. The segmentation for trigger purposes is the same as in the hadron calorimeter. About 1000 towers have to be combined to form a trigger segment. A minion traversing the calorimeter gives a signal corresponding to $\approx$ 250 MeV of electromagnetic energy. The noise in a trigger segment is expected to be $\approx$ 150 MeV. Because the front-end integrating amplifiers have a rise-time of the order of 1 μs, any discrimination for the fast trigger must be done at approximately half the full signal level. A low-energy threshold equivalent to $\approx$ 1.5 GeV should be feasible for a complete trigger segment, as should a total energy threshold of 10 GeV. A minion trigger is not possible for a complete trigger segment. The electromagnetic calorimeter may therefore not be used in the track logic but only to search for energy clusters.

4) The muon chambers represent a tool for helping the calorimeter in defining penetrating particles such as muons. In addition to the muon signal in the calorimeter, a hit in the muon chambers could be required.

5) The luminosity monitor: Trigger signals are derived from the calorimeters. Back-to-back correlation of two energy clusters forms the trigger on Bhabha events used as a monitor, and single hits are used as tags for two-photon events. The latter trigger requires additional signals from the main detectors.

The fast trigger logic is the central element of the Level 1 trigger. The signals arriving at the fast trigger logic system are shown in Fig. 11.1, as are the basic functions. The organization of the logic is shown in more detail in Fig. 11.2. The emphasis is again on flexibility and modularity, with the same circuitry and cards being used wherever possible. All energy thresholds and logic functions are programmable.

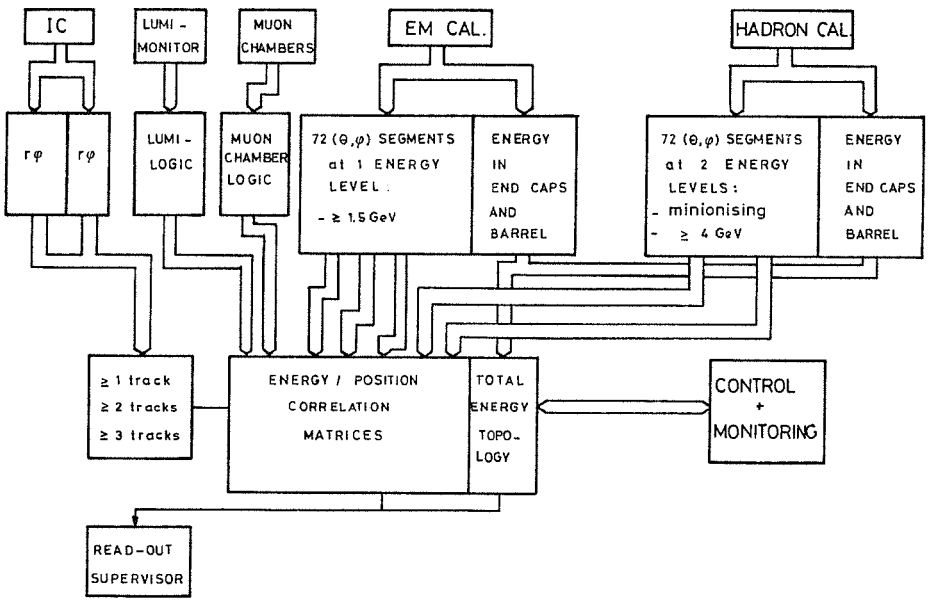

Fig. 11.1

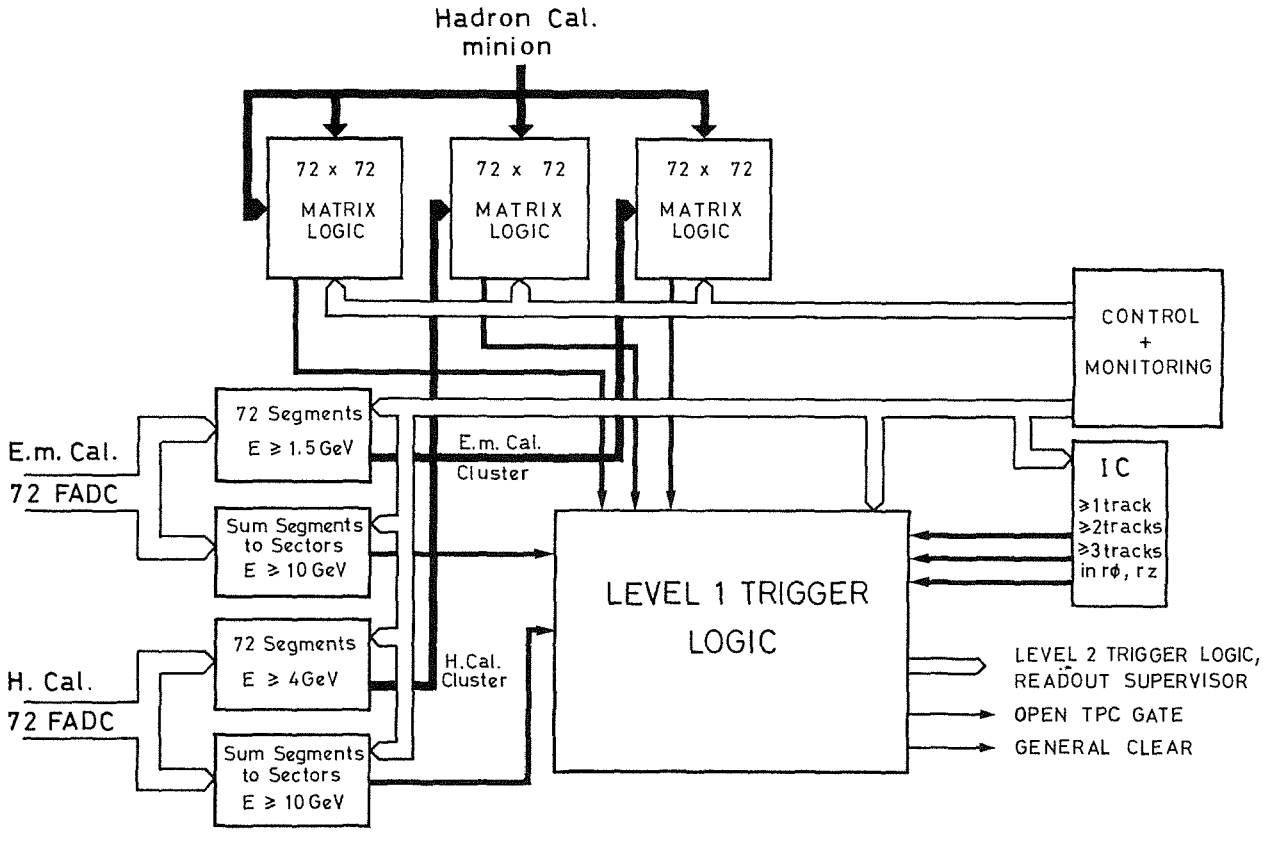

Fig. 11.2

In order to build track–track or track–cluster triggers described above, we feed two sets of signals into correlation matrices: i) the minion signals and ii) the energy cluster signals. These signals are derived from the FADC data by comparing them with preset values. The matrices are programmable; they can select any possible topology of two calorimeter signals. In response to background conditions, these topological correlations can be less or more restrictive. The output of these correlation matrices forms the input to the Level 1 trigger logic, where additional coincidence requirements, such as the number of tracks found in the IC, are added. The Level 1 trigger logic then communicates with the readout supervisor.

The third trigger condition is entirely based on energy requirements: the energy in one sector of the detector (e.g. the sum of 6 or 12 segments) exceeds a certain threshold ($\approx$ 10 GeV), or two such sectors are in coincidence, but at a lower energy level.

11.3 The Level 2 trigger

The basic requirement of the Level 2 trigger is that the tracks in the TPC point to the bunch-crossing region; this can be done progressively within the 40 μs TPC drift-time, with the final answer available a few microseconds after that.

The TPC trigger works on the rz projection using dedicated cathode pads on the TPC end-plates. Tracks with $p_T \geq 1$ GeV/c appear as essentially straight in the rz projection: the TPC trigger recognizes, in real time, straight tracks from the crossing point with a tolerance of $\Delta z \approx 10$ cm. Essentially any event with tracks coming from the crossing point will be accepted. The trigger logic would be fully programmable.

Each end-plate is divided into 12 overlapping segments (see Fig. 11.3). The segments would be arranged to correspond to the segmentation in ϕ used in the fast trigger associated with the IC. Each segment contains about 15 radial cathode pads arranged with greater density near the beam axis to improve detection efficiency for small-angle tracks. The logic associated with each segment (all segments being treated identically and independently) utilizes the fact that for a particular pad radius there is a one-to-one correspondence between drift time and track angle, for each track emanating from the crossing point. Thus to each pad i of radius r_i is associated a look-up table. The drift time t_i provides the address in this table, which contains the corresponding θ in the form of an address within a set of scalers. The content of the appropriate scaler is incremented by 1: this sequence is shown diagrammatically in Fig. 11.4. The look-up tables are fully program-controlled: thus the number and effective width of the θ-bins can be optimized in the light of experience. A reasonable number would be between 32 and 64.

For a track coming from the crossing point, all pad look-up tables will give the same angle; hence at the end of the TPC drift-time the corresponding θ-scaler will contain N, the number of pads. A track coming from outside the crossing region will give a set of different angles and will be rejected by a requirement on the number of counts in any θ scaler. This requirement will be programmable and can vary between different values of θ. For example, small-angle

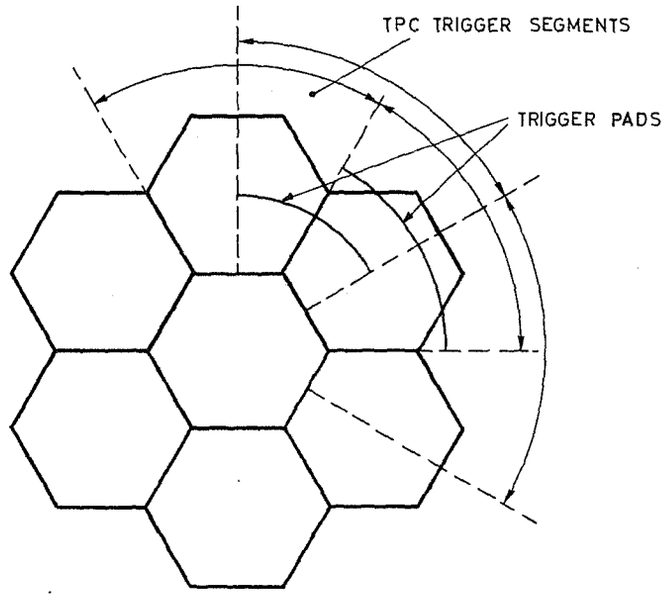

Fig. 11.3

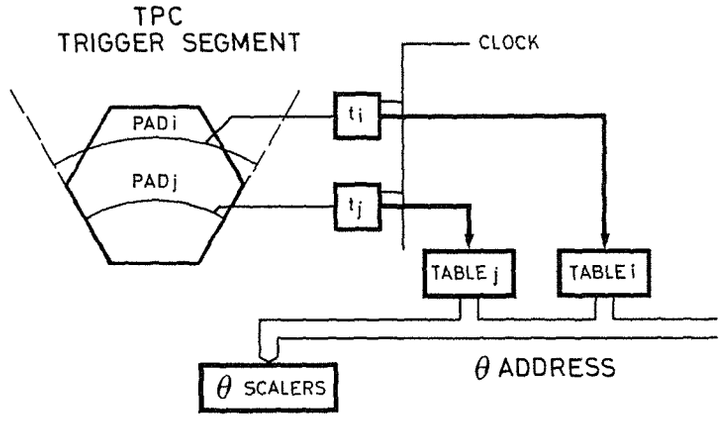

Fig. 11.4

tracks will require fewer hits because fewer pads are involved. Small-angle tracks present particular difficulties because: i) the number of pads involved will be small; ii) the z resolution deteriorates as cotan θ; iii) any background ionization problems are expected to be more severe near the beam pipe.

11.4 The readout supervisor

The crucial point of overlap between trigger and data acquisition is the synchronization of the trigger information with the data flow from the front-end electronics to tape: this task will be accomplished by a readout supervisor. As far as the trigger is concerned, this device can be seen as a "master" device controlling the readout performed by the distributed crate processors, whose result will be stored in buffers with multiple event capacity, and acted upon by the Level 3 processors. The readout supervisor is not intended to do any computation on the data; its input information is basically the result of the Level 1 and Level 2 trigger decisions. Its design and the way in which it influences the data flow reacting upon these trigger signals must be fixed inside the layout of the data acquisition system.

11.5 The cosmic muon trigger

For test and calibration purposes, a trigger on cosmic-ray muons is needed. In the absence of the beam crossing signal, which provides good timing for real events, a timing signal on cosmic muons must be generated. There are two ways of getting this: i) using the hadron calorimeter; ii) building a special scintillator telescope (two planes in coincidence) underneath the detector. The hadron calorimeter trigger would not need additional hardware. The signal is as fast as from a scintillator telescope; the coincidence of several layers of the calorimeter would provide a clean signal. The acceptance is well matched to the needs. This timing signal is then used as strobe for the Level 1 trigger, where track–track correlations between the top and bottom halves of the barrel are selected.

11.6 Monitoring and testing

All input and output signals of the Level 1 and Level 2 trigger logic will be stored in latches and read out with each event, and also, on a sampling basis, when the trigger fails. In this way most cases of malfunctioning of the trigger can be discovered. A further check of the performance of the trigger logic is provided by setting the input levels by software via programmable registers and comparing the output of the trigger processors with the expected pattern.

For setting-up and debugging, special test circuitry will be provided. The various components of the trigger will have explicit electronic tests built in.

12. DATA ACQUISITION

12.1 The scenario

We distinguish three phases for the implementation of the data acquisition:

- the development,
- the assembly and debugging,
- the running and maintenance.

During the development phase, the different sub-detectors will be built in places distributed all over Europe. Most of the devices will need a minicomputer during this time to check and debug the electronics, to develop the data reduction and readout hardware, and to implement the calibrations and the monitoring. In fact, such a sub-system can be as complex as our present experiments. The amount of effort for the software development is too large to be repeated for the final installation. Once a sub-detector arrives at CERN, it has to fit in with the other parts, not only mechanically but also as far as electronics, readout, software, and user interface are concerned. This forces us to plan the interfaces carefully and early enough to avoid duplication of work.

Phase 2 is the installation and integration of the sub-systems. Our experiment will be installed on two levels. All the electronics will be located in several movable counting rooms attached to the detector. The minicomputers of the sub-detectors (equipment computer) are there as well. Graphics terminals are needed close to the equipment for debugging and maintenance. The control of the experiment is on the surface. Figure 12.1 shows a possible layout. The terminal room serves for program development, monitoring work, and on-line analysis. The control console is used by the "shift master" for the over-all control of the apparatus. A service console provides access for tests, survey, debugging, etc. All noisy equipment stays in the "computer room" (line printer, etc.).

After running in (phase 3), the full control of the experiment is done from the control room. There is no need to have people working continuously underground.

With such a scenario, the data handling imposes some restriction. We are convinced that we need one family of computers running the same operating system on all sub-systems. Furthermore, we have to be sure that we can buy more powerful computers in five years from now and use the programs we develop today. In addition, this type of machine is needed at the home institutes for the development and the maintenance of the equipment. With these considerations, we have decided on the VAX family of machines and on the VMS operating system.

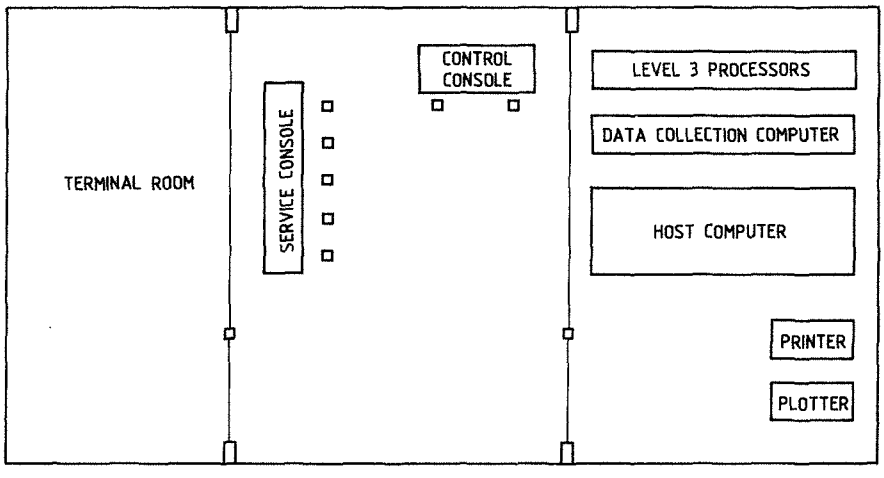

Fig. 12.1

12.2 A typical sub-detector

Figure 12.2 shows a typical sub-detector during the development phase. The front-end electronics contains, for example, the ADCs, raw data buffers, the zero suppression logic, and the crate processor for data reduction. FASTBUS is a candidate for the implementation. Depending on the requirements of the sub-system, the data reduction can be done on a crate level or on groups of crates. The reduced and preformated data are stored in event buffers and can be read by the equipment computer. The tasks to be performed are more or less the ones we are used to in present experiments, and they should include the local monitoring (histograms, constants, hardware survey) and the calibrations, so as to be able to run each sub-detector as stand-alone. Slow control functions such as the monitoring of gas-flow, control of high voltages, etc., might be implemented in CAMAC where appropriate. Nevertheless, CAMAC cannot be connected directly to the equipment computer, as we need to control any sub-detector from any equipment computer without recabling or complicated interconnections.

In the later installation phase, such a sub-detector has to be integrated with other sub-detectors of similar complexity. Therefore, we need connections to a European-wide network during the development phase to ensure a tight collaboration and centrally supported software development.

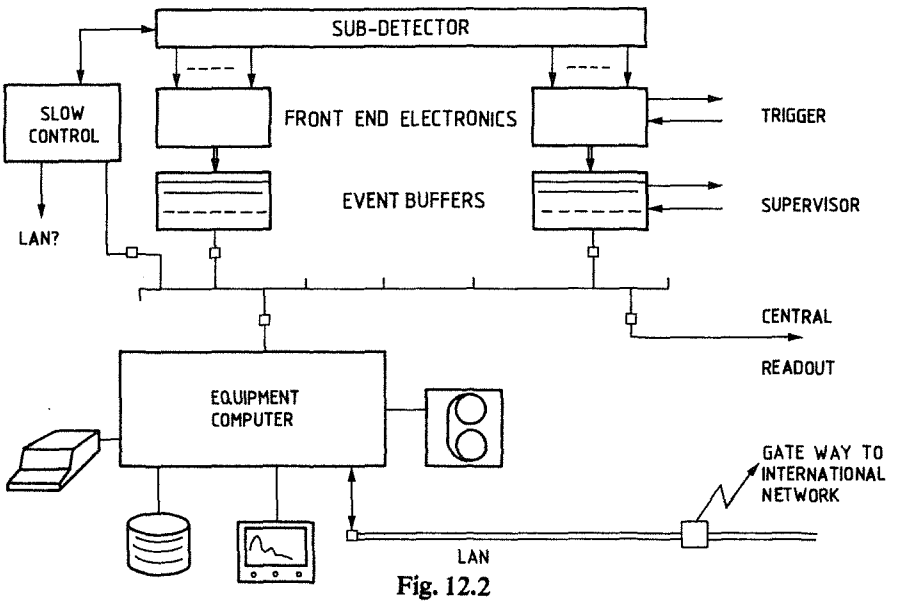

Fig. 12.2

12.3 Interconnection of sub-systems and general data flow

Two independent data channels are foreseen. A "fast" channel is used for data readout, a "slow" channel (Local Area Network, LAN) for control function and general communication. Figure 12.3 shows a first attempt to define the fast channel of ALEPH data-flow mechanism. Referring specifically to this picture, the following points of relevance can be stressed:

- Each sub-detector's front-end electronics is read by several "crate processors". This readout has to be fast and versatile, so it will be probably handled through FASTBUS devices.
- The result of the readout will be stored in local buffers with multiple event capacity, in order to de-randomize the data flow.
- The interface between all the computers and the FASTBUS will be standardized. No CAMAC will be connected to any computer directly: it will go through a FASTBUS or a CAMAC ETHERNET interface.
- The synchronization of this readout with the signals coming from the trigger electronics (Level 1 and 2 trigger results) will be handled by a read-out supervisor, which receives signals from the trigger logic, the timing signal from the LEP machine, and the "readout over" signal from the single-crate processors. The supervisor is responsible for enabling or stopping a readout upon trigger decision.

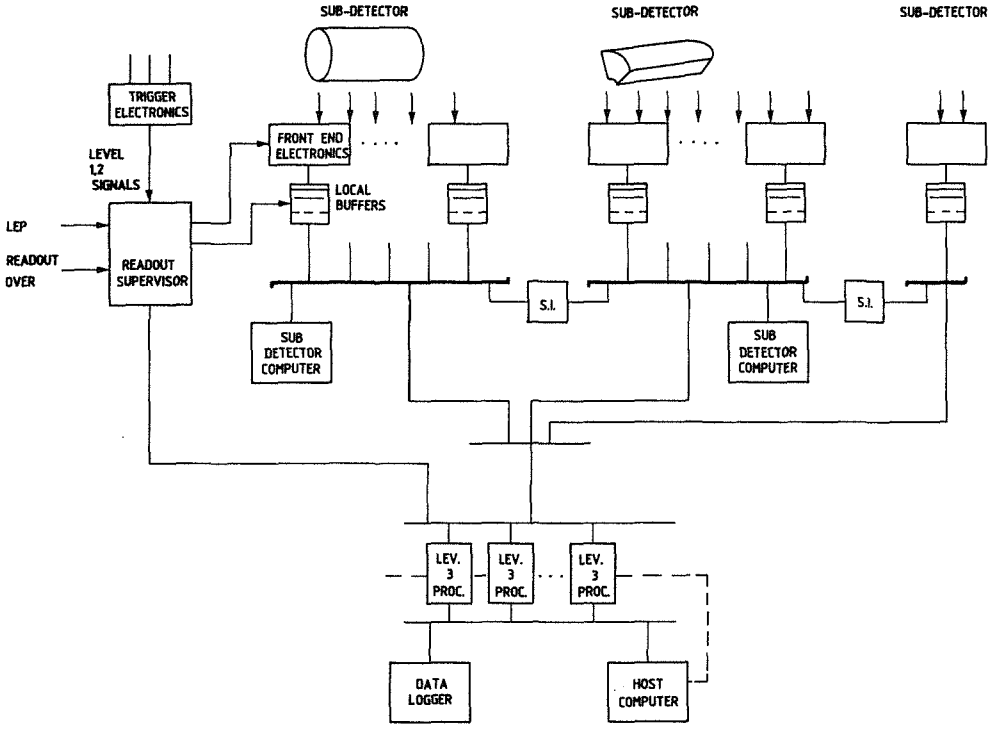

Fig. 12.3

- Also, the supervisor takes care of associating a particular event with one of the Level 3 processors, which should act as a further event filter before writing onto tape. These processors collect the bits of an event from the local buffers to build up a complete event in a single memory, and perform a rather sophisticated software trigger action.
- The Level 3 processors are linked to the Host Computer also via an extra control line, for downloading of programs and for checks, without interfering with the basic data-flow path.
- Owing to the rapid advance of technology with regard to the area of Level 3 processors, it is unwise at this stage to make any definite decision about the type and the number of the processors which will be used. What is clear is that the Bus structure into and out of the Level 3 processors section should be designed with sufficient flexibility to support a large number of processors of various possible types.
- The FASTBUS segment interconnections should provide (together with the LAN) a tool for backing-up one of the sub-detector computers from any other one, in case of faults or maintenance.

The second data path is a LAN which handles the "slow" traffic. It provides connections between intelligent terminals and the computers, and connects the main control console to the experiment. Depending on the LAN selected (the one which will be standard at CERN) it might be necessary to have two LANs in parallel to separate high-priority traffic, such as the steering of the experiment, from low-priority traffic such as watching histograms or program development.

Data collection and tape writing is separated from the monitoring and the on-line analysis. The on-line analysis computer needs to be the most powerful from the selected family of machines. Its tasks are on-line analysis, event reconstruction, central data base for programs, calibration, etc., general services and support for 3D high-resolution interactive graphics.

The mean length of the event buffer is $\sim 5 \times 10^4$ 16-bit words, 80% of which contains the information of the TPC.

12.4 Communications

During the development phase, the mail, programs, and documents have to be exchanged between people working on on-line computers in various institutes. This is done with the facilities provided by the computer manufacturers and/or nationally developed network architectures running over leased lines and the European PTT public packet-switching network.

At the experiment (phases 2 and 3), the communication is done with a LAN, connected to CERN's "backbone" for communication with the rest of the world. A good candidate for this LAN is ETHERNET, as it is compatible with the computer we have chosen.

12.5 Software environment

To produce an effective and user-friendly on-line system requires co-operation between the suppliers of the raw data, the on-line program developers, and the off-line program developers who are the consumers. One important aspect of this is to ensure compatibility between the on-line and off-line environments. This implies at least a common data definition and structure, a common programming language and documentation scheme, and a common set of utility routines.

Compared with today's experiments, the somewhat unnatural separation of the two "data handlers" should disappear.

13. OFF-LINE SOFTWARE

13.1 Introduction

The software effort of the ALEPH Collaboration is at present concentrated on two aspects:

a) the development and maintenance of a short-term ("Phase 0") Monte Carlo simulation program, and
b) the definition of the long-term data-handling strategy.

The latter aspect comprises:

i) choice of the software development and data processing environment;
ii) phase 1: job definition;
iii) phase 2: job organization;
iv) phase 3: job execution;
v) phase 4: data processing and program maintenance.

The "Phase 0" simulation program GALEPH is ready. It is described in more detail in subsection 13.2.

The Collaboration has clearly realized the importance of the software and has set up a group to work out detailed project specifications. This group has studied the problems of the software development environment. It is expected that a conclusion will be reached soon. The presently discussed alternatives are presented in subsection 13.3. Subsection 13.4 outlines the plans for the data-processing environment. Phase 1 of the software life-cycle, i.e. the definition of the software job, is getting close to its completion. A final internal document on this topic is scheduled for the middle of 1983. The present ideas on the planning of the software development are sketched in subsection 13.5.

13.2 The simulation program GALEPH

GALEPH is written in the framework of GEANT, and simulates the following detector elements:

i) The *inner chamber:* points in (r,ϕ) space, response of trigger pad rings.
ii) The *TPC:* points in (r,ϕ,z) space as measured by the pad readout; points in (r,z) space as measured with dE/dx wires; response of trigger pads; dE/dx information is *not* simulated.
iii) the *e.m. calorimeter:* e.m. and hadronic energy deposited in minitowers; the lateral size of e.m. showers and the longitudinal tower segmentation are taken into account.
iv) The *hadron calorimeter:* hadron energy deposited in towers; the response of the individual streamer tubes is *not* simulated.
v) The *muon detector:* two orthogonal coordinates of the muon impact point in the two muon detector layers.

The track and shower simulation includes bremsstrahlung, pair creation, hadronic interactions and particle decays. Electromagnetic showers are parametrized.

The magnetic field is a perfect solenoidal field with B_z = 1.5 T inside the superconducting coil. A simplified magnetic field in the flux return is taken into account for muon tracking.

Multiple scattering and energy loss of tracks is simulated.

The (r,ϕ) view and the (r,z) view of a hadronic event at $\sqrt{s}$ = 90 GeV are shown in Figs. 13.1a and 13.1b.

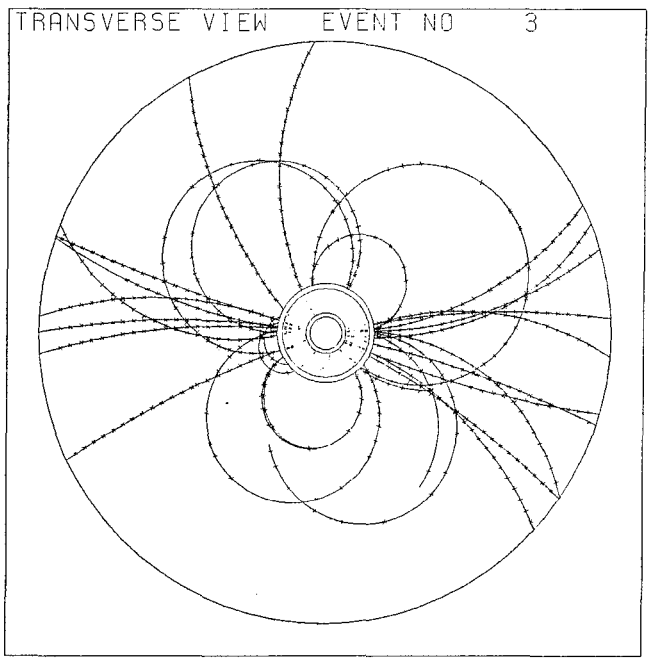

Fig. 13.1a

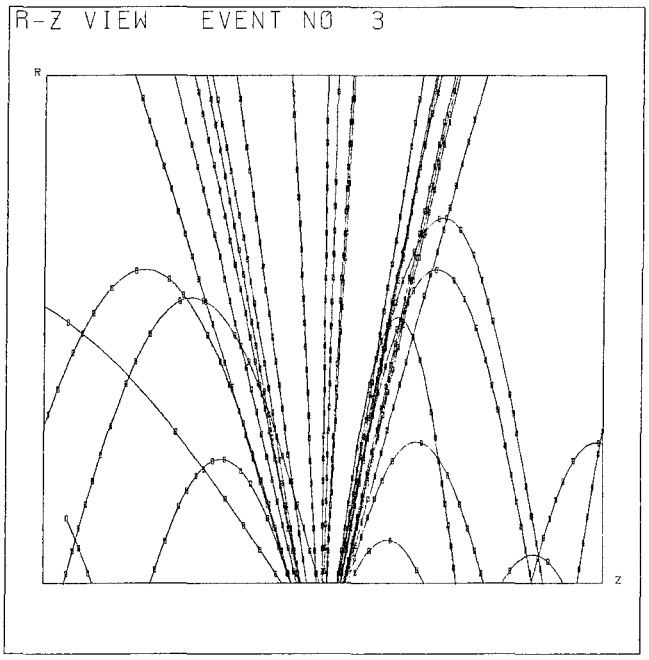

Fig. 13.1b

13.3 The software development environment

The implementation of the ALEPH software (Phase 3) will start around the beginning of 1985. Hence the software development environment must be defined rather soon. The question is non-trivial because of the rapid advance of computer hardware and software.

One possibility is to develop the software centrally at CERN, and indeed in this way large software systems have been made to work. This approach trivially solves the problems of working on different computer systems and of communication.

The ALEPH Collaboration is, however, bound to start out with the program development in many different sites, including CERN, which will also act as an integration station for the software. To succeed with this approach despite bad experience in the past, we need very careful planning of the software project, good communication between the laboratories, and *standardization of the software development environment,* comprising computer hardware, operating system, and software tools.

Experience with large software systems shows that an ever-increasing fraction of the work is spent on integration of program modules and validation. The program development is greatly facilitated if only one computer type and only one operating system is used throughout the Collaboration. The overheads for converting ever-changing programs to different machines, and errors resulting from misunderstanding and time delays in program updates, disappear. New releases of operating systems and tools can be incorporated at the same time and without the help of system programmers. Three possibilities for the ALEPH Standard Software Development Environment have emerged from the discussion (no final choice is yet made). These are:

a) VAX computers with VMS operating system.
b) IBM computers with VM/CMS operating system.
c) Personal work stations.

The personal work station option (c) is being investigated at CERN in some detail. It looks attractive since it has many desirable features. However, the present market situation is very rapidly evolving and work stations are still very expensive. There are many manufacturers offering incompatible systems, different connections to networks, and similar, but not identical, operating systems.

Option (b) could be an alternative since the VM/CMS system allows for real-time programming and debugging. However, we understand that the change-over at CERN to the VM/CMS operating system is by no means clear. IBM computers to which ALEPH laboratories have access, tend to be large systems which serve a wide user community, and hence have little flexibility towards standardization. On large computers, support for graphics will be poor with a large number of users and batch operation as at CERN (powerful graphics stations like MEGATEK need a short distance to the mainframe and require good response time).

Option (a) is widely supported within the ALEPH Collaboration. A sizeable number of VAX computers already exist in the participating laboratories. We expect the VAX to be the future CERN standard for data acquisition, and the ALEPH data-acquisition group has chosen the VAX as their standard computer. The FORTRAN on the VAX has very good debugging facilities. Despite their range of mainframes, machines of the VAX family are all strictly software compatible. Furthermore, the VAX can serve as a support system for a powerful graphics station, which we consider an important ingredient of the program development.

13.4 Data processing environment

Whatever the final choice of the software development environment is, the program will obey a number of constraints which are imposed by the prior choice of large data reduction computers on which the software product is finally to be installed.

We expect that the ALEPH Collaboration will want to use the CERN central computing facilities for the processing of the first data recorded at LEP. Only after a significant period will the major fraction of the analysis work be done outside CERN.

An important aspect of data processing is event scanning and interactive reconstruction. We expect that the computers used for the program development will continue serving for program maintenance and upgrading, but their main task will be support stations for graphics facilities.

The computing power which is at present available in the ALEPH laboratories is listed in Table 13.1, together with the names of the software co-ordinators.

13.5 Planning of software development

The total period, from the first definition of the software project until the final disposal in an archive, is called the software life-cycle. This period can be separated into distinct phases. The end of each phase represents a major milestone in the development of the software. Each phase is terminated with thorough documentation of the work which has been completed, a detailed plan for the next phase, and an updated over-all plan for the remainder of the project.

Table 13.1

Computing facilities in ALEPH Laboratories

Laboratory	Have VAX	Have IBM	Software co-ordinator
1 BARI	Yes	Some	F. Romano
2 BEIJING	<	No	
3 CERN	Yes	Yes	G. Kellner
4 CLERMOND-FERRAND	No	NET	J. Jousset
5 COPENHAGEN	No	Yes	J.D. Hansen
6 DEMOKRITOS	Would work at CERN		T. Kokkinias
7 DORTMUND	No	No	J. Knobloch
8 ÉCOLE POLYTECHNIQUE	No	NET	M. Rumpf
9 EDINBURGH	<	NET	P. Osborne
10 FRASCATI	Yes	No	G. Capon
11 GLASGOW	NET	Yes	A. Flavell
12 HEIDELBERG	No	Yes	A. Putzer
13 IMPERIAL COLLEGE	Yes	Yes	R. Beuselinck
14 LANCASTER	Yes	NET	G. Hughes
15 MARSEILLE	<	NET	J.P. Albanese
16 MPI MUNICH	No	Yes	W. Männer
17 ORSAY	No	NET	Ph. Heusse
18 PISA	<	Yes	F. Fidecaro
19 RUTHERFORD APPLETON LAB.	Yes	Yes	S.M. Fisher
20 SACLAY	No	Yes	J.F. Renardy
21 SHEFFIELD			
22 SIEGEN			
23 TRIESTE	Yes	NET	F. Liello
24 WESTFIELD COLLEGE	<	Yes	G. Heath
25 WISCONSIN	Yes	Yes	M. Mermikides

< = planned or possible NET = via network only

13.5.1 Phase 1: job definition

The following list of requirements and constraints for the ALEPH software has been agreed upon:

- User requirements concerning all aspects of physics to be explored with the detector, the evolution of the detector with time, and the access to information in view of the decentralized user community.
- Decomposition into modules which correspond to detector elements, to cope easily with modifications of the detector hardware.
- Decomposition into independent logical modules.
- Well-defined access to the data bank for each module.
- Standard interface to the data base for detector geometry, detector status, and calibration information.
- Realistic Monte Carlo simulation of data, and processing of Monte Carlo data like real data through the whole program chain.
- Versatile steering of the program flow.
- Graphics facilities for interactive reconstruction of events.
- Up-to-date documentation on several levels for casual users and experts.

Several subgroups are actively preparing detailed recommendations in the following areas of work:

- Software project management.
- Software design methodology.
- Program architecture.
- Data organization.
- Man/machine interaction and graphics.
- Coding standards and documentation.
- Program validation and test requirements.

It is agreed that the ALEPH software is to be built by a well-defined set of physicists who consider themselves programming professionals, and will devote the major fraction of their time to this effort.

13.5.2 Phase 2: job organization

In this second phase of the ALEPH software we have to define the explicit organization of the program into individual modules, and the interfaces between the program modules and the data.

At the same time, all procedures, rules, and guidelines for coding have to be defined before people start to write code.

13.5.3 Phase 3: job execution

The present idea is that coding is done in various laboratories in a decentralized way, probably on computers of the same family linked via a network. Information exchange should work through electronic mail. The full program will be regularly put together, tested, and will be simultaneously available as a new release to all programmers concerned.

13.6 Time scale

Phase 1, the job definition, will be finished around the middle of 1983.

The subsequent Phase 2, the job organization, and in parallel the implementation of the software development environment and work on prototypes of software tools, will terminate by the end of 1984. Around this time we expect the transition into Phase 3.

Phase 3—coding, validation and documentation—will continue for about three years until the end of 1987. Around this time a smooth transition into Phase 4 should occur, such that the program is available in 1988 for the processing of calibration and cosmic-ray data.

The target date for the completion of the program is the end of 1988.

14. INSTALLATION

14.1 Experimental zone

Because access to the experimental zone is difficult and space there is limited, as well as the fact that the zone becomes available rather late, our plans call for a maximum of preassembly and test on the surface before installation in the zone. This general philosophy has some bearing on the design of certain parts of the detector, such as those elements necessary for a first operation of the magnet above ground and certain difficult problems concerning cabling.

14.1.1 The detector

The detector consists of a central part and two end-caps. Figure 14.1 shows these three parts. Each of them is assembled on an independent carriage which is movable along the length of the experimental area. Each end-cap is also capable of limited motion in the beam direction to permit rapid access to the electronics at the barrel ends while the detector is in the "intersection region". An axial stroke of 2.5 m will provide reasonable access. These motions imply a corresponding mobility of the cables and of the shielding around the low-β quadrupoles, which remain fixed in their position during this operation.

A system of barracks with all relevant electronics is associated with each of these parts. Each system moves together as a unit so that interconnecting cables remain fixed. Cable-following devices are necessary only for the limited number of cables which link the three systems to each other and to the main control room on the surface.

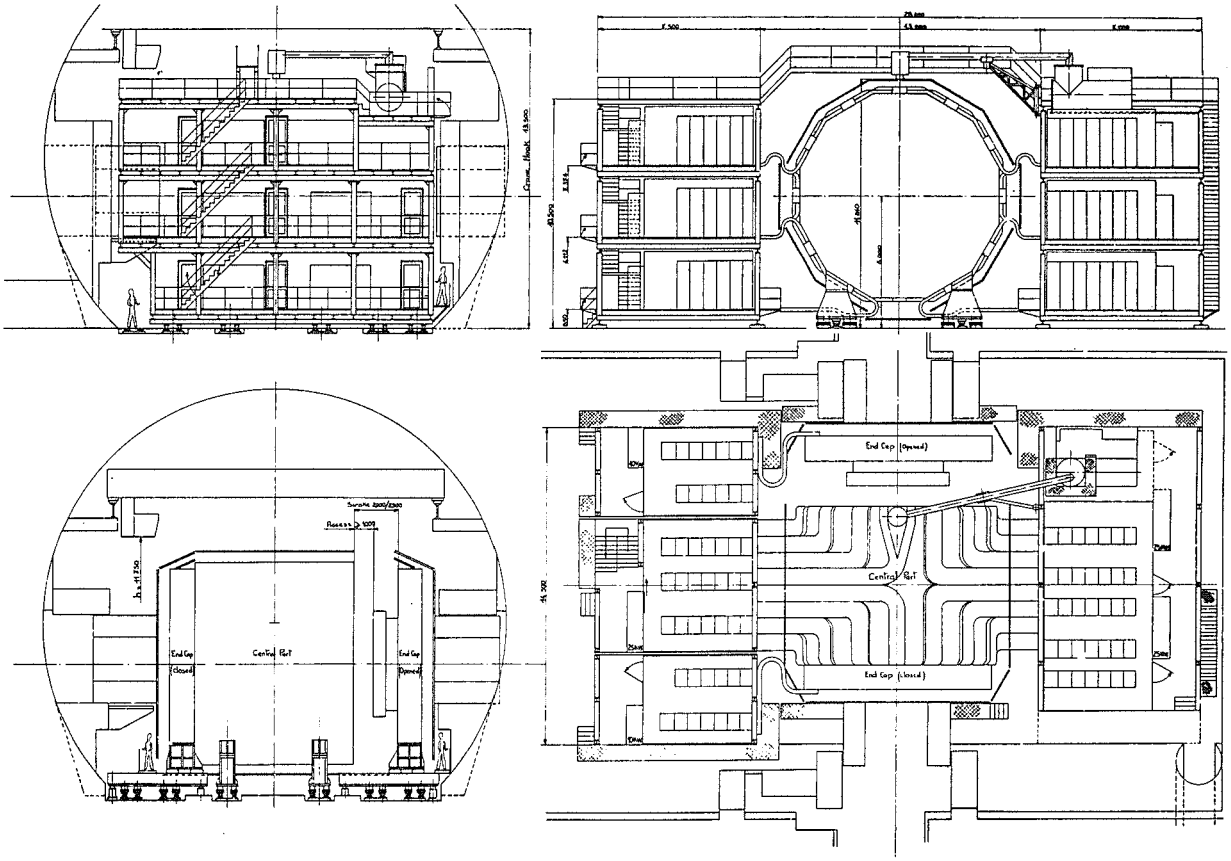

Fig. 14.1

14.1.2 Counting rooms

Counting rooms are made of standard "SPS" elements and assembled in a mechanical structure fixed to each carriage. The width of each is 5 m.The central part has three such levels on each side of the detector. On the fourth level it is planned to have on one side the gas and cooling systems of the inner part of the detector, and on the other side the refrigerator for the coil, as well as its power supply with its discharge resistance and controls. The length of the counting room is 6 m on the garage side and from 11 to 14 m on the machine side.

Each end-cap has two levels of counting rooms on the garage side of the detector. A third level may be used for the gas and cooling systems of the electronics of the electromagnetic calorimeter. The double-level barracks of the end-caps are sufficient to house the electronics and leave adequate clearance for the crane to move big pieces from one side of the apparatus to the other.

A system of stairs and gangways provides communication between the different barracks as well as access around the apparatus and to the evacuation tunnel.

14.1.3 Assembly

All parts are introduced through the shaft and the access tunnel. For some parts of the assembly it is necessary to provide specialized tooling, adapted for transporting some of the heavy loads.

Once the detector is in the intersection zone, there is no problem of material access since the tunnel entrance is then free.

It is important that the layout permits access to all elements of the detector, especially to its central parts (TPC, e–γ calorimeter, ...), when the machine is running with its shielding around the beam pipe. Figure 14.2 shows this arrangement. In this position the axis of the central part is in line with the access tunnel, and both end-caps are in the experimental area with good accessibility to each component.

In this layout, after assembly of the iron barrel, a sequential mounting of the coil, e–γ calorimeter, TPC, and the beam pipe with its equipment, is possible.

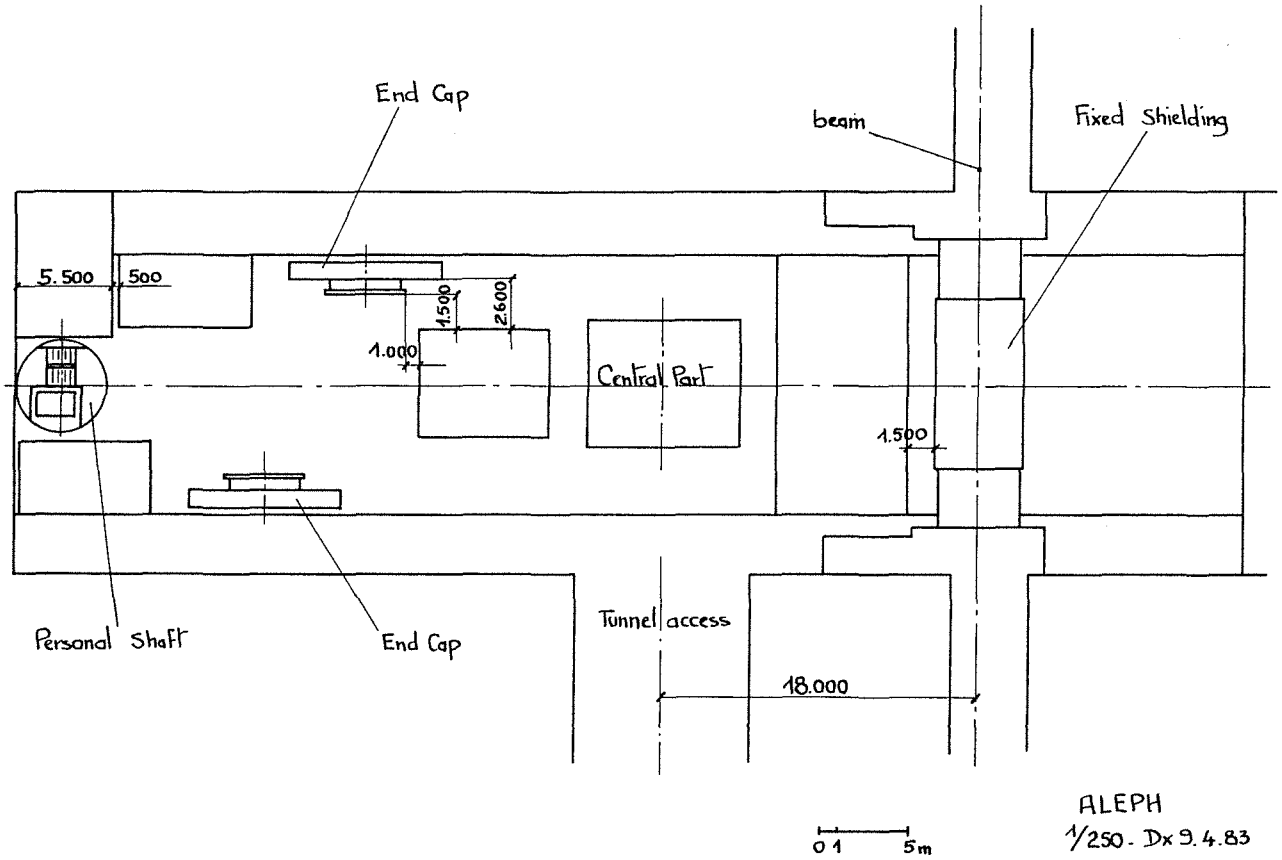

Fig. 14.2

14.1.4 Cranes

Assembly in the zone is based on simultaneous use of two cranes of 40 t each. Transfer carriages and special equipment for cranes are required only during initial assembly of the end-cap and barrel iron. Assembly of the iron of the barrel necessitates one crane equipped with two chariots of 40 t each, which can be connected in parallel. Special supports are necessary for these operations for reasons of civil engineering safety.

The iron of the end-caps is assembled using two cranes, each equipped with one chariot of 40 t. A transfer carriage on the floor is necessary to put each end-cap in its final position.

14.1.5 Fixed barracks

The equipment at the end of the experimental hall near the personnel shaft could be as shown in Fig. 14.3.

One side should be equipped with five levels of barracks and a safety system for access to the shaft in case of accident. We then foresee these barracks providing:

- a quiet room for terminals which are connected to the main computer and to the experiment via the local area network;
- a mechanical workshop, an electronics workshop, and storage space for small spares. These facilities are important, given the large distance between the surface and the experimental hall.

On the other side, we foresee barracks on only one or two levels, thus permitting the maximum stroke for one end-cap.

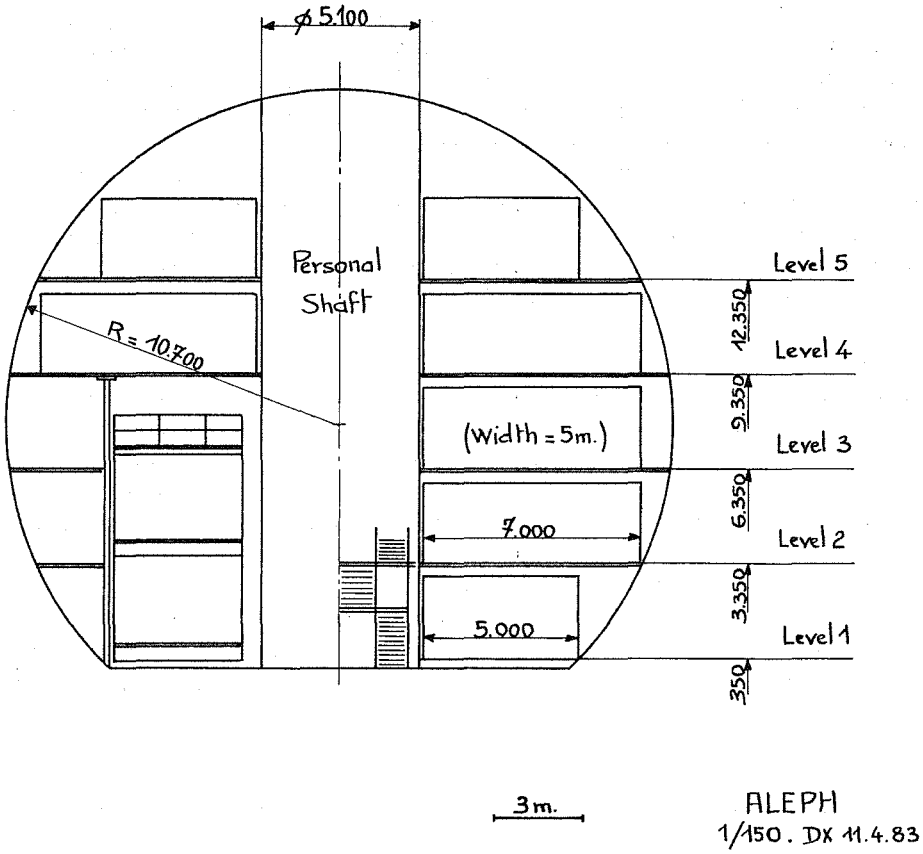

Fig. 14.3

14.1.6 Surface equipment

The main control room with the main on-line computer, graphics facilities, terminals, and general services is located on the surface.

In the surface building complex, there should be provision for a compressor system for the coil refrigerator, for gas storage, and for the gas-mixing systems.

Surface cranes for moving equipment between the surface and the zone must have:

- available at all times, a facility for lowering and raising those parts of the apparatus which do not exceed 10 to 15 t;
- available only very infrequently, a facility for dealing with heavy elements, such as the coil (~ 60 t) and the 36 iron elements of the return yoke (~ 70/75 t).

A satisfactory solution could consist of a permanently installed 20 t crane and special access to an 80 t mobile crane with appropriate boom and cable length for a fixed initial installation period.

14.2 Gases and safety

14.2.1 General philosophy

The detector uses xenon, argon, and CO_2, and relatively smaller quantities of ethane, methane, and n-pentane, which are flammable. The CO_2 will be stored in the form of compressed gas, whilst argon should be stored in the form of liquefied or compressed argon. Xenon could be stored either as a gas or as a liquid. The ethane and n-pentane will be stored in their liquid form, whereas methane will be stored as a compressed gas.

The general philosophy is to have two buildings at the surface in which the gases are stored and mixed. This surface storage in a specialized building will give us the best guarantee for a safe, well-controlled storage. The mixing will take place in a second building. The controls for the stocks, mixing equipment, pressure, flows, and alarm will be located in the main control room; this is the kind of solution which has been adopted for UA2 and has been working satisfactorily. A similar type of equipment and design could be used.

Each individual detector has its own gas distribution and control system. Used gas will be returned to the surface.

14.2.2 Inventory of the gases

a) The hadron calorimeter and muon detector use streamer tubes. In order to keep the streamers very short, one must add to the inert gas (argon + CO_2) some amount of heavy hydrocarbon; it is proposed to add 25% of n-pentane to the argon + CO_2 mixture. The gas volume of the hadron calorimeter is 70 m^3; each double layer of muon chambers contains 5 m^3 of gas. Thus, the total volume of gas will be initially 75 m^3 and will be increased to

80 m^3 after completion of a second layer of muon chambers. The density of the n-pentane is 3.2 g/l; so in the first stage, we will have 56 kg of hydrocarbon, and in the ultimate stage 64 kg of hydrocarbon.

b) The e–γ calorimeter uses a mixture of xenon and CO_2, which is non-flammable. However, it is not excluded that the e–γ will use a xenon + 20% isobutane mixture instead. Since the total volume of the e–γ calorimeter gas is 20 m^3, this corresponds to an additional 12 kg of hydrocarbon.

c) The TPC will be filled with a mixture of argon + 10% methane; it is not excluded, however, that the percentage of methane will be increased to 20%, in which case there will be 6.4 kg of hydrocarbon since the volume of the TPC is 42 m^3. It should be noted that the mixture argon + 10% methane is just at the limit of flammability.

d) The inner chamber will be filled with a standard mixture of argon + 50% C_2H_6, which corresponds to a well-saturated drift velocity. The total amount of hydrocarbon is 0.4 kg.

14.2.3 Safety considerations

From the above list it can be seen that the total amount of hydrocarbon in ALEPH will be 78 kg in the worst case. This puts us in the Class II risk, but well below the limit of 100 kg for Class III, where serious risk of explosion exists.

The safety problem has not yet been studied in detail, but we expect to follow lines similar to those of the UA experiments. The general idea is to install an alarm system which detects the presence of flammable gas in the zone, with a sensitivity well below the level of flammability. As an example for the TPC, assuming that air is used for the cooling of the electronics, methane in this air could be detected and an alarm triggered when the amount of methane is at, say, 3%, given the fact the flammability limit is 9 to 10%.

The most serious problem comes from the hadron calorimeter; the n-pentane is very dense and migrates downwards; therefore, we should have a good detection system underneath the detector and, in addition, an adequate detection system around it. The fact that the streamer tubes of the hadron calorimeter are separated by 50 mm thick iron plates decreases the risk.

14.3 Electricity, water, and air conditioning

We have estimated our needs at the ground level and in the experimental area; we do not include the needs for the cranes and for the general ventilation, which come under the jurisdiction of the LEP machine.

14.3.1 At the surface level

Here the compressors of the refrigerator and the main control room with its computers are installed. The electrical consumption is estimated to be 500 kW. In addition, 35 m^3/h of industrial water are needed for the cooling of the compressors. The air-conditioning system should be able to evacuate 50 kW. Finally, 15 m^3/h of compressed air is needed for the refrigerator.

14.3.2 In the experimental zone

The total power consumption is estimated at 900 kW: 100 kW for the power supply and accessories of the coil, and 800 kW for the electronics. The air-conditioning system should be able to evacuate $\sim$ 1/3 of the electrical power dissipated by the electronics, i.e. 270 kW. The remaining electrical power as well as the power dissipated by the cold box will be evacuated by cold water. The total water consumption in the experimental zone will be 20 l/s. Using an input temperature of 12 °C, a rise of 8 °C is foreseen.

14.4 Assembly schedule

Of the four experimental zones, zone No. 4 or No. 8 could be allocated to ALEPH. For planning purposes, we assume here that zone No. 8, which will be the first zone ready for the installation of an experiment, will be made available to us. According to the programme of the LEP machine, this zone will be at the disposal of the experiment by 1 July 1987, if the civil engineering works begin, as is at present foreseen, on 1 July 1983.

In order to achieve this installation correctly and in a minimum of time, we consider it essential to prepare the work, as much as possible, in a hall at ground level.

We keep in mind that the planning should include:

a) a thorough, long test of the solenoid; and

b) a careful test of the TPC *in situ* in a magnetic field.

Consequently, our installation planning contains two phases:

Phase 1: at the ground level

During 1986, the modules of the iron structures are expected to be delivered and equipped with the streamer tubes, first of all the barrel, then the end-caps.

The modules of the barrel should be mounted together before 1 November 1986, in such a way that the mounting of the coil can start at the delivery date of **1 November 1986.** The assembly of the coil and the iron yoke is expected to be completed by **1 January 1987.**

We propose to conduct a full test of the magnet, including the first three-dimensional field mapping and TPC installation, between **1 January 1987** and 1 July 1987. The location of these tests is not yet clear, but a place near the

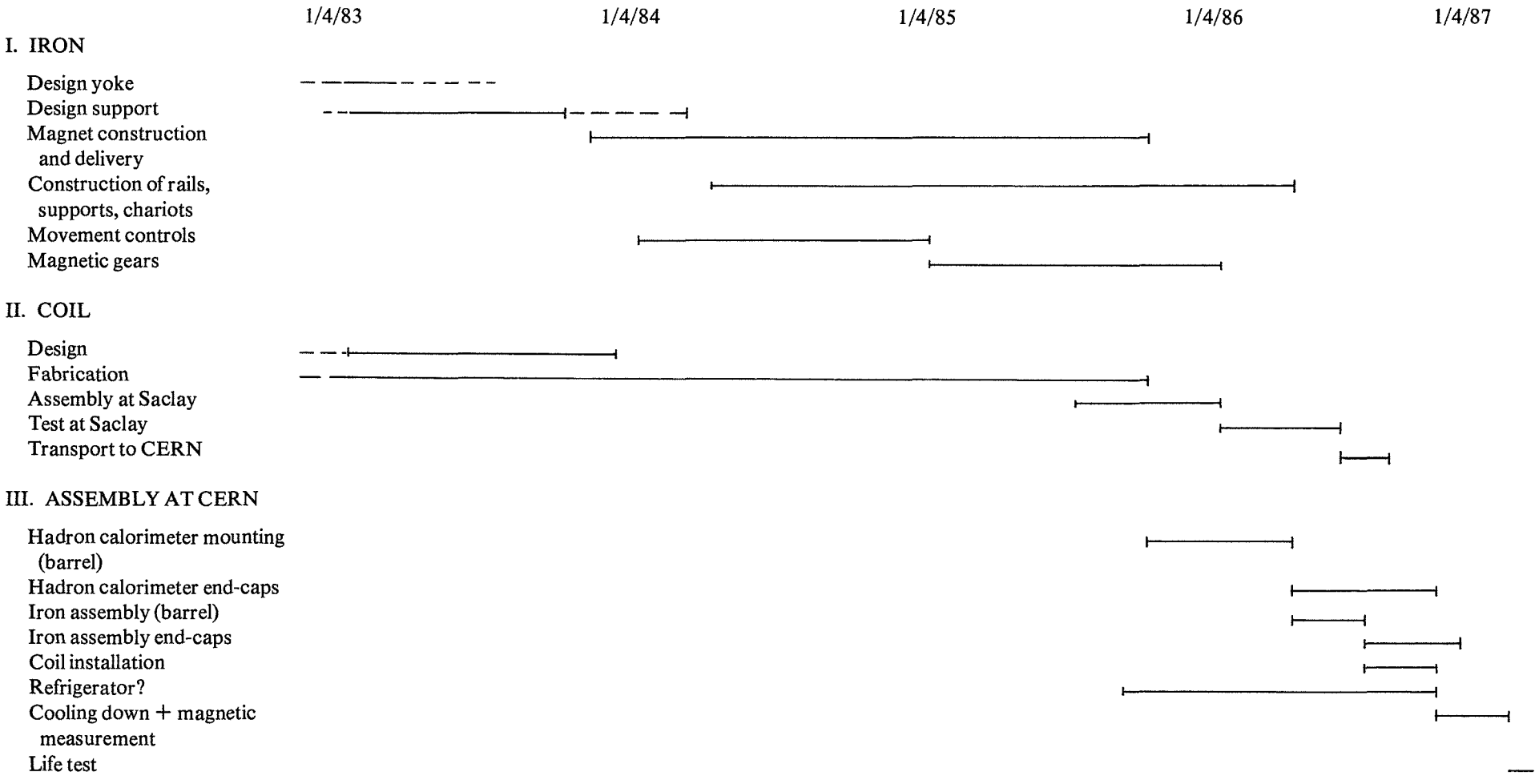

Fig. 14.4 PREASSEMBLY OF THE MAGNET AT GROUND LEVEL

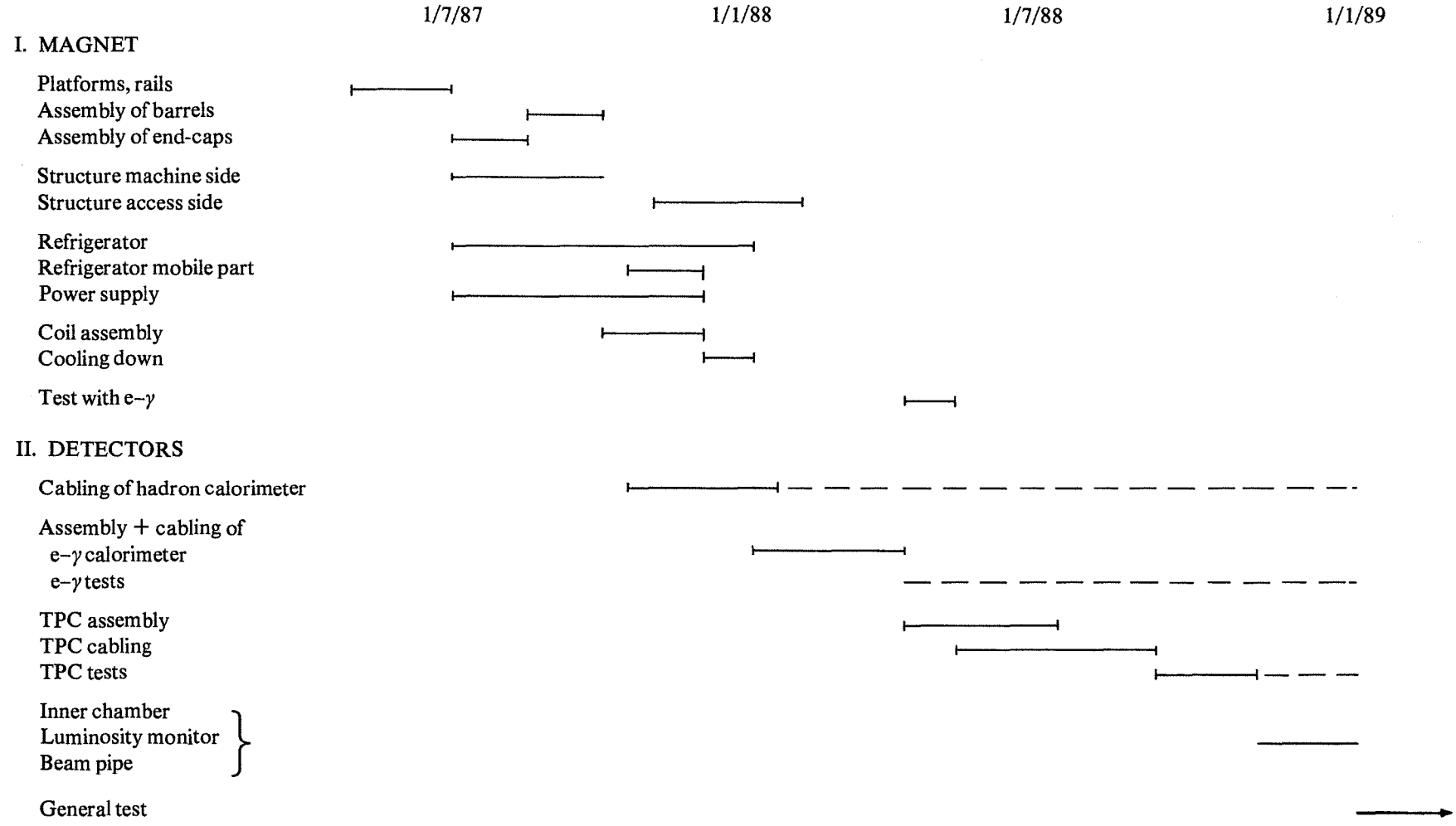

Fig. 14.5 GENERAL ASSEMBLY PLANNING

zone would be preferable. Then, in July 1987, we will prepare the installation in the experimental zone. Under these circumstances we will try to transport the coil in a single piece; this seems to be possible in a first approximation (Fig. 14.4 shows the details of this planning).

Phase 2: in the experimental zone

The general assembly is expected to take about 20 months. If we succeed in completing phase 1 as described including the magnetic measurements, the installation time will be reduced to 18 months. This assumes that the cabling has been carefully prepared on a mock-up, cables cut at the right length, and connectors mounted in advance, etc.

The solenoid will be kept cold from the first cooling-down onwards. A check of the magnetic field will be made after the installation of the electromagnetic calorimeter. One sees that in the best case, namely 18 months of installation, we will just be ready in time when LEP turns on. Figure 14.5 shows the details of this planning.

14.5 Space requirements at CERN and experimental areas

a) During the construction period, space will be needed on the present site for offices, laboratories, and a hall; a request for these has been made. We are asking for approximately 30 additional offices for the housing of about 70 new people.

An increase in laboratory space from 100 m^2 to 500 m^2 between now and the end of 1984 is requested, essentially for the assembly of the TPC.

Approximately 3600 m^2 of hall, equipped with a large crane, will be needed, essentially from the end of 1984 until 1988, when the installation in the experimental zone finishes. A relatively small part ($\sim$ 200 m^2) of these 3600 m^2 is needed immediately for development and prototype work for the TPC.

Finally during the assembly period, a storage area of about 1500 m^2 will be required.

b) In addition to the experimental area, which is already described in the civil engineering contract, a number of surface buildings are needed for housing the various auxiliary services, the main on-line computer, and the main control room.

Our present estimates are as follows:

– Main control room and computer room	300 m^2
– $\sim$ 20 offices and a small conference room	300 m^2
– Compressor building for the refrigerator	200 m^2
– Gas storage and mixing	200 m^2

14.6 Requested services from CERN in the experimental zone

A list of these services (as exhaustive as possible) has been established in collaboration with F. Bonaudi. The corresponding costs are included in the budget of the LEP machine, or in the CERN contribution to the ALEPH budget (see subsection 14.7).

The Collaboration expects CERN to provide an experimental zone equipped with the needed lifting facilities, the ventilation, the lifts, and such other necessary services as electrical installation, water and compressed air supplies, an emergency main, and alarms and interlocks to the machine. In addition, CERN should provide the surface buildings which house gas storage, mixing and distribution, the compressor for the refrigerator of the coil, a few offices, the main control room, the mounting hall at the top of the access shaft, as well as crane facilities capable of handling 80 t pieces.

We expect CERN to build, according to our specifications and in collaboration with us, the fixed and mobile counting rooms, with their gangways, supporting structure, air conditioning, etc. In the same manner, CERN should make the special tools needed for the final assembly, the platforms, chariots, shielding, vacuum pipe, etc. We expect CERN to take part in the assembly of the detector, providing the general co-ordination and part of the necessary manpower, in particular crane drivers, transport people, staff for laying down the cables.

Finally, we expect CERN to take responsibility for the maintenance of the general services, such as electricity, water, compressed air, ventilation, lifts, cranes, alarms, etc.

14.7 ALEPH budget for zone installation

a) General services (all prices in kSF):

Shielding	500
Ventilation (safety)	200
Cooling (installation)	50
No-break supply	80
Gas distribution	100
Gas storage and safety	600
Exhaust lines	100
Crane*)	300

*) Concerning the crane, this number is not final. It is based on the hypothesis that we use a double-chariot crane of 2 × 40 t in the experimental zone.

		Carried forward:	1930
	Electrical installation	500	
	Handling gear, chariots	200	
	Special tooling	300	
	Survey	50	
	Barracks (fixed)	500	Total: 3480
b)	Counting rooms:		
	Structure	950	
	Passage ways	250	
	Cable trays	250	
	Barracks (movable)	350	
	Racks (80 water-cooled, 80 open)	720	
	Cables installation	500	
	Barracks climatization	500	Total: 3520
		Grand total:	7000

15. TEST BEAM REQUIREMENTS

Prototypes and real-size modules of the various parts of the detector have to be tested. These tests will be performed by different groups at different times over the coming years, using particles of different types and momenta.

The three main pieces of equipment to be tested are the electromagnetic calorimeter, the hadron calorimeter, and the TPC.

The electromagnetic calorimeter tests (three different prototypes will be tested) need good e/π separation and momentum resolution in the beam, and particles also of small momenta (< 10 GeV). The biggest item which has to be provided is a magnet with a large pole shoe gap (of the ISR system type) to study magnetic field effects on the wire signal behaviour.

The hadron calorimeter prototype ($\sim 1.5 \times 1.5 \times 1.8$ m^3) tests need 5–50 GeV particles, sometimes also of very low intensity (a few particles per second). Since the real calorimeter will be preceded by the electromagnetic calorimeter, in which a sizeable fraction of the hadrons interact, the performance of the prototype has to be tested with a module of the electromagnetic calorimeter (or its equivalent) in front of it. A means of distinguishing muons from pions is a requirement which might have to be built into the test set-up, since the beam will not provide μ identification.

The tests with the TPC prototypes require about as much time without beam as with beam (because of the work on a laser calibration system); hence the TPC test must be installed at the downstream end of the area separated from the upstream part by a movable dump, such that it can be accessed also when the beam is used for calorimeter tests. The TPC tests use a pulsed solenoidal magnet (270 kW, 2 × 1500 A, 470 V).

Apart from these three major items, several smaller parts — such as a luminosity monitor and other auxiliary equipment — will have to find space and beam for tests.

The test area foreseen for ALEPH in the West Area [X7b, 26 × (6–8) m^2 surface, 30 t crane, 16 × 4 m^2 barrack, 5–100 GeV beam] seems to fulfil most of the requirements for installing and testing prototypes, if the calorimeters are easily removable and their tests properly scheduled. However, its width of 6 to 8 m will make tests of real-size calorimeter modules (7 m wide) very difficult or even impossible.

The X-beams derived from the H3 beam in the upgraded West Area (D. Plane, SPS/EBS/Note 82-12) deliver particles with good variability; however, the feasibility of less than 5 GeV beams (especially protons around 1 GeV, necessary for TPC tests) has to be studied further.

An important requirement for the test area is flexible coordination at various levels: inside the X7b area, between the X7b and X7a (DELPHI) areas, and between the H1–H3 beam and the various test area users.

We expect that the need for test beam facilities will not end with the start up of LEP. Repetition of calibrations will probably be necessary, as well as the testing of new components.

16. GROUP COMPOSITION, RESPONSIBILITIES, MANPOWER

Spokesman: J. Steinberger
Technical co-ordinator: P. Lazeyras
Mechanical co-ordination: Ph. Delcros
Electronic co-ordination: J.C. Gouache and I. Pizer
Safety co-ordination: P. Lazeyras
Installation co-ordination: H. Atherton
Financial co-ordination: R. Budde

For the time being, the participating laboratories and the corresponding physicists and senior technical staff are the following (the total number is indicated for each institution):

Bari: (15)	M. De Palma, O. Erriquez, C. Favuzzi, B. Ghidini, G. Maggi, M.T. Muciaccia, S. Natali, F. Navach, S. Nuzzo, T. Ranieri, F. Romano, F. Ruggieri, G. Selvaggi, P. Spinelli, G. Zito
Beijing: (7)	J.F. Lin, S.G. Wang, X.L. Wang, W.M. Wu, Y.L. Xu, W.G. Yan, J.Q. Zhang
CERN: (32)	H. Atherton, R. Budde, D. Cundy, F. Dydak, Mi. Ferro-Luzzi, J.P. Froberger, F. Gagliardi, J.C. Gouache, R. Hagelberg, F. James, G. Kellner, H. Kowalski, A. Lacourt, P. Lazeyras, I. Lehraus, R. Matthewson, J. May, P. Palazzi, G. Petrucci, I. Pizer, M. Price, F. Ranjard, W. Richter, D. Schlatter, J. Steinberger, W. Tejessy, H. Verweij, W. von Rüden, H. Wachsmuth, H. Wahl, W. Witzeling, J. Wotschack
Clermont-Ferrand: (6)	A. Falvard, J. Jousset, B. Michel, J.C. Montret, M. Querrou, F. Vazeille
Copenhagen: (6)	J.D. Hansen, J.R. Hansen, O. Kofoed Hansen, B. Madsen, R. Møllerud, B.S. Nilsson
Demokritos Athens: (5)	N. Demetriou, M. Dris, T. Kokkinias, E. Simopoulou, A. Vayaki
Dortmund: (11)	A. Dunkel, W. Hofmann, K. Kleinknecht, J. Knoblauch, E. Müller, D. Pollmann, B. Pszola, B. Renk, J. Richstein, K. Rauschnabel, D. Wegener
Ecole Polytechnique Palaiseau: (13)	J. Badier, P. Benkheiri, A. Blondel, A. Busata, Ph. Delcros, G. Fouque, F. Jacquet, Ph. Miné, J.Y. Parey, A. Rougé, M. Rumpf, H. Videau, I.M. Videau
Edinburgh: (4)	D.J. Candlin, J. Muir, P. Osborne, K.J. Peach
Frascati: (12)	R. Baldini, G. Battistoni, G. Beck, G. Bologna, P. Campana, G. Capon, F. Celani, B. D'Ettorre Piazzoli, E. Iarocci, P. Laurelli, G. Murtas, P. Picchi
Glasgow: (18)	P.J. Bussey, J.B. Dainton, A.J. Flavell, D. Frame, I.S. Hughes, J.G. Lynch, D.M. McFadzean, D.J. Martin, P.J. Negus, R. O'Neill, C. Raine, W.L. Randolph, J.M. Scarr, I.O. Skillicorn, K.M. Smith, D.T. Stewart, A.S. Thompson, R.M. Turnbull
Heidelberg: (8)	C. Geweniger, P. Hanke, V. Hepp, W. Heyde, E.E. Kluge, J. Krause, A. Putzer, K. Tittel
Imperial College: (20)	T.C. Bacon, G. Barber, R. Beuselinck, D.M. Binnie, W. Cameron, P.J. Dornan, B. Foster, D.A. Garbutt, D. Gentry, J.V. Gibb, G. Hall, W.G. Jones, J.G. McEwen, D.G. Miller, D.R. Price, P. Rankin, J.K. Sedgbeer, L. Toudup, D.M. Websdale, A.P. White

Lancaster: (3)	F. Foster, G. Hughes, T. Sloan
Marseille: (9)	J.P. Albanese, J.J. Aubert, R. Bazzoli, C. Benchouk, G. d'Agostini, Y. Déclais, R. Nacasch, P. Payre, M. Talby
MPI Munich: (13)	W. Blum, H. Brettel, J. Fent, Z. Hajduk, G. Lütjens, W. Männer, H. Münch, A. Peisert, R. Richter, R. Settles, U. Stierlin, W. Tribanek, P.K. Weissbach
Orsay: (15)	J. Boucrot, O. Callot, R.L. Chase, A. Cordier, M. Davier, D. Decamp, M. Dialinas, A. Ducorps, D. Fournier, J.F. Grivaz, Ph. Heusse, Ph. Jean, J. Lefrançois, A.M. Lutz, J.J. Veillet
Pisa: (18)	S.R. Amendolia, E. Bertolucci, L. Bosisio, P.L. Braccini, C. Bradaschia, R. Castaldi, M. Dell'Orso, F. Fidecaro, L. Foà, E. Focardi, A. Giazotto, M. Giorgi, M. Givoletti, I. Mannelli, P.S. Marrocchesi, G. Sanguinetti, G. Tonelli, C. Vannini
Rutherford Appleton Laboratory: (15)	D.R. Botterill, M. Cawthraw, R. Clifft, I. Corbett, M. Edwards, S.M. Fisher, R. Gray, R. Hand, A.J. Lewis, D. Moore, M. Morissey, P. Norton, G. McPherson, G. Tappern, J.C. Thompson
Saclay: (19)	Ph. Bloch, E. Bonnin, G. Bosc, P. Debu, H. Desportes, R. Duthil, L. Gosset, C. Guyot, M. Jacquemet, J. Le Bars, P. Micolon, M. Mur, S. Palanque, A. Para, P. Perez, B. Peyaud, J. Rander, J.F. Renardy, R. Turlay
Sheffield: (1)	F. Combley
Siegen: (8)	A. Bäcker, S. Brandt, C. Grupen, M. Holder, H.J. Meyer, M. Rost, K.H. Stupperich, G. Zech
Trieste: (7)	G. Batignani, M. Budinich, F. Liello, E. Milotti, F. Ragusa, L. Rolandi, A. Stefanini
Westfield College, London: (8)	E.H. Bellamy, M.G. Green, G.A. Heath, M.P.J. Landon, P.V. March, D. Newman-Coburn, J.A. Strong, J. Sutton
Wisconsin: (7)	T. Barklow, M. Mermikides, T.C. Meyer, G. Rudolph, E. Wicklund, S.L. Wu, G. Zobernig

The participants of ALEPH have defined the sharing of the responsibilities between themselves in the following manner:

a) The superconducting solenoid is paid in common by the participating laboratories. It will be constructed and installed under the responsibility of Saclay. At Saclay the engineers — 5.5 man-years — are available. From the extra 29.5 man-years needed, 6 are available at Saclay; the rest, to be hired on a temporary basis, are included in the cost estimate of the solenoid. R. Turlay co-ordinates this project.

b) The iron structure, the refrigerator, and the power supply for the superconducting solenoid, which are paid by a common contribution of all participants, will be designed and fabricated, assembled, and installed under CERN responsibility (G. Petrucci). The corresponding manpower for the iron structure is 24.5 man-years, of which 19 are available at CERN. The 5.4 missing man-years have been included in our cost estimates. The EF Cryogenic Group under M. Morpurgo will take care of the refrigerator and has the necessary means.

c) The over-all responsibility and the co-ordination for the TPC is given to CERN; the development and construction work is shared between CERN, Dortmund, Pisa, MPI Munich, Trieste, and Wisconsin. The calibration system will be constructed by Dortmund and Glasgow. The manpower needed for the TPC construction is estimated at 82 man-years, of which 15 are not available and must be hired. The corresponding cost is included in our budget. The TPC co-ordinator is J. May.

d) The electromagnetic calorimeter has been divided into two main parts: the end-caps and the barrel. The Rutherford Appleton Laboratory has the responsibility of the end-caps. The responsibility for the barrel is shared between Saclay and the French Institute IN2P3, comprising Clermont-Ferrand, Ecole Polytechnique Palaiseau, Marseille,

and Orsay. The co-ordinators are J. Rander for the barrel and P. Norton for the end-caps. The manpower is estimated at 35 man-years for the barrel, of which approximately 9 must be hired. As far as the end-caps are concerned, the requested 35 man-years are available at RAL and Glasgow.

e) The hadron calorimeter and the muon detector are being procured by the Italian collaborators. They have divided the work as follows: Frascati will deliver the barrel part; Bari and Pisa the end-caps. The over-all co-ordinator is L. Foà. The total manpower needed is 44 man-years, of which 5 must be hired. Their cost has been included in the cost estimate. This manpower is only foreseen for the hadron calorimeter and one layer of muon chambers, which correspond to a reduced version of the detector. Extra manpower will be needed later on for the construction of the second layer of muon chambers. The possibility of sharing the responsibility for the muon detector with Beijing is under discussion.

f) The inner chamber will be built at Imperial College in London, with some help from RAL; between them they have the 18 man-years needed for its construction, including the prototypes and the tests. P. Dornan is the co-ordinator.

g) The responsibility for the luminosity monitors, comprising chambers and calorimeters, is shared between the Universities of Siegen and Copenhagen. The co-ordinators are C. Grupen and R. Møllerud.

h) The Pisa Group is responsible for the minivertex detector. For financial reasons, this detector is not included in the first stage of the construction, but will come later. Six man-years are necessary for its realization; the co-ordinator is M. Giorgi.

i) The responsibility of the trigger is given to Heidelberg and RAL, with K. Tittel as co-ordinator. The needed manpower is available.

j) A large number of groups—if not all groups—is involved in the data processing, which is co-ordinated by F. Dydak. The on-line system, essentially under CERN responsibility, is co-ordinated by W. von Rüden, whilst the central computer for this on-line system will be procured by RAL. The off-line software will be developed under the responsibility of G. Kellner.

17. FINANCES

The budget as presented here gives:

a) the financial participation of the members of the Collaboration;
b) the cost estimate for the different parts of the detector and its installation;
c) a discussion of those detector elements whose realization, for budgetary reasons, has to be postponed ("staged");
d) the cost estimate of the first stage of the detector;
e) the distribution of the financial responsibilities for realizing this detector.

The financial participation which the different members of the Collaboration will make available for the ALEPH detector has been calculated at 1983 prices. In such cases where it is based on currencies other than Swiss francs (SF), the exchange rate of 28 February 1983 was used. The financing period normally covers five years (1983–1987), with one exception (IN2P3) where it includes also 1988. Corrections for inflation are expected to be allocated in most cases.

The cost estimate is grouped into the following items:

- Magnet and main computers (to be financed in common by the whole Collaboration).
- Infrastructure and counting rooms (financed out of the CERN participation of 13.6 MSF).
- Trigger elements and data acquisition.
- Main detector hardware.
- Cost for installation, tests, commissioning, and running-in, which is planned to be paid 1988/1989.

Exchange rates used (28 February 1983)

1 £ = 3.11 SF
1 DM = 0.84 SF
1 FF = 0.30 SF

a) Financial participation (MSF, 1983) for 1983–1987 (1988)

CERN	13.60*)	
Denmark	0.50	
Germany	9.50**)	(4.6 MDM/3 years × 1.66 + 3.06 MSF (MPI))
IN2P3	7.00*)	(3.33 FF = 1 SF; over 6 years)
Italy	12.00	
Saclay	4.00*)	(3.33 FF = 1 SF)
UK	10.60*)	(3.4 M£)
Wisconsin	3.00	
	60.20 MSF	

b) Cost estimate (MSF)

Iron structure	9.80		
Coil	9.70		
Refrigerator	2.00		
Main computers	1.20		22.70
Infrastructure	3.45		
Counting rooms	3.55		7.00
Inner chamber	0.90	(290 k£)	
Trigger	1.20		
Luminosity monitor	0.65		
Data acquisition	0.95		
Off-line software	2.50		6.20
TPC	11.40		
e–γ calorimeter, reduced version	11.35		
Hadron calorimeter + 2 μ-chamber double layers	6.90		
Minivertex detector	1.25		30.90
		Subtotal	66.80
Installation, tests, commissioning, running-in			6.00
		TOTAL	72.80

*) Correction for inflation (c.f.i.) expected.
**) Fixed for 3 years; for next 3 year period some c.f.i. expected.

c) Stage one detector

In order to stay within the roughly 60 MSF budget currently understood to be available during the five-year construction period, the project must be reduced or its realization in part postponed.

We propose one reduction in scope: the e–γ calorimeter has been modified with respect to the original proposal such that the lead thickness for the last 10 of the 22 radiation lengths is increased from 2 to 4 mm. This deteriorates the energy resolution for electrons and gammas above ~ 10 GeV by about 10%; at lower energy the deterioration is not significant. The effect on the cost is already included in the budget of point (b).

The items which must be postponed are as follows:

- The minivertex detector.
- The instrumentation of the individual tube readouts of the hadron calorimeter.
- The second double layer of muon chambers and associated circuits.
- The off-line computing facility.
- The item labelled "installation, tests, commissioning, and running-in". These expenses might be called contingencies, and the figure of 6 MSF which is given is a guess. They are not expected to appear until 1988–1989, when additional resources are expected to be available.

d) Cost estimate, staged version (MSF)

Iron structure	9.80		
Coil	9.70		
Refrigerator	2.00		
Main computers	1.20		22.70
Infrastructure	3.45		
Counting rooms	3.55		7.00
Inner chamber	0.90	(290 k£)	
Trigger	1.20		
Luminosity monitor	0.65		
Data acquisition	0.95		3.70
TPC			11.40
e–γ calorimeter, reduced version			11.35
Hadron calorimeter + 2μ-chamber layers staged version			5.00
		TOTAL	61.15

e) Distribution of financial responsibilities

		Participation (MSF)	Cost (MSF)
e–γ calorimeter	IN2P3	4.02	
	Saclay	2.29	
	UK	4.56	
	not financed	0.48	11.35
TPC	CERN	2.83	
	Dortmund	1.02	
	Heidelberg	0.13	
	Italy	1.87	
	MPI	2.66	
	Siegen	0.39	
	UK	0.31	
	Wisconsin	1.72	
	not financed (staged)	0.47	11.40

Hadron calorimeter and 2μ-chamber layers (staged version)	Italy		5.00
Inner chamber	UK		0.90
Trigger	Heidelberg	0.89	
	UK	0.31	1.20
Luminosity monitor	Denmark	0.29	
	Siegen	0.36	0.65
Data acquisition	CERN		0.95
	Subtotal:		31.45
Magnet, main computers	Whole Collaboration		22.70
Infrastructure, counting rooms	CERN		7.00
	TOTAL		61.15

The observant reader will have noticed that $\sim$ 1 MSF is still missing according to the present estimates — half of this in the e–γ calorimeter budget, half in the TPC budget. These sums are much less than the uncertainties in the cost estimates. Perhaps we will be lucky and some of the costs, especially of the electronics which is such a big part of both budgets, will turn out to be lower than estimated. If not, corresponding amounts of the electronics will have to be "staged".